FFI-rapport 2015/01750

Crowds2D – a new, robust crowd dynamics simulation model

Steinar Børve

FFI Forsvarets forskningsinstitutt

Crowds2D – a new, robust crowd dynamics simulation model

Steinar Børve

Norwegian Defence Research Establishment (FFI)

13 January 2016

FFI-rapport 2015/01750

1255

P: ISBN 978-82-464-2638-9
E: ISBN 978-82-464-2639-6

Keywords

Gruppedynamikk

Numeriske metoder

Modellering og simulering

Menneskelig atferd

Approved by

Eirik Svinsås	Research Manager
Jon E. Skjervold	Director

English summary

The Norwegian Armed Forces have over the last few years given priority to the procurement of less-lethal weapons (LLW) for use in certain scenarios. The purpose of FFI project 1255 has therefore been to support the armed forces in choosing the right means for different tactical scenarios and in a rapidly evolving marked. One class of scenarios where LLW can be a relevant tool involves human crowds. Choosing the right tool in such a scenario requires insight into the behaviour of human crowds.

The collective behaviour of human crowds is of interest not only to the armed forces, but also in civil applications such as pedestrian traffic studies, security planning of events involving large crowds, and police crowd management during political demonstrations and riots. The latter scenario is also relevant for the armed forces in operations abroad where peace-keeping and law-enforcement is an important part of the assigned task. In situations where law-enforces confront a crowd which include hostile or even violent individuals, one must decide whether or not to utilize LLW to control the crowd. The important question then is what can be achieved in a given scenario in terms of crowd management depending on whether LLWs are applied or not.

This report describes a new, robust crowd dynamics simulation model capable of simulating a wide range human crowd behaviour. It is a technical report and documents the important first steps towards a potentially useful tool in the analysis of LLW-related operations. This includes not only normal pedestrian traffic, but also scenarios such as evacuation or riots which might involve running agents. The model relies on a number of model parameters. Default values of these parameters have been determined on the basis of fundamental properties of the human body, semi-analytical models of fundamental crowd behaviour, and simplified crowd test simulations.

The new model not only captures crowd movement well, it also provide information on force levels which in turn can be used to assess the risk of injuries and deaths.

Sammendrag

Forsvaret har dei siste åra lagt vekt på å kjøpe inn Mindre-dødelege våpen (MDV) for å kunne handtere visse situasjonar. FFI-prosjekt 1255 har hatt som formål å hjelpe Forsvaret med å velge riktige verkemiddel under ulike taktiske situasjonar og i ein marknad som er i rask utvikling. Ein klasse av situasjonar der MDV kan vere eit aktuelt verkemiddel involverer større menneskemengder. Å kunne velge riktig verkemiddel i ein slik situasjon krev at ein har innsikt i korleis menneskemengder kan opptre.

Kunnskap om dynamikken til menneskemengder er av interesse ikkje berre for Forsvaret, men kan óg komme til nytte innanfor sivile bruksområde som t.d. studiar av fotgjengartrafikk, planlegging av sikringstiltak rundt arrangement som involverar store menneskemengder og planlegging av politiaksjonar ved politiske demonstrasjonar og opptøyar. Det siste scenarioet er òg relevant for Forsvaret i utanlandsoperasjonar der fredsbevaring og arbeidsoppgåver knytta til lov-og-orden er ein viktig del av oppdraget. I situasjonar der ein som ordensmakt skal konfrontere ei menneskemengd som inneheld fiendtleg innstilte eller til og med valdelege enkeltindivid, må ein vurdere kor vidt ein skal ta i bruk MDV for å halde kontroll på menneskemengda. Det viktige spørsmålet er i så fall i kva grad ein kan påverke dynamikken til menneskemengda, med eller utan bruk av MDV.

Denne rapporten skildrar ein ny, robust simuleringsmodell for studiar av dynamikken til ei menneskemengd. Han er av teknisk karakter og dokumenterar viktige fyrste steg på vegen mot eit potensielt nyttig verkty i analysen av MDV-relevante operasjonar. Modellen er ikkje berre i stand til å simulera normal fotgjengartrafikk, men òg scenaria knytt til evakuering eller opptøyer som kan involvere springande personar. Modellen bygger på ei rad modelparametrar. Standardverdiar for desse parametrane har blitt bestemt på bakgrunn av grunnleggande eigenskapar ved menneskekroppen, semianalytiske modellar av fundamental dynamikk i menneskemengder og foreinkla simuleringar av menneskemengder. Den nye modellen skildrar ikkje berre rørsla i ei menneskemengde på ein god måte. Han gjev i tillegg informasjon om storleiken på kreftene som verkar i menneskemengda. Dette er informasjon som kan vere nyttig i vurderinga av risikoen for personskader og dødsfall grunna uheldig dynamikk i menneskemengder.

Contents

1	**Introduction**	**7**
2	**Simulation model overview**	**8**
2.1	Observations regarding human anatomy and behaviour	8
2.1.1	Biomechanical properties of the human body	9
2.1.2	Assumptions regarding fundamental human behaviour in crowds	10
2.2	Introduction to the agent-based force model	11
2.3	Spatial interaction function	12
2.4	Obstacle avoidance and crowd repulsion	14
2.5	Variable interaction range	15
2.5.1	Obstacle avoidance scale length	15
2.5.2	Crowd repulsion scale length	16
2.5.3	Comparison of scale lengths and robust calculation of smoohting length	17
3	**Internal forces**	**20**
3.1	Displacement force	20
3.2	Flow will force	21
3.2.1	Non-linear flow will	22
3.3	Strain force	24
4	**Inter-agent forces**	**25**
4.1	Social force	25
4.1.1	Obstacle avoidance interaction	25
4.1.2	Crowd repulsion	26
4.2	Contact force	27
5	**Solid boundary interaction**	**27**
5.1	Boundary interaction scale length	29
5.2	Density correction	30
5.3	Social boundary force	32
5.3.1	Boundary avoidance interaction	33
5.3.2	Wall repulsion interaction	33
5.4	Contact boundary force	37
5.5	Automatic path finder	38

6	**Model calibration**	**38**
6.1	Uni-directional, homogeneous flow ($A_{\text{crowd}}/A^v_{\text{will}}$ and θ_0)	39
6.1.1	Results with a linear will force	39
6.1.2	Results with a non-linear will force	40
6.2	Multi-directional, homogeneous flow ($A^r_{\text{avoid}}/A_{\text{crowd}}$)	41
6.3	Agent meeting ($A^d_{\text{avoid}}/A_{\text{crowd}}$)	43
6.3.1	Asymmetric meeting	43
6.3.2	Symmetric meeting	44
6.4	Crowd naviagtion (e_{avoid} and ρ_{avoid})	45
6.5	Agent pair equilibrium ($A^r_{\text{will}}/A^v_{\text{will}}$ and σ_{min})	49
6.6	Single agent boundary avoidance ($C_{\mathcal{B}}$ and $q_{\mathcal{B}}$)	49
6.7	Homogeneous crowd stopping near boundary ($p_{\mathcal{B}}$)	52
7	**Crowd tests**	**53**
7.1	Full-scale simulation of uni-directional flow	53
7.2	Bi-directional flow in a torus-shaped channel	54
7.3	Pedestrian flow through bottlenecks	59
7.4	Evacuation from a building	61
8	**Conclusion**	**64**
	Bibliography	**69**
Appendix A	**Calculating the wall repulsion integral, I^{wall}_{ab}**	**71**
A.1	Approximation to I^{wall}_{ab} with normal sector lines	71
A.2	Modifications to I^{wall}_{ab} due to boundary segment intersections	73
A.2.1	End point related coordinates	73
A.2.2	Boundary segment intersections	75
A.2.3	Modified wall repulsion integration	76
A.3	Wall repulsion from curved boundaries	78
Appendix B	**Automatic path finder algorithm**	**79**

1 Introduction

The collective behaviour of human crowds is of interest in civil applications such as pedestrian traffic studies, security planning of events involving large crowds, and police crowd management during political demonstrations and riots. The latter scenario is also relevant for the armed forces in operations abroad where peace-keeping and law-enforcement is an important part of the assigned task. In situations where law-enforces confront a crowd which include hostile or even violent individuals, one must decide whether or not to utilize less-lethal weapons (LLW) to control the crowd. The important question then, is what can be achieved in a given scenario in terms of crowd management depending on whether LLWs are applied or not.

Crowd modelling has in recent years become an important tool in studying the dynamics of human crowds (see Zhou et al. (2010) for a review), in applications ranging from military simulation, safety engineering, architectural design, and digital entertainment. Most of these models are developed with a typical pedestrian type crowd in mind. This implies that the models are tested for moderate and high crowd densities, and moderate human velocities (walking). This report documents the development of a new numerical crowd dynamics model. The model is designed to be a robust simulation tool capable of handling both normal pedestrian scenarios as well as more extreme scenarios like a riot. This means that the model must be able to handle widely different human crowds, both in terms of crowd density and in terms of human velocities. The size of the simulated crowd could range from a few tens (or smaller in validation tests) to a few thousand people, and the time scale of the scenarios could vary from a fraction of a minute to hours. Ultimately, the model is meant to become a supplement to the purely phenomenological descriptions in the study of crowd events where LLWs are relevant. To achieve this, we will in future have to extend the basic crowd model described in this work with models of different LLWs, as well as more advanced models for decision-making and human motivation.

In the current work, we focus on the development of a numerical model for the simulation of human crowds based on the agent force modelling concept (Helbing & Molnár, 1995). An important issue is finding the right level of complexity in the model, and this means minimizing the number of free parameters as much as possible without neglecting important aspects of crowd behaviour. The basic assumption for the model is that as density in a human crowd increases, so do the limitations on the movement of individuals. The human body itself has certain characteristics when it comes to compressibility, constitutive properties, speed limitations and so forth. Furthermore, we need to take into account that solid obstacles will prevent or at least slow down the crowd flow. From these observations, we can formulate a set of basic forces that in principle can have great effect on human behaviour. Next, it is a fair assumption that humans manage to optimize their body movement with respect to the object or goal of the individual. Obviously, it is beyond the scope of the model to describe in detail the vast number of forces involved in reproducing optimised body movements. However, we can provide simplified force models to make individuals capable of avoiding solid obstacles and maintaining

a moderate speed when moving unhindered.

So what about less easily quantifiable effects from for instance psychological and social factors? Obviously, these effects will in many cases be very important in order to accurately predict the effectiveness of LLWs. Decision-making by individuals in a crowd, in particular individuals with a leading role in a group, can have a substantial effect on the overall outcome of e.g. a crisis. Models failing to take these effects into account will in certain scenarios fail at providing adequate predictions. Still, a simplified model can nevertheless provide us with important information. In this work, the strategy is to start out with a simple model where psychological and social factors are kept to a minimum. Well aware of the limitations of such a model, the plan is in future to gradually extend the applicability of the model by including additional non-physical effects.

This report is organized as follows: Section 2 reviews observational data on the biomechanical properties of the human body which are important when simulating human crowds. It also gives an overview of the equations of motion and explains how we can estimate crowd density and calculate the interaction range. In section 3, we look at the internal forces that represent desired movements, capabilities and limitations associated with each individual agent. The inter-agent forces are responsible for trying to keep individual agents separated at distances larger than some reasonable minimum distance. These forces are described in section 4. Similar forces associated with the agents interactions with solid boundaries are covered in section 5. Important model parameters not specified earlier, are determined in section 6 on the basis of simplified simulations and semi-analytic models. Full-scale simulations on a selection of more or less well-known crowd dynamics tests are presented in section 7 and compared with results from literature. A conclusion is provided in section 8. More in-depth information on aspects of the boundary interaction is provided in Appendix A and Appendix B.

2 Simulation model overview

This section serves several purposes. First, we establish an experimental framework in which the simulation model should fit. Next, the overall equations of motion are formulated and a suitable expression for the crowd number density is found. The last part of this section deals with interactions at a distance. This is relevant both for inter-agent and boundary forces. How the strength of such interactions will depend upon the choice of spatial interaction function, is described. The concepts of obstacle avoidance and crowd repulsion are also introduced, and variable interaction range is discussed.

2.1 Observations regarding human anatomy and behaviour

It is of vital importance for any numerical model to be given a firm analytic and/or experimental basis. A human crowd model should be no different. Some aspects of a crowd's behaviour could be described quite well by a fluid model. Other aspects are more likely to be

assicated with the granular nature of a human crowd. And yet again other aspects can only be described when considering the full psycho-social characteristics of individuals in the crowd.

2.1.1 Biomechanical properties of the human body

Although it has been a goal to minimize the number of free parameters by neglecting many of the psycho-social factors, the model will still rely on a fairly large number of parameters. Some of these parameters will have to be determined by fitting simulation results to observations of key crowd behaviour. However, many parameters can be determined, directly or indirectly, on the basis of biomechanical properties of the human body. Table 2.1 gives an overview of some important properties relevant in this work and references where this is applicable. The values refers to an adult human [1].

Parameter	Observed value	Reference
Shoulder width	0.4-0.5 m	Weidmann (1992)
The anteroposterior size	0.25-0.3 m	Weidmann (1992)
Shoe size	0.25-0.3 m	Weidmann (1992)
Mass	50-100 kg	—
Pedestrian walking speed	1.34m/s $\pm$ 0.26m/s	Weidmann (1992)
Fast running speed	6.0-8.0 m/s	Novacheck (1998)
Typical whole-body acceleration	0.1g	Kavanagh & Menz (2008)
Maximum muscle-driven acceleration	0.5-0.8g	Kugler & Janshen (2010)
Chest (low speed) spring force	300-1000 N/cm	Viano & King (2000)
Max. chest compression before injury	20%-40%	Viano & King (2000)
Critical 1-minute force asphyxia limit	1000 N	Fruin (1993)
Critical 10-second force asphyxia limit	6000 N	Fruin (1993)
Max. manual force on structures	30-75% of weight	Fruin (1993)
Min. distance to obstacles	0.75-1.50 m	Weidmann (1992)

Table 2.1 Biomechanical properties of the human body with typical values as derived from various empirical studies.

On the basis of the order of magnitude estimate of whole-body acceleration given in table 2.1, we can use a simple analysis to determine roughly at what range the interactions must become effective if collisions with obstacles in the flow path are to be avoided. If we assume an initial velocity v_0 and a mean acceleration $\bar{a}$, the minimum effective range for the interaction must be

$$s_{\min} = v_0^2/(2\bar{a}). \tag{2.1}$$

We see that the required range is highly dependent on the relative velocity between the agent and the obstacle. If the obstacle also is a moving agent, both v_0 and $\bar{a}$ will be twice as large. If

[1] The current simulation model makes the simplifying assumption of a circular human cross-section, typically with an effective diameter of 0.3-0.4 m.

both agents are running towards each other at a speed of 5-6 m/s, and we assume a mean acceleration of around 0.1g, then the interaction between the two should have a range of roughly 30 m. This will ensure that a direct collision is avoided with a reasonable acceleration magnitude.

2.1.2 Assumptions regarding fundamental human behaviour in crowds

A crowd model cannot be constructed using biomechanical properties and mathematics alone. The development must also be guided by observations and assumptions regarding human behaviour in a crowd. In this section, I have tried to list the main assumptions used in developing the current model.

1. Local density is the primary parameter in determining the dynamics of a crowd.

2. Isolated agents have a large interaction range. This interaction range decreases with increasing density.

3. Agents optimize their movements so as to minimize energy consumption and maximize efficiency.

4. Agents will try to navigate around limited-sized obstacles. Body forces are adjusted according to velocity so that the minimum distance to obstacles and other agents becomes only weakly dependent on the original velocity.

5. A pair of agents in a crowd experience a mutual repulsive effect if they are not familiar with each other. This holds even though the two agents are not in danger of colliding. However, the repulsion is anisotropic so that a net posterior repulsion is experienced in a uniform crowd causing the average velocity in the crowd to drop with increasing crowd density.

6. In low density crowds, agents can easily maintain their preferred speed.

7. In high density crowds, agents will resort to moderate levels of pushing in order to try maintaining a non-zero velocity.

8. As an agent approaches the preferred location, the associated preferred speed drops to 0. How accurately the agent defines the preferred location is scenario dependent.

Some assumptions are trivial, while others are made from experimental work (Older, 1968; Parisi et al., 2009; Seyfried et al., 2009; Still, 2000; Weidmann, 1992). Some assumptions

have even come about simply as a result of the numerical challenges met in this work. The assumptions made will always have great impact on the model. If simulation results do not fit sufficiently well with observations, this could be an indication that the list of assumptions needs revising.

2.2 Introduction to the agent-based force model

In the choice between different modelling approaches, the agent-based, social force approach introduced by Prof. Dirk Helbing and his collaborators almost 20 years ago (Helbing & Molnár, 1995) was preferred. The idea behind the Helbing force model is to model crowd behaviour by formulating forces which describe interaction between pairs of persons, interaction between a person and a solid wall, and the self-propelling force which represents the own will of the person to move in a certain way. Each person (hereafter referred to as agent) a has attributes such as mass (m_a), physical diameter (d_a), position ($\boldsymbol{r}_a$), and velocity ($\boldsymbol{v}_a$). The basic equations of motion are:

$$\frac{d\boldsymbol{r}_a}{dt} = \boldsymbol{v}_a \tag{2.2}$$

and

$$m_a \frac{d\boldsymbol{v}_a}{dt} = \boldsymbol{\mathcal{F}}_a^{\mathcal{I}} + \sum_{b\in\mathcal{A}} \boldsymbol{\mathcal{F}}_{ab}^{\mathcal{A}} + \sum_{b\in\mathcal{B}} \boldsymbol{\mathcal{F}}_{ab}^{\mathcal{B}}. \tag{2.3}$$

The forces acting on agent a in the basic model are divided into 3 parts based on the object of interaction: $\boldsymbol{\mathcal{F}}_a^{\mathcal{I}}$ indicates the internal forces (often referred to as the will force), $\boldsymbol{\mathcal{F}}_{ab}^{\mathcal{A}}$ represents interactions with neighbouring agent b (where $\mathcal{A}$ is the set of all agents), and $\boldsymbol{\mathcal{F}}_{ab}^{\mathcal{B}}$ denotes interactions with solid boundary element b (where $\mathcal{B}$ is the set of all boundary elements). Each of the three groups of forces can be split up according to the characteristics of the interaction. This is illustrated in Fig. 2.1. The internal forces are split up into a displacement force dependent on the agent's position, a flow force dependent on the agent's velocity relative to the desired velocity, and a strain force dependent on the agent's velocity relative to a upper velocity limit. The inter-agent forces are either long-range social forces or contact forces. The former type of interactions include obstacle avoidance and crowd repulsion, while the latter type of interactions deals with direct physical contact and typically has both a normal and a transversal component. The boundary forces are formulated so as to match the inter-agent forces.

Local density is an important property when describing a crowd. Still, density is not included as a variable in the original Helbing model (Helbing, Farkas & Vicsek, 2000). Instead the model focuses to a large extent on close-range interactions, thereby making the model less suited for modelling low and moderate density crowds. Later attempts to correct this, utilized a crude density estimate (Lakoba, Kaup & Finkelstein, 2005). More recently, the link between crowd modelling and a fluid method known as Smoothed Particle Hydrodynamics (SPH) (see review in Monaghan (2005)) was pointed out by Vetter et al. (2011). According to this method,

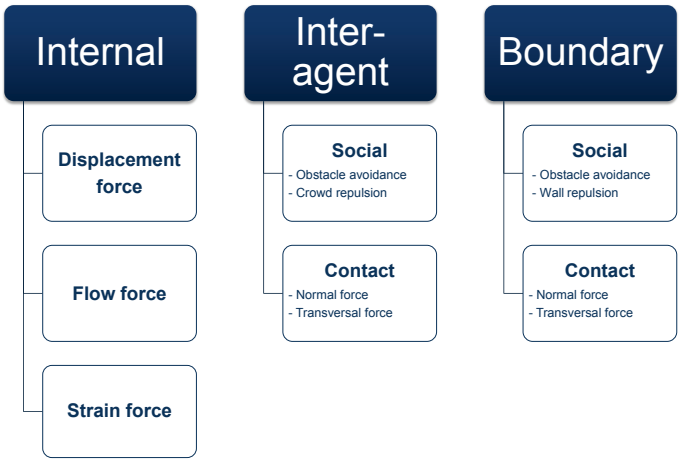

Figure 2.1 Forces in the basic agent model are sorted in 3 groups according to the object of interaction.

the density at the position of an agent a, denoted ρ_a, is calculated as

$$\rho_a = \sum_b \mathcal{W}_{ab}. \tag{2.4}$$

where $\mathcal{W}_{ab} \equiv \mathcal{W}(r_{ab}/h_{ab}, h_{ab})$ is a smoothing kernel. The kernel is dependent on r_{ab}, the distance between agents a and b, and the characteristic scale length h_{ab}, often referred to as the smoothing length, where h_{ab} is found as the mean smoothing length of the two agents. In this work, the chosen kernel is taken from Wendland (1995):

$$\mathcal{W}(\nu, h) = \frac{7}{64\pi h^2} \begin{cases} (2-\nu)^4(1+2\nu) & \text{if } 0 \leq \nu \leq 2; \\ 0 & \text{otherwise.} \end{cases} \tag{2.5}$$

The smoohting length, h_a, is itself dependent on ρ_a, so that Eq. 2.4 in reality is a non-linear equation (see section 2.5.3 for details). Note also that the density at the location of an agent a will never be zero because the agent itself contributes to the sum in Eq. 2.4 by the amount $\mathcal{W}(0, h_a)$.

2.3 Spatial interaction function

A main challenge in developing a robust crowd model is to describe human movement with sufficient degree of accuracy both in low and high density scenarios. In low density crowds, agents should make appropriate modifications to their path based on the location and relative speed of any obstacles, even when these obstacles are still far from the agent. In high density crowds, the interactions should in general be restricted to a much smaller region. In order to improve efficiency and accuracy, the range of the inter-agent and boundary forces should be

linked to the local crowd number density. The effective interaction range will depend both on the shape of the spatial interaction function and the scale length.

In the Helbing model, the spatial interaction function used for social forces is exponentially decaying with the normalized distance from the physical radius of the agent. The blue curve in Fig. 2.2 shows this function in a logarithmic plot. Because of the chosen functional form, the interaction strength will drop off quickly with normalized distance. Increasing the scale length will only to a limited degree help avoiding dynamical effects that resemble colliding billiard balls. Note that this refers to the interaction strength for a single pair of interacting agents. If we assume a uniform crowd, the relative interaction strength from all agents at a given distance can be found by multiplying the curves in Fig. 2.2 with the distance. Even so, the interaction force in the original Helbing model drops off very quickly with normalized distance.

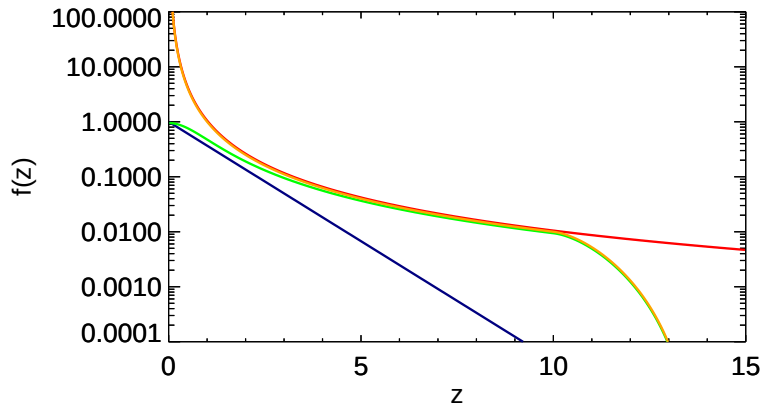

Figure 2.2 *Comparison of different spatial interaction functions as functions of the normalized distance from the chosen origin. The blue, red, orange and green curves correspond to the exponential function, the Coloumb function, the tapered Coloumb function, and the tapered and softened Coloumb function.*

Drawing parallels to systems governed by electrostatic or gravitational forces, a new spatial interaction function, referred to as a Coloumb function, is proposed. This function will in its original form be written as

$$\Phi_0(z, \epsilon) = \frac{1}{z^2 + \epsilon^2}, \tag{2.6}$$

where ϵ is an optional softening parameter to avoid the singularity at $z = 0$. The case with $\epsilon = 0$ is illustrated in Fig. 2.2 by the red curve. Notably different than the exponential function, the Coloumb function goes to infinite at $z = 0$ and drops off very slowly for large values of z. The latter behaviour could lead to a very large effective interaction range. However, this is avoided by adding a taper function Ψ at an appropriate distance. Apart from the functional form, in this work chosen to be equal to the smoothing kernel defined in Eq. 2.5, Ψ is characterized by the **taper start distance**, z_0, and the **taper half width**, z_w. These two parameters defines the taper

variable $\xi = (z - z_0)/z_w$. The taper function itself can then be written as

$$\Psi(\xi) = \begin{cases} 1 & \text{if } \xi \leq 0; \\ \frac{1}{16}(2-\xi)^4(1+2\xi) & \text{if } 0 < \xi \leq 2; \\ 0 & \text{otherwise}, \end{cases} \tag{2.7}$$

By multiplying the original Coloumb function Φ_0 with the taper function Ψ, we get a **compactly supported** interaction function

$$\Phi(z, \epsilon) = \Phi_0(z, \epsilon)\Psi\left(\frac{z - z_0}{z_w}\right), \tag{2.8}$$

which means that $\Phi(z, \epsilon)$ is exactly zero beyond the cut-off distance $z_{\text{max}} = z_0 + 2z_w$. The orange curve in Fig. 2.2, shows the Coloumb function multiplied by the taper function with $z_0 = 10$ and $z_w = 2$. The green curve in Fig. 2.2 shows the corresponding Coloumb function with a softening parameter equal to 1.

2.4 Obstacle avoidance and crowd repulsion

Based on assumptions 4 and 5 listed in section 2.1.2, it is reasonable to divide the social interaction forces described in sections 4 and 5 into two separate effects: Agents need to be able to navigate in between nearby obstacles, whether it be other agents or solid barriers. At the same time, agents will interact with a neighbouring crowd of people if the crowd density is non-negligible. The former type of interaction, which we will refer to as **obstacle avoidance**, is in nature a point-point interaction. The latter type of interaction, which we will call **crowd repulsion**, could be considered more of a fluid type force.

Obstacle avoidance, or simply avoidance, deals with how agents avoids isolated obstacles in the preferred path. This is usually important in low density regions where the concept of a crowd is somewhat misleading, or simply when the distance to a single obstacle/neighbouring agent is considerably smaller than the typical agent separation. The number of neighbouring agents which gives rise to a non-zero avoidance interaction should therefore be more or less independent of density with a relative strong emphasis on the nearest obstacles/neighbouring agents. The tapered Coloumb function with zero softening (corresponding to the orange curve in Fig. 2.2) could be well suited for describing the avoidance effect. Since the contact force between two agents becomes non-zero for distances less than the mean agent diameter, d, we require the normalized avoidance distance at the agent diameter to be equal to unity. For distances larger than the agent diameter, the avoidance distance is normalized by the avoidance scale length, b_A.

The crowd repulsion on the other hand, describes the almost pressure-like forces that an agent experiences from a larger crowd or boundary structure. A fluid description could therefore be considered more appropriate in describing this type of interaction (Vetter et al., 2011). However, it is beyond the scope of the current work to explore this possibility. Instead of a

fluid formulation, crowd repulsion is described with a formulation similar to that used for obstacle avoidance, although with some important differences. Because of its nature, the crowd repulsion should become gradually more important as the density is increased. This implies that the number of crowd interactions should be zero when the density is very low, and gradually increase as density increases. This type of interaction should not put a very strong emphasis on single obstacles/neighbouring agents. But just as with avoidance interaction, it is practical to have an interaction function with compact support (finite interaction range). The tapered Coloumb interaction function with the softening parameter equal to 1 is a suitable starting point for the crowd repulsion model. Distance will be normalized by the corresponding scale length, referred to as b_C.

2.5 Variable interaction range

The number of interactions per agent, N_b, in a uniform crowd is dependent on the interaction range R and the density ρ, and is given as $N_b = \pi R^2 \rho$. If R was to be constant, then N_b would increase too rapidly for an efficient and accurate description to be achieved both in high and low density crowds. If, on the other hand, we let $R \propto \rho^{-1/2}$, this would lead to a roughly constant N_b. This would fit the description of the obstacle avoidance, but would not enable us to model density dependent crowd phenomena like the fundamental diagram (Schadschneider et al., 2009). For the modelling of the crowd repulsion, a weaker dependence of R on ρ is required, e.g. $R \propto \rho^{-1/4}$. In this section, the algorithms for determining the scale lengths, b_A and b_C, as functions of density will be presented.

2.5.1 Obstacle avoidance scale length

Based on the description of obstacle avoidance given in section 2.4, we find that the avoidance interaction range, R_A, depends on the corresponding scale length (b_A), the normalized cutoff distance for the tapered Coloumb function (z_{max}), and the agent diameter (d) as

$$R_A = (z_{\text{max}} - 1) b_A + d. \tag{2.9}$$

As already mentioned, $R_A \propto \rho^{-1/2}$ would imply a roughly constant number of avoidance interactions which could be expressed as

$$N_A = \pi R_A^2 \rho \equiv \pi R_{A,\text{ref}}^2 \rho_{\text{ref}}. \tag{2.10}$$

Since N_A is independent of density, we can safely express N_A using a reference density, ρ_{ref}, and a reference interaction range, $R_{A,\text{ref}}$. Combining Eqs. 2.9 and 2.10, we can get an expression for the reference scale length, $b_{A,\text{ref}}$ as

$$b_{A,\text{ref}} = \frac{1}{z_{\text{max}} - 1} \left[\left(\frac{N_A}{\pi \rho_{\text{ref}}} \right)^{1/2} - d \right]. \tag{2.11}$$

In order to avoid a singularity at $\rho = 0$, we allow the scale length to deviate from a strict

$\rho^{-1/2}$-dependence and choose the following dependence on density:

$$b_A = b_{A,\text{ref}}\left(\frac{\rho_{\text{ref}} + \rho_{A,\text{min}}}{\rho + \rho_{A,\text{min}}}\right)^{1/2}. \tag{2.12}$$

The additional parameter $\rho_{A,\text{min}}$ is chosen so that $b_A = b_{A,0}$ if $\rho = 0$. This implies that $\rho_{A,\text{min}}$ can be written as

$$\rho_{A,\text{min}} = \frac{\rho_{\text{ref}}}{(b_{A,0}/b_{A,\text{ref}})^2 - 1}. \tag{2.13}$$

To summarize, obstacle avoidance is characterized by the maximum scale length, $b_{A,0}$, the typical number of interactions, N_A, and to a much lesser degree on ρ_{ref}. From the discussion in section 2.1.1, we have that the interaction range should be as large as around 30 m to avoid collisions with other agents if both agents are running. If $z_{\text{max}} = 14$ as shown in Fig. 2.2, this implies that $b_{A,0} \approx 2$ m is a good choice. A suitable choice for N_A might be 5. The reference density, ρ_{ref}, should be small compared to relevant levels of crowd density, which is on the order of unity. We will set $\rho_{\text{ref}} = 0.1$ m^{-2}. If d is roughly 0.5 m as indicated in Table 2.1, then $b_{A,\text{ref}}$ and $\rho_{A,\text{min}}$ become roughly 0.29 m and $1.8 \cdot 10^{-3}$ m^{-2}, respectively.

2.5.2 Crowd repulsion scale length

A similar discussion can be presented when it comes to crowd repulsion. The relation between the interaction range R_C and the scale length b_C is

$$R_C = z_{\text{max}} b_C. \tag{2.14}$$

The number of crowd interactions, N_C, is not in this case independent of density. Instead, we specify an optimal number of interactions $N_{C,\text{max}}$ at a given large density ρ_{max}. Note that we are completely free in choosing the value of ρ_{max}. We can e.g. set ρ_{max} equal to a realistic maximum crowd density value. The corresponding $N_{C,\text{max}}$ will then indicate an upper limit to the number of crowd interactions per agent. This number is expressed as :

$$N_{C,\text{max}} = \pi R_C^2 \rho_{\text{max}} \equiv \pi z_{\text{max}}^2 b_{C,\text{max}}^2 \rho_{\text{max}}. \tag{2.15}$$

Choosing the crowd interaction range to be proportional to $\rho^{-1/4}$, we can formulate the crowd scale length, b_C, in a similar way as we did with b_A in Eq. 2.12 as

$$b_C = b_{C,\text{ref}}\left(\frac{\rho_{\text{ref}} + \rho_{C,\text{min}}}{\rho + \rho_{C,\text{min}}}\right)^{1/4}. \tag{2.16}$$

By combining Eq. 2.15 and 2.16 with $\rho = \rho_{\text{max}}$, and assuming $\rho_{\text{max}} \gg \rho_{C,\text{min}}$, we find that $b_{C,\text{ref}}$ can be expressed as

$$b_{C,\text{ref}} = \left[\frac{N_{C,\text{max}}}{\pi z_{\text{max}}^2 \rho_{\text{max}}^{1/2} (\rho_{\text{ref}} + \rho_{\text{min}})^{1/2}}\right]^{1/2}. \tag{2.17}$$

We use the same reference density as in the case of obstacle avoidance, and again, we link the density parameter $\rho_{C,\text{min}}$ to a maximum scale length $b_{C,0}$ which corresponds to the case $\rho = 0$.

So by combining Eq. 2.17 and Eq. 2.16 with $\rho = 0$, we get

$$\rho_{C,\text{min}} = \frac{N_{C,\text{max}}^2}{\pi^2 z_{\text{max}}^4 b_{C,0}^4 \rho_{\text{max}}}. \tag{2.18}$$

Since crowd repulsion is considered a fluid-like effect in this model, the number of interactions per agent should be substantially larger than what was the case for the obstacle avoidance in crowds of medium and high densities. At the same, we must consider the computational expense of having a large number of interactions per agent. Since the crowd repulsion scale length has a weaker dependence on the density than the avoidance scale length, a smaller maximum scale length must be chosen in this case. A suitable choice could be $b_{C,0} = b_{A,0}/2 = 1.0$ m. For $\rho_{\text{max}} = 6$ m^{-2}, an acceptable number of interactions, both with regards to accuracy and efficiency, would be $N_{C,\text{max}} \sim 50$. From Eq. 2.18, we then calculate $\rho_{C,\text{min}}$ to be equal to $1.1 \cdot 10^{-3}$ m$^-2$. And finally, we find $b_{C,\text{ref}} = 0.32$ m from using Eq. 2.18.

2.5.3 Comparison of scale lengths and robust calculation of smoohting length

The solid and dashed lines in Fig. 2.3 illustrate how the characteristics of the obstacle avoidance and crowd repulsion, respectively, change with changing density. In the left panel, the avoidance scale length is seen to drop quickly as the density increases from 0 to the reference density at 0.1 m^{-2}. The crowd scale length is a factor of two smaller than the avoidance scale length at zero density, but drops more slowly than the latter. So for ρ larger than roughly $\rho_{\text{ref}}/2$, the crowd scale length is larger than the avoidance scale length. The grey, dashed line in the same panel shows the mean agent separation divided by the normalized cut-off distance z_{max}. By comparing this curve with the other two curves, we can conclude that in a uniform crowd, the obstacle avoidance range will never be much larger than the agent separation whereas the crowd repulsion range becomes significantly larger than the agent separation for large densities.

The middle panel illustrates how the interaction strength at 3 different distances vary with density. Assuming a uniform crowd, the average inter-agent separation Δ is roughly given as $\Delta = \rho^{-1/2}$. The red, green, and blue lines in the middle panel correspond to the density-dependent distances $\Delta/2$, Δ, 2Δ. The first case corresponds to a particularly close-by neighbour. In accordance with the general description in section 2.4, the obstacle avoidance dominates over the crowd repulsion for all densities except in the intermediate density range of roughly $0.01 - 1$ m^{-2}. The second case represents the normal minimum distance to neighbours. Here, the intermediate density range where crowd repulsion dominates has been extend up to $\rho \approx 3$ m^{-2}. The third case corresponds to a neighbour which is not among the nearest neighbours. In this case, the interaction strength is small everywhere except for the crowd repulsion in high density regions.

The right hand panel of Fig. 2.3 shows how the number of interactions per agent changes with density. In the avoidance case, the number of interactions is more or less constant as expected. Only at very low densities does the number of interactions drop. In the crowd case, the number of interactions has a very different density variation: The increase is small for very

low densities. For densities above the reference density, the number of interactions increases very rapidly. As specified by the input parameters, 50 interactions per agent are found at $\rho = 6\ \mathrm{m}^{-2}$.

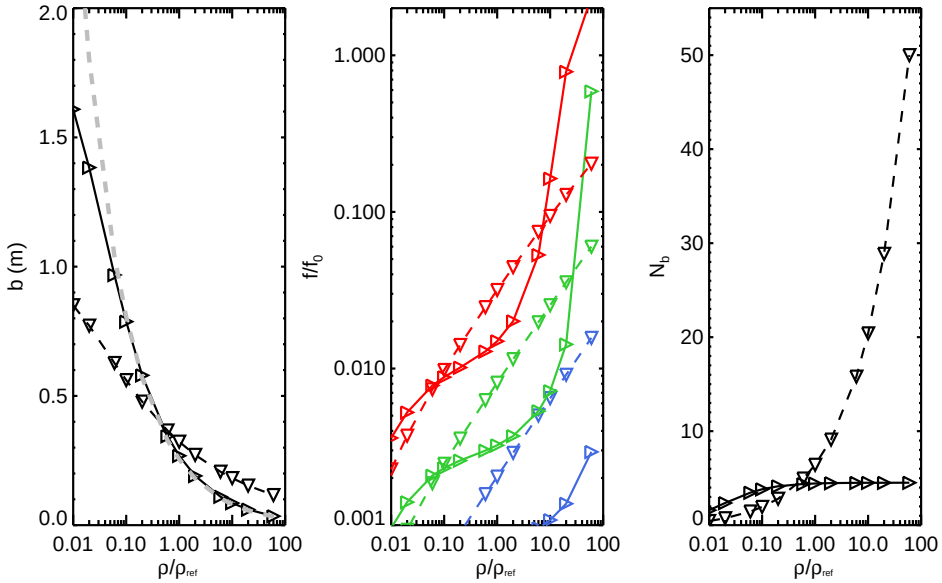

Figure 2.3 *Characteristics of the obstacle avoidance (solid lines) and crowd repulsion (dashed lines) as functions of crowd density. The left, middle, and right panels show the scale length, the normalized interaction strength, and the number of interactions. The grey curve in the left hand plot shows Δ/z_{max}, where $\Delta = \rho^{-1/2}$. The red, green, and blue curves in the middle panel correspond to interaction distances $\Delta/2$, Δ, and 2Δ.*

Now, let us return to the question of how the density is calculated. Eq. 2.4 described how this is done by adding weighted contribution from agents within a certain interaction range. From the expression of the weight function given in Eq. 2.5, we see that the interaction range in this case is given as $2h$, where h was referred to as the smoothing length. The smoothing length should in itself be dependent on density, much as the avoidance and crowd scale lengths, and this makes Eq. 2.4 non-linear. To achieve accurate but also smoothly varying density estimates, the range of the weight function is made equal to the range of the crowd repulsion. This implies that h can be expressed as

$$h = \frac{z_{\max}}{2} b_C. \tag{2.19}$$

The non-linear nature of Eq. 2.4 needs special considerations. If the initial density is very low, we know from the right-hand panel of Fig. 2.3 that the number of crowd interactions is small. As a consequence, the density estimate can fluctuate substantially, especially since the distribution of agents often are highly inhomogeneous in low density regions. Also in such cases, the contribution from an agent a to its own density, hereafter referred to as the density

self-contribution, is important. It is equal to $\mathcal{W}(0, h_a)$ which is proportional to h_a^{-2}. This means that a small increase in density, which in turn leads to a decrease in h_a, can have a potential feedback effect on the density estimate causing the density to increase even further. In fact, if we assume the total density is dominated by self-contribution, then it can be easily shown that there exists an equilibrium value of the crowd scale length, b_C, which is about 70% smaller than $b_{C,0}$, the maximum value of b_C, given as input in section 2.5.2. For the avoidance scale length, b_A, the difference between $b_{A,0}$ and the maximum scale length in real simulations becomes even larger.

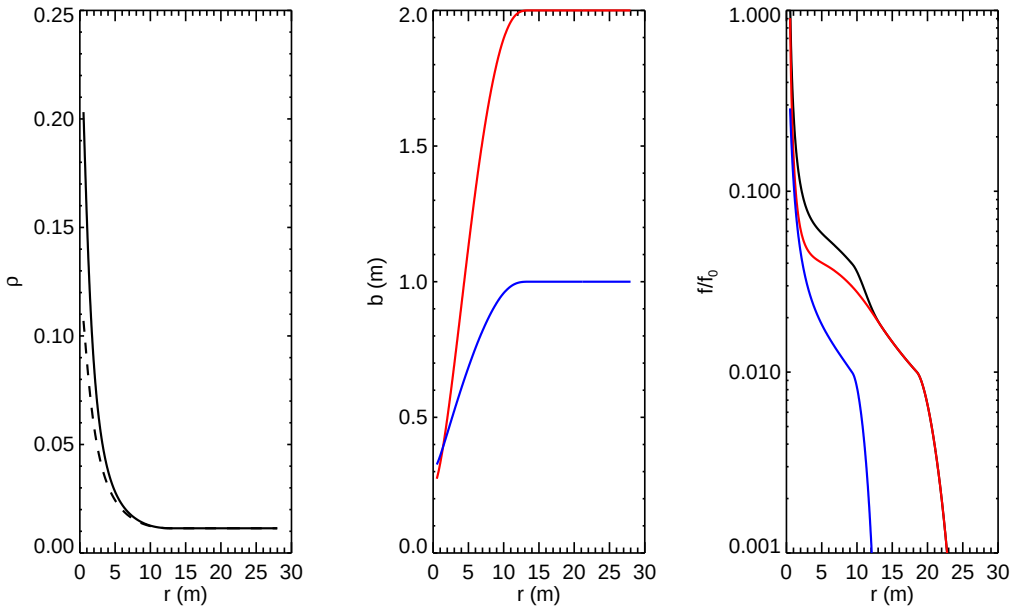

Figure 2.4 *Characteristics of the interaction between two agents as functions of separation. The solid line in the left panel shows the total density in a two-agent system, while the dashed line in the same panel shows the corresponding density self-contribution. The middle and right-hand panels show the scale length and normalized interaction strength, respectively. Obstacle avoidance and crowd repulsion are indicated by red and blue curves, respectively, while the black curve in the latter panel indicates the total interaction strength.*

To avoid this problem, it is proposed to calculate the scale lengths by replacing ρ in the denominators of Eqs. 2.12 and 2.16 with $\rho^\star = \rho - \mathcal{W}(0, h)$, the density without the density self-contribution. The strength of the non-linear coupling between h and ρ in the low-density regime is thus weakened substantially. This makes it easier to achieve a robust algorithm for calculating the interaction scale lengths. Nevertheless, the non-linearity of Eq. 2.4 can give rise to temporal oscillations in the scale lengths. To avoid this, we calculated the crowd scale length at time step t as

$$b_C^t = \frac{1}{2}[b_c^{t-1} + \hat{b}_c^t], \tag{2.20}$$

where b_c^{t-1} is the scale length from the previous time step and $\hat{b}_c^t$ is calculated by Eq. 2.16 with $\rho = \rho^{t-1}$, the density estimate from the previous time step.

To illustrate the change in interaction scale lengths in the low density regime, we take a look at a simple case where two isolated agents approach each other. We assume standard input parameters as described in sections 2.5.1 and 2.5.2. Characteristics of the interaction between the two agents as functions of separation are shown in Fig. 2.4. The left-hand panel shows the density (solid line) and density self-contribution (dashed line). We see that the density can become as large as 0.2 m^{-2} if the agents come sufficiently close. This corresponds to the density of a uniform crowd where the typical separation is around 2.2 m. The dashed line indicates that the self-contribution also increases as the two agents approach each other. The middle panel illustrates how the obstacle avoidance (red curve) and crowd repulsion (blue curve) scale lengths drop as the separation between the two agents is reduced. Note that the latter scale length is only bigger than the former when the separation is smaller than about 1.5 m. The right-hand panel shows the corresponding interaction strength for the two interaction types together with the total interaction strength (black curve). Obstacle avoidance becomes significant already at 15-20 m, while crowd repulsion gives negligible contribution to the total interaction for separations larger than 10 m or so.

3 Internal forces

Internal forces are introduced to model the fundamental ability of agents to make choices regarding their own movement. Such a description should include any limitations of this ability dictated by the human body. The classic model incorporates a will force, as it is often referred to, in a simple manner by having a force which depends exclusively on the difference between the preferred and actual velocity (Helbing, Farkas & Vicsek, 2000). The preferred velocity itself (denoted by $\boldsymbol{u}_a$) can vary in time and be related to the displacement from the preferred location (denoted by $\boldsymbol{z}_a$). If the applications are restricted to cases where all agents move at roughly the same, moderate speed, this formulation gives satisfactory results. However, we want to consider applications where agents might have widely different (preferred) velocities. We also have to take into account that the preferred locations are defined with varying degrees of accuracy. And finally, we must consider the possibility that different forces acting constructively might result in unrealistically large accelerations or might accelerate agents to unrealistically large velocities. With this in mind, we formulate an internal force containing three components, a displacement force, a flow will force, and a strain force: $\boldsymbol{\mathcal{F}}_a^{\mathcal{I}} = \boldsymbol{\mathcal{R}}_a^{\mathcal{I}} + \boldsymbol{\mathcal{V}}_a^{\mathcal{I}} + \boldsymbol{\mathcal{S}}_a^{\mathcal{I}}$.

3.1 Displacement force

The first component ($\boldsymbol{\mathcal{R}}_a^{\mathcal{I}}$) is directly dependent on the displacement $\boldsymbol{\delta z}_a = \boldsymbol{z}_a - \boldsymbol{r}_a$ from the preferred location. Let σ_a denote a scale length that indicates how accurately agent a targets the preferred location. Out of convenience, we also define $\tilde{\sigma}_a = \sigma_a / \ln 2$. The force attracting the

agent to the preferred location is then defined as

$$\boldsymbol{\mathcal{R}}_a^{\mathcal{I}} = m_a A^r_{\text{will}} \left\{ \exp\left(-\frac{\delta z_a}{\tilde{\sigma}_a}\right) - \exp\left(-\frac{2\delta z_a}{\tilde{\sigma}_a}\right) \right\} \frac{\boldsymbol{\delta z}_a}{\|\boldsymbol{\delta z}_a\|}. \tag{3.1}$$

The attraction to the preferred location is at its largest at a distance of σ_a, and the constant A^r_{will} determines the maximum strength of the displacement force. Although σ_a is a problem-dependent parameter, we will assume that $\sigma_a \geq \sigma_{\text{min}}$, σ_{min} is a model constant to be determined later. It is also reasonable to include a damping force acting on agents when they are close to their preferred location. The damping force can be formulated as an additional term in the momentum equation which is proportional to both the velocity (Monaghan, 2005) and the spatial weight factor $\exp(-\delta z_a/\sigma_a)$.

3.2 Flow will force

The second component ($\boldsymbol{\mathcal{V}}_a^{\mathcal{W}}$) depends primarily on the difference in preferred and actual velocity. However, according to assumption 8 in section 2.1.2, there should also be a natural softening of the force when the agent comes within the preferred location range σ_a. First, let us define the softening parameter γ_a as

$$\gamma_a = \begin{cases} \frac{\delta z_a}{\sigma_a} & \text{if } 0 \leq \delta z_a < \sigma_a; \\ 1 & \text{otherwise.} \end{cases} \tag{3.2}$$

The softened preferred velocity is defined as

$$\boldsymbol{u}_a = \tilde{u}_a \gamma_a \frac{\boldsymbol{\delta z}_a}{\|\boldsymbol{\delta z}_a\|}, \tag{3.3}$$

where $\tilde{u}_a > 0$ is the unsoftened preferred speed during movement. It is also convenient to define the normalized preferred velocity vector $\hat{\boldsymbol{u}}_a = \frac{\boldsymbol{u}_a}{\tilde{u}_a}$, and it is trivial to see that $\|\hat{\boldsymbol{u}}_a\| = \gamma_a \leq 1$.

The flow will force is divided into two parts. The first part is a driving force term in the direction of the preferred velocity, while the second force term dampens movement perpendicular to the preferred velocity. First, we define the parallel and perpendicular velocity components,

$$v_{\parallel,a} = \boldsymbol{v}_a \cdot \hat{\boldsymbol{u}}_a \tag{3.4}$$

and

$$\boldsymbol{v}_{\perp,a} = \gamma_a \boldsymbol{v}_a - v_{\parallel,a} \hat{\boldsymbol{u}}_a, \tag{3.5}$$

respectively. Then, we define the corresponding normalized velocity deviations from preferred velocity:

$$x_{\parallel,a} = \frac{\|\boldsymbol{u}_a\| - v_{\parallel,a}}{\tilde{u}_a} \tag{3.6}$$

and

$$\boldsymbol{x}_{\perp,a} = -\frac{\boldsymbol{v}_{\perp,a}}{\tilde{u}_a}. \tag{3.7}$$

The flow will force, $\boldsymbol{\mathcal{V}}_a^{\mathcal{I}}$, can then be written as

$$\boldsymbol{\mathcal{V}}_a^{\mathcal{I}} = m_a A_{\text{will}}^v [\Gamma(x_{\parallel,a})\hat{\boldsymbol{u}}_a + \boldsymbol{x}_{\perp,a}], \tag{3.8}$$

where A_{will}^v is the flow will acceleration amplitude and $\Gamma(x)$ is a non-linear force amplifier.

3.2.1 Non-linear flow will

The original flow will force formulation is a strictly linear function of velocity (Helbing, Farkas & Vicsek, 2000). It is meant to describe the tendency of an agent to try maintain the preferred velocity in spite of external forces acting on the agent. Linear models are often considered first order approximations to more complex processes. For instance, are linear models often valid only under the assumption of small deviations from an equilibrium state. In the case of the flow will force, assumptions 6 and 7 listed in section 2.1.2 lead us to identify 2 regimes, for $x \ll 1$ and $x \sim 1$, where a non-linear flow will behaviour might be appropriate. In situations where a weak but nearly static external force acts on an agent, the deviation from the preferred velocity should be almost negligible. This is because the agent can easily balance the external forces with a moderate will force. Compared to the velocity deviation, though, the required will force might be superlinear. In situations where the external forces are large, the agent might nearly stop or even move in the opposite direction relative to the preferred velocity. If this is the case, it is likely that the agent will exhibit enhanced determination or even resort to pushing to secure a minimum of movement in the correct direction. To model this behaviour appropriately, a non-linear force is also required.

The force amplifier $\Gamma(x)$ is defined as:

$$\Gamma(x) = \begin{cases} b_0 x^2 + c_0 x & \text{if } 0 \leq x < x_0; \\ b_1 x^2 + c_1 x + d_1 & \text{if } x_0 \leq x < x_1; \\ x & \text{if } x_1 \leq x \leq x_2; \\ a_2 x^3 + b_2 x^2 + c_2 x + d_2 & \text{otherwise}. \end{cases} \tag{3.9}$$

The coefficients can be determined by requiring $\Gamma(x)$ and its first derivative to be continuous in the interval $0 < x < 1$ and the second derivative to be continuous in the interval $x_1 < x < 1$. The amplification at $x = x_0$ is equal to $x_{1/2} = (x_0 + x_1)/2$. The amplification at $x = x_2$, Γ_2 is

a free parameter. The force amplification coefficients are then given as

$$
\begin{aligned}
b_0 &= -\frac{x_{1/2}}{x_0^2}, && (3.10)\\
c_0 &= 2\frac{x_{1/2}}{x_0}, && (3.11)\\
b_1 &= \frac{1}{2(x_1 - x_0)}, && (3.12)\\
c_1 &= -\frac{x_0}{x_1 - x_0}, && (3.13)\\
d_1 &= \frac{x_1^2}{2(x_1 - x_0)}, && (3.14)\\
a_2 &= (\Gamma_2 - 1)/(1 - 3x_2 + 3x_2^2 - x_2^3), && (3.15)\\
b_2 &= -3a_2x_2, && (3.16)\\
c_2 &= 1 + 3a_2x_2^2, && (3.17)
\end{aligned}
$$

and

$$
d_2 = -a_2x_2^3. \qquad (3.18)
$$

The shape of the amplifier is shown in Fig. 3.1 for $\Gamma_2 = 2$. Although the parameters $x_0 - x_2$ can be set independent of each other, the plot only shows 3 choices of (x_0, x_1, x_2), namely $(0.05, 0.1, 0.5)$ (solid curve), $(0.05, 0.2, 0.7)$ (dotted curve), and $(0.05, 0.4, 0.9)$ (dashed curve).

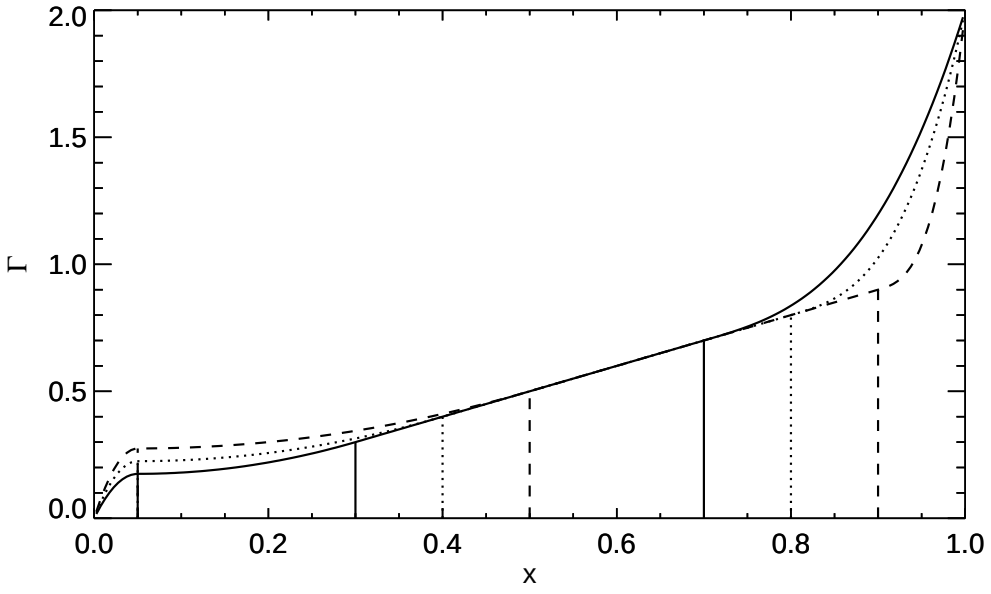

Figure 3.1 Non-linear will force amplifier $\Gamma(x)$ with $\Gamma_2 = 2$. The solid, dotted, and dashed lines correspond to $(x_0, x_1, x_2) = (0.05, 0.3, 0.7)$, $(x_0, x_1, x_2) = (0.05, 0.4, 0.8)$, and $(x_0, x_1, x_2) = (0.05, 0.5, 0.9)$, respectively.

3.3 Strain force

External forces acting on an agent can be sorted into 2 fundamental categories. Contact forces are real forces that in extreme cases can give rise to sudden changes in the dynamics of agents, potentially leading to physical injury. Most other forces in a crowd model are pseudo forces. Although some of these forces are described as interactions with external entities, they are in reality caused by the agents' own bodies in response to decisions made by the agents. The strain force should reflect the physical limitations of the human body. For instance, the model should make sure that the magnitude of the total pseudo force does not become too large. Also, an agent should not be accelerated to unrealistically high velocities. In principle, the limitations on the human body could be time-dependent, representing the current physical (and psychological) state of individual agents. For now, we will restrict the strain force model to be universal and time-independent.

First, we deal with the limitation on velocity. Let $v_{\text{lim},0}$ denote the speed at which the straining force becomes non-zero, for instance 6 m/s. For speeds larger than $v_{\text{lim},0} + \delta v_{\text{lim}}$, for instance 9 m/s, the straining force should quickly become very large and strong damping occurs. To achieve this, we can define the **velocity strain force** for agent a as

$$\boldsymbol{\mathcal{S}}_{1,a}^{\mathcal{I}} = -m_a A_{\text{will}}^s \begin{cases} \left(\frac{\|\boldsymbol{v}_a\| - v_{\text{lim},0}}{\delta v_{\text{lim}}} \right)^3 \hat{\boldsymbol{v}}_a & \text{if } \|\boldsymbol{v}_a\| > v_{\text{lim},0}; \\ 0 & \text{otherwise}, \end{cases} \tag{3.19}$$

where $\hat{\boldsymbol{v}}_a$ is the unity vector in the flow direction of agent a and A_{will}^s is the velocity strain acceleration amplitude.

We also want to put restrictions on the pseudo forces acting on an agent by introducing what we call the **acceleration strain force**. First we need to defined the pseudo force acceleration of agent a as

$$\frac{d\boldsymbol{v}_a^p}{dt} = \frac{d\boldsymbol{v}_a}{dt} - \frac{d\boldsymbol{v}_a^c}{dt}, \tag{3.20}$$

where $\frac{d\boldsymbol{v}_a^c}{dt}$ is the corresponding acceleration due to contact force interactions. The magnitude of the pseudo force acceleration is written f_a^p for short. Let $f_{\text{lim},0}$ denote the acceleration at which the straining force becomes non-zero, for instance 0.5g, and let the upper limit to the pseudo forces be defined as $f_{\text{lim},0} + \delta f_{\text{lim}}$, for instance 1.0g. A normalized variable, $\eta = (f_a^p - f_{\text{lim},0})/\delta f_{\text{lim}}$, is then introduced. If $\eta \leq 0$, the pseudo force should not be reduced and the acceleration strain force becomes 0. However, if $\eta > 0$, the modified pseudo force magnitude is found as

$$\hat{f}_a^p = f_{\text{lim},0} + \delta f_{\text{lim}} \tanh(\eta). \tag{3.21}$$

The effective acceleration strain force then becomes

$$\boldsymbol{\mathcal{S}}_{2,a}^{\mathcal{I}} = -\left(1 - \frac{\hat{f}_a^p}{f_a^p}\right) m_a \frac{d\boldsymbol{v}_a^p}{dt}. \tag{3.22}$$

The total strain force is given as $\boldsymbol{\mathcal{S}}_a^{\mathcal{I}} = \boldsymbol{\mathcal{S}}_{1,a}^{\mathcal{I}} + \boldsymbol{\mathcal{S}}_{2,a}^{\mathcal{I}}$.

4 Inter-agent forces

The interaction between agents is formulated as a sum of interactions between pairs of agents. For each pair of agents, the interaction $\boldsymbol{\mathcal{F}}_{ab}^{\mathcal{A}}$ can be separated into a relatively long-range, social force (denoted $\boldsymbol{\mathcal{S}}_{ab}^{\mathcal{A}}$) and a short-range contact force (denoted $\boldsymbol{\mathcal{C}}_{ab}^{\mathcal{A}}$). The role of $\boldsymbol{\mathcal{S}}_{ab}^{\mathcal{A}}$ is to maintain a reasonable distance between adjacent agents under normal conditions, while $\boldsymbol{\mathcal{C}}_{ab}^{\mathcal{A}}$ accounts for the additional forces associated with direct, physical contact. When describing agent-agent interaction, it is useful to define the separation vector, $\boldsymbol{r}_{ab} = \boldsymbol{r}_b - \boldsymbol{r}_a$, the relative velocity, $\boldsymbol{v}_{ab} = \boldsymbol{v}_b - \boldsymbol{v}_a$, and the mean mass, $m_{ab} = (m_a + m_b)/2$.

4.1 Social force

The concept of a social force was originally presented in Helbing & Molnár (1995) and the most common approach has been to use a force which is strictly radial, anisotropic, but independent of velocity. In this section, we will look at the social force model adopted in the current work. As described in section 2.4, the social force is split into 2 types of interactions: obstacle avoidance and crowd repulsion. The social force on agent a from agent b is therefore written as

$$\boldsymbol{S}_{ab}^{\mathcal{A}} = \boldsymbol{S}_{1,ab}^{\mathcal{A}} + \boldsymbol{S}_{2,ab}^{\mathcal{A}}, \tag{4.1}$$

where the indices 1 and 2 refer to obstacle avoidance and crowd repulsion, respectively. The corresponding interaction scale lengths for the two types of interactions were found in sections 2.5.1 and 2.5.2. In this section, we will take a closer look at how these interactions are formulated.

4.1.1 Obstacle avoidance interaction

The construction of the obstacle avoidance formulation is primarily guided by assumptions 3 and 4 listed in section 2.1.2. For this reason, the interaction is dependent on both the separation and the velocity difference between the two agents, and the force includes both a radial component and a normal component. While the first component can be seen as being analogous to the electrostatic force, the second component resembles the magnetic force (Yu et al., 2005).

First, let us consider the radial force component for a pair of agents a and b. The velocity dependence of the component, formulated as a function of the relative, radial velocity, is determined by a simple linear function, denoted $\Upsilon(v_{ab,r})$, defined as

$$\Upsilon(v_{ab,r}) \equiv \Upsilon_{ab} = \begin{cases} \frac{v_{ab,r}}{v_{\text{ref}} + v_{ab}} & \text{if } v_{ab,r} \geq 0; \\ 0 & \text{otherwise}, \end{cases} \tag{4.2}$$

where v_{ref} represents normal walking speeds, $1.0 - 1.5$ m/s.

While the radial component is effective in slowing agents down when approaching other agents, the second component improves the ability of the agents to move around obstacles. This is achieved by a force, which we will refer to as the **deflection force**, that is perpendicular to the

relative velocity. In formulating the deflection force, we first need to define the scalar

$$\Omega_v(\hat{\boldsymbol{r}}_{ab}, \boldsymbol{v}_{ab}) \equiv \Omega_{v,ab} = (\boldsymbol{v}_{ab} \times \hat{\boldsymbol{r}}_{ab}) \cdot \hat{\boldsymbol{z}}, \tag{4.3}$$

where $\hat{\boldsymbol{z}}$ is the unity vector in the direction out of the computational plane. The sign of $\Omega_{v,ab}$ indicates which way around an obstacle is more natural for an agent to move. If $|\Omega_{v,ab}| > \epsilon_v$, where ϵ_v is a small constant e.g. 0.01, we can define $\Sigma_{v,ab}$ as

$$\Sigma_{v,ab} = \Omega_{v,ab}/|\Omega_{v,ab}|. \tag{4.4}$$

If not, $\Sigma_{v,ab}$ is set equal to 1 or -1 based on either agent preferences (agents preferring to move either to the right or to the left) or based on random choice. Next, we need to determine to what extent the two agents are on collision course. This is done by the function

$$\Pi_v(v_{ab,r}, v_{ab}) \equiv \Pi_{v,ab} = \begin{cases} \frac{v_{ab,r}}{v_{ab}} & \text{if } v_{ab} > \epsilon_v; \\ \frac{v_{ab,r}}{\epsilon_v} & \text{otherwise.} \end{cases} \tag{4.5}$$

In crowds where the density is small or medium, agents are likely to navigate around neighbouring agents as if they were isolated obstacles. And since the inter-agent separation decreases with increasing density, the deflection force must increase with increasing density to prevent collisions with other agents. For larger crowd densities, deflective motion around individual neighbours becomes less effective. In this regime, increasing the deflection force further will contribute to increased flow in the crowd. Based on this argument, we propose a density-dependent ehancement of the deflection force, D_{avoid}, which we simply formulate as

$$D_{\text{avoid}}(\rho) = 1 + e_{\text{avoid}} \frac{\rho}{\rho + \rho_{\text{avoid}}}, \tag{4.6}$$

where e_{avoid} and ρ_{avoid} are constants that need to be determined.

Finally, we can formulate the full obstacle avoidance force on agent a from agent b as

$$\boldsymbol{S}^{\mathcal{A}}_{1,ab} = -m_{ab}\Phi(r_{ab}/b_{A,ab}, 0)\left\{ A^r_{\text{avoid}} \Upsilon_{ab} \hat{\boldsymbol{r}}_{ab} + A^d_{\text{avoid}} D_{\text{avoid}}(\rho_{ab}) \Sigma_{v,ab} \Pi_{v,ab} \frac{\boldsymbol{v}_{ab} \times \hat{\boldsymbol{z}}}{v_{\text{ref}}} \right\}, \tag{4.7}$$

where $z_{ab} = r_{ab}/b_{A,ab}$ is normalized distance, $b_{A,ab} = (b_{A,a} + b_{A,b})/2$ is the mean avoidance scale length, and A^r_{avoid} and A^d_{avoid} are yet to be determined force constants.

4.1.2 Crowd repulsion

In contrast to obstacle avoidance, crowd repulsion only consists of a radial component. Compared with the radial component of the avoidance interaction, the velocity dependent factor Υ_{ab} is replaced by a angular dependent factor Θ_{ab} defined as

$$\Theta_{ab} = \theta_0 + (1 - \theta_0)\frac{1 + \hat{\boldsymbol{v}}_a \cdot \hat{\boldsymbol{r}}_{ab}}{2}, \tag{4.8}$$

where the parameter $0 \leq \theta_0 \leq 1$ determines the level of anisotropy in the crowd repulsion. The actual value of θ_0 is yet to be determined, but generally, one can say that a smaller θ_0 will

result in increased anisotropy which in turn means reduced flow speed in a uniform crowd. On the other hand, $\theta_0 = 1$, will result in a completely isotropic force and therefore zero net crowd repulsion in a uniform crowd. The crowd repulsion force on agent a from agent b is

$$\boldsymbol{S}^{\mathcal{A}}_{2,ab} = -m_{ab} A_{\text{crowd}} \Phi(r_{ab}/b_{C,ab}, 1) \Theta_{ab} \hat{\boldsymbol{r}}_{ab}, \tag{4.9}$$

where A_{crowd} is the crowd repulsion force amplitude.

4.2 Contact force

The contact force is very similar to the classic model by Helbing, Farkas & Vicsek (2000). The force between two agents during physical contact is split up into a radial component; only dependent on the separation, and a transversal component; dependent on both the separation and the transversal velocity difference. The full contact force exerted on agent a by agent b is

$$\boldsymbol{C}^{\mathcal{A}}_{ab} = (2m_b - m_a)[\kappa_r \hat{\boldsymbol{r}}_{ab} + \kappa_t (\boldsymbol{v}_{ab} \cdot \hat{\boldsymbol{t}}_{ab}) \hat{\boldsymbol{t}}_{ab}] \Delta(r_{ab} - d_{ab}), \tag{4.10}$$

where

$$\Delta(x) = \begin{cases} x & \text{if } x < 0; \\ 0 & \text{otherwise} \end{cases} \tag{4.11}$$

and d_{ab} is the mean agent diameter. Note that the mean mass, m_{ab}, has been replaced by the asymmetric expression $2m_b - m_a$. This is done to ensure that the more massive agent is favoured in a situation with direct contact. This is important in order to reduce the probability of mutual blocking (see section 7.3). In the original model, $\kappa_r = 1.6 \cdot 10^3 \text{s}^{-2}$ and $\kappa_t = 3.2 \cdot 10^3 (\text{ms})^{-1}$ (for 75 kg agents). Since our agents are assumed to have a circular (and not elliptical) shape, and because we assume the agents wear clothes that add a certain level of compressibility, we choose $\kappa_r = 5.0 \cdot 10^2 \text{s}^{-2}$ and $\kappa_t = 2.5 \cdot 10^3 (\text{ms})^{-1}$. This corresponds to a radial force of around 0.5g per centimetre compression. If we neglect the effect of the social force, we can estimate the total compression experienced by each of the two agents to be around 2.2 cm times the velocity difference (in m/s) at first contact. Even with a velocity difference of 2 m/s at first contact, the compression will not exceed the 20% injury limit found experimentally (Viano & King, 2000). For more robust handling of physical contact forces, the spring force should increase when the compression increases above a certain limit.

5 Solid boundary interaction

Complex geometrical structures in two dimensions can be constructed by combining points, straight lines, and curves with constant curvature, and in the model, we have chosen to build solid boundaries by combining one or more instances of these basic structures. We will refer to the basic structures used in a given model as **boundary segments**. The boundary prevents an agent from being influenced by anything located on the other side of the boundary. In other words, an agent a does not interact with a neighbouring agent b if the two are separated by a boundary segment. Boundaries can thus effectively limit the interaction region of nearby agents.

If boundary related corrections were not introduced, agents located near boundaries would therefore experience both an artificial drop in the crowd density as well as an imbalance in the crowd forces.

To achieve a realistic crowd behaviour near boundaries, the current crowd model incorporates three boundary related correction mechanisms. First, the density is corrected when boundaries come within the interaction range to compensate for the reduction in effective interaction area. Secondly, agents interact with individual boundary segments in order to balance the inter-agent forces and thereby to avoid collisions with the boundaries. It is particularly important when modelling dense crowds that the boundary forces match the inter-agent forces as closely as possible. Just as for the inter-agent force, the boundary force $\boldsymbol{\mathcal{F}}_{ab}^{\mathcal{B}}$ acting on agent a due to boundary segment b is separated into a social force (denoted $\boldsymbol{\mathcal{S}}_{ab}^{\mathcal{B}}$) and a contact force (denoted $\boldsymbol{\mathcal{C}}_{ab}^{\mathcal{B}}$). Finally, the preferred location and velocity is temporarily modified to take into account boundaries that prevent the agent from taking the direct route to the preferred location.

Sufficiently close to boundaries, the simulation area is separated into **boundary interaction sectors**, one on either side of each two-dimensional boundary segment b (lines or curves). Every sector is restricted by the associated boundary segment and straight lines, called **sector lines**, starting at the corresponding end points. Just as a boundary segment will have exactly two end points, does it also have two interaction sectors and two sector lines per end point (so four in all). If an end point is not shared with any other boundary segment, then the two associated sector lines are identical and parallel to the boundary tangent (directed away from the segment midpoint). If exactly two boundary segments share the same end point, the two associated sector lines are given by the bisector of the two angles formed by the two connected segments. The two sector lines are in this case parallel but opposite and the sum of the two angles is 2π. Fig. A.2 shows an example where to boundary segments, marked A and B, share an end point, marked V_1. The dashed red line through V_1 marks the exterior and interior (relative to the segment normal vector) sector lines. If more than two boundary segments share an end point p, then the two sector lines associated with boundary segment b at point p is equal to the bisector to the angles between b and the closest boundary segments on either side of b. Fig. A.3 shows an example where 3 segments, marked A, B, and C, share the end point V_1. Again, sector lines are indicated by dashed coloured lines. The red sector line is shared by segments A and B, the green line is shared by segments A and C, while the blue line is shared by segments B and C.

The interaction between an agent a and a boundary segment b can be described as an approximation to the interaction between a and imaginary agents outside b (as viewed by a). For now, let us define the *inside* and *outside* of segment b such that agent a is located on the inside of b. The imaginary agents are then assumed to fill the *outer* interaction sector so that agent a is separated from the imaginary agents by segment b. The imaginary agents are assumed to be uniformly distributed in the outer interaction sector with an agent separation which is consistent with the density of agent a. Just as in the inter-agent case, the social boundary forces depend

on a spatial separation vector. In the current context, this vector is defined as the vector from agent a to its mirror image with respect to b. If the separation vector intersects the boundary segment, we refer to the intersection as the **boundary interaction point**. In this case, the separation vector will be normal to the boundary segment (if a line or curve segment). In the event that the separation vector does not intersect the boundary segment, the separation vector is defined by mirroring the agent about the nearest boundary segment end point.

Before we can discuss the social boundary forces in more detail, we need to look at the boundary interaction scale lengths and how the calculated density is corrected near boundary segments. Then, the contact boundary force is briefly discussed.

5.1 Boundary interaction scale length

The interaction scale lengths of boundary interaction should be comparable to the corresponding scale lengths of inter-agent interaction. This means that the scale lengths should be large when the crowd density is close to zero and decrease as the density increases. Fig. 5.1 depicts a uniform crowd below a boundary segment defined by the points p_1 and p_2. It shows the distribution of agents (circles with black filling) and the corresponding imaginary mirror agents (circles with grey filling). In this case, one has made the simplifying assumption that the relevant sector lines are normal to boundary segment. It also shows the crowd repulsion interaction range and the projected position onto the boundary of agent a.

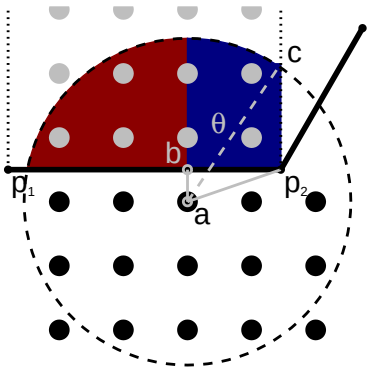

Figure 5.1 A uniform crowd (black dots) and the corresponding mirror agents (grey dots) located below and above, respectively, of a boundary defined by the points p_1 and p_2. The dashed circle indicates the wall repulsion interaction range. See main text for further details.

The boundary forces should match the inter-agent forces, and this is particularly important when it comes to wall repulsion which should balance crowd repulsion, the dominant force in

dense crowds with small relative velocities. The obvious choice would therefore be to let the boundary scale lengths be equal to the inter-agent scale lengths, as given by Eqs. 2.12 and 2.16. So, we choose the wall repulsion interaction scale length for the interaction between agent a and boundary segment b, $b_{C,ab}$ to be equal to $b_{C,a}$, the crowd repulsion scale length of agent a. In the case of obstacle avoidance, on the other hand, we need to make sure that we get an efficient agent interaction with isolated, static obstacles. In order to achieve this, it is important that the interaction scale length is sufficient large.

Fig. 2.3 showed that even a very modest crowd density of 0.01 m^{-2} will cause the avoidance scale length to be reduced by more than a factor of 2 relative to its maximum value. At the same time, boundary tests have revealed that a rapid decrease in the boundary scale length can cause agents to make unrealistically sudden movements near boundaries. To avoid this model deficiency, the scale lengths should have a relatively low dependence on density when the density is much smaller than the reference density. For higher levels of density, the obstacle avoidance boundary scale length should approach the corresponding inter-agent scale length. To achieve this, we first define the density weight factor for agent a, ς_a, as

$$\varsigma_a = \frac{\rho_a}{\rho_a + \rho_{\text{ref}}}. \tag{5.1}$$

The obstacle avoidance scale length for the interaction between agent a and boundary segment b, $b_{A,ab}$ can then be formulated as a weighted sum of the avoidance scale length of agent a and the maximum avoidance scale length:

$$b_{A,ab} = \varsigma_a b_{A,a} + (1 - \varsigma_a) b_{A,0}. \tag{5.2}$$

With ρ_{ref} and $b_{A,0}$ as defined in section 2.5.1, the boundary avoidance scale length becomes roughly 95% of its maximum value when the crowd density is equal to 0.01 m^{-2}.

5.2 Density correction

Crowd density is computed as a weighted sum over neighbouring agents within a circular interaction region (see Eq. 2.4). Because nearby boundaries can represent a truncation of this interaction region, an artificial drop in density would typically be observed if the estimated density is not properly corrected. Referring to the example shown in Fig. 5.1, only agents found below the line from p_1 to p_2 are included when calculating the density of e.g. agent a. It is not practical to include the contribution from the imaginary mirror particles indicated above the $p_1 - p_2$ line. As a result, the computed density will not be consistent with the typical agent separation. Therefore, we want to correct the computed density by renormalizing the weight function, $\mathcal{W}_{ab}$, defined in Eq. 2.5. First, we approximate $\mathcal{W}_{ab}$ by a step function where all agents within interaction range is given the same weight. The effective interaction range with this simplified weight function is $R_{\rho,a} = \kappa_\rho h_a$, where

$$\kappa_\rho = \frac{1}{\sqrt{\pi h^2 \mathcal{W}(0,h)}} = \frac{2}{\sqrt{7}}. \tag{5.3}$$

Using this simplified weight function, and assuming a continuous rather than a discrete agent distribution, we can estimate the reduction in calculated density for agent a when we know the fractional reduction in the associated interaction area due to nearby boundaries.

Another simplification we will make when deriving the density correction is related to how we treat information regarding the coupling of boundary segments. To accurately calculate the fractional reduction in the interaction area of agent a we would need information not only on the location of individual boundary segments, but also on how these boundary segments are connected (as seen in Fig. 5.1). This could lead to quite time-consuming computations which, in the current context, is not strictly necessary in order to obtain adequate accuracy. To simplify the problem, we try to calculate the reduction in interaction area due to each nearby boundary segment separately without considering how segments are connected. Referring to the discussion in section 5 regarding sectors and sector lines, this means not calculating the exact interaction sectors. What we do need to take into account, is the possibility that one boundary segment might be partially hidden behind other boundary segments. Therefore, before accepting the interaction area reduction caused by a boundary segment b, a test is performed to check if b is visible to agent a or hidden behind other, closer boundaries. Now, we are ready to describe the density correcting algorithm in more detail.

Let us first assume that boundary segment b is a straight line, for instance as shown in Fig. 5.1. If an agent a is within interaction range R_a of an infinite straight line, the circle with radius R_a and the line will have exactly two intersections. Since the boundary segment b is of finite length, we have to consider the possibility that b has only one or even no intersection with the interaction circle of a, even though b is within interaction range of a. That part of boundary segment b which is inside the interaction region of a will be referred to as the boundary segment b *inside* agent a. We will denote the end points of the segment of b inside a by c_1 and c_2 and the distance between these two points by l_{ab}. In order for boundary segment b to be relevant in this context, the midpoint between c_1 and c_2 must be visible to agent a (and not hidden behind other boundary segments). Assuming this is the case, we can calculate the reduction in the interaction area of a by b, δA_a^b, as follows: Let the distance from agent a to boundary segment b be given as s_{ab}, and the angle between the two vectors from the position of a to the end points c_1 and c_2 be referred to as χ_{ab}. Then, δA_a^b can then be estimated as

$$\delta A_a^b = \frac{1}{2}(\chi_{ab} R_a^2 - s_{ab} l_{ab}). \tag{5.4}$$

If boundary segment b is a curve with radius R_b, the reduction in the interaction area of a due to b can be calculated in a similar fashion. Once again, c_1 and c_2 denote the end points of b *inside* a, and the distance between c_1 and c_2 is given by l_{ab}. As before, s_{ab} is the distance from the agent to the straight line between c_1 and c_2, and χ_{ab} is the angle between the two vectors from the position of a to c_1 and c_2, respectively. In addition, we need to calculate s_{cb}, the distance from the curve origin to the straight line between c_1 and c_2, and χ_{ab}, the angle between the two vectors from the curve origin to c_1 and c_2, respectively. With these additional

parameters, we find the estimated reduction in the interaction area of a due to the curved boundary segment b, δA_a^b, to be given as

$$\delta A_a^b = \frac{1}{2}[\chi_{ab} R_a^2 \pm \chi_{cb} R_b^2 - (s_{ab} - s_{cb}) l_{ab}], \tag{5.5}$$

where the correct sign to use for the second term is found as follows: A closed region S_{ab} is defined by the curve b and the straight lines from the end points of b and the position of agent a. If S_{ab} is convex, then the second term in Eq. 5.5 should be positive. Alternatively, if S_{ab} is concave (non-convex), then the second term in Eq. 5.5 should be negative.

The normalized reduction in the interaction area of agent a due to all visible boundary segments within interaction range, δY_a, is estimated by adding the reduction found for each boundary segment and divide by the full interaction area for the simplified weight function

$$\delta Y_a = \frac{\sum_b \delta A_a^b}{\pi R_{\rho,a}^2}. \tag{5.6}$$

If accurately calculated, $\delta Y_a < 1$ and the density correction of agent a, $C_{\rho,a}$ should then be given as

$$C_{\rho,a} = \frac{1}{1 - \delta Y_a}. \tag{5.7}$$

However, we have to take into account that δA_a^b was estimated without properly taking into account the connection between different boundary segments. For this reason, δY_a could in special cases become larger than unity. If this is the case, Eq. 5.7 could cause $C_{\rho,a}$ to become infinite and possibly negative. To get a more robust algorithm, we first ensure that $\delta Y_a \leq 1$. Then, to avoid an infintely large density correction, we calculate the correction factor by this modified expression:

$$C_{\rho,a} = \frac{1}{1 - \delta Y_a + \epsilon_Y \delta Y_a^2}, \tag{5.8}$$

where ϵ_Y typically would be around 0.1. This would ensure that $C_{\rho,a} \leq 10$.

5.3 Social boundary force

Just as agents have a tendency of maintaining a reasonable distance to neighbouring agents if possible, so will agents also try to keep away from solid boundaries. The term "social boundary force" refers to boundary-agent forces which act on a distance and are analogous to the social inter-agent forces described in section 4.1. As in the inter-agent case, the social forces are sorted into boundary avoidance and wall repulsion. The social force on agent a from boundary segment b is therefore written as

$$\boldsymbol{S}_{ab}^{\mathcal{B}} = \boldsymbol{S}_{1,ab}^{\mathcal{B}} + \boldsymbol{S}_{2,ab}^{\mathcal{B}}, \tag{5.9}$$

where the indices 1 and 2 refer to obstacle avoidance and wall repulsion, respectively. The corresponding interaction scale lengths for the two types of interactions are given by Eqs. 5.2 and 2.16, respectively.

5.3.1 Boundary avoidance interaction

The boundary avoidance interaction is a relatively short-range force, and we can therefore safely assume that an agent a in this case only interacts with at most one mirror agent per boundary segment b. This means that the interaction with the mirror agent population can easily be approximated by a single interaction with b. The only requirement for such an interaction, is that b is inside the interaction range of a and that the separation vector between a and b is not intersected by other boundary segments.

The obstacle avoidance formulation presented in Eq. 4.7 for the inter-agent case, is the starting point for the formulation used in the case of boundary interaction. There are however a few modifications introduced: The deflection force, represented by the second term of Eq. 4.7, describes the ability of the agent to navigate around relatively small obstacles. Solid boundaries, such as walls, are normally quite large in comparison and not easily navigated around. The deflection force is therefore not applicable in this case and should not be included. In order to maintain a good balance between inter-agent forces and boundary forces, it is reasonable to compensate for this omission by increasing the radial component of the boundary avoidance force. We also want the boundary avoidance interaction to increase with increasing crowd density and to be much smaller when an agent is not heading directly towards a boundary. With these modifications, the boundary obstacle avoidance force on agent a from boundary segment b can be formulated as

$$\boldsymbol{S}^{\mathcal{B}}_{1,ab} = -m_a \Phi(r_{ab}/b_{A,ab}, 0) C_{\mathcal{B}} A^r_{\text{avoid}} \Upsilon^{q_{\mathcal{B}}}_{ab} \left(\frac{\rho + \rho_{\text{ref}}}{\rho_{\text{ref}}} \right)^{p_{\mathcal{B}}} \hat{\boldsymbol{r}}_{ab}, \tag{5.10}$$

where Υ_{ab} is defined by Eq. 4.2, ρ_{ref} is the same reference density used in section 2.5.1, $z_{ab} = r_{ab}/b_{A,ab}$ is normalized separation distance, $b_{A,ab}$ is the boundary avoidance scale length, A^r_{avoid} is the force constant introduced in section 4.1.1. The free parameters $C_{\mathcal{B}} > 1$, $q_{\mathcal{B}} > 1$, and $p_{\mathcal{B}} > 1$ are the yet to be determined through calibration tests.

5.3.2 Wall repulsion interaction

Wall repulsion, which is the boundary force equivalent to crowd repulsion, has a longer interaction range in medium and high density crowds than the boundary avoidance force. As a consequence, the single interaction point approximation is not sufficiently accurate in describing this type of boundary interaction. An exception to this rule is if the boundary segment is a point. Then, the formulation from the inter-agent model, given in Eq. 4.9, can be applied directly to the agent-mirror agent interaction. If on the other hand, the boundary segment is a line or a curve, the wall repulsion acting on agent a from boundary segment b should ideally equal the total crowd repulsion force on a from all mirror agents which fit inside the appropriate interaction sector associated with b. In Appendix A we try to estimate the wall repulsion on a by calculating the effect of the mirror agent distribution. This can be done by integrating the wall repulsion force over the appropriate interaction sector. In Fig. 5.1, the red and blue coloured regions indicate that part of the interaction sector of the boundary segment from p_1 to p_2 which is inside the interaction range of agent a. Note that in this case, we have simplified the problem

by assuming the sector lines (indicated by dotted lines) are normal to the boundary segment. This assumption is used in the first approximation to the wall repulsion, discussed in section A.1.

We also assume that the wall repulsion, just as the boundary avoidance force, is normal to boundary segment b. In addition, wall repulsion will be proportional to the crowd density of agent a, ρ_a. If $z_{ab} = r_{ab}/b_{C,a}$ is the normalized distance from agent a to the mirror image of a about the boundary segment b, the contribution to the wall repulsion force on agent a from boundary segment b can be written as

$$\boldsymbol{S}^{\mathcal{B}}_{2,ab} = -m_a A_{\text{crowd}} \Theta_{ab} \rho_a b^2_{C,a} I^{\text{wall}}_{ab}(z_{ab}) \hat{\boldsymbol{r}}_{ab}, \tag{5.11}$$

where Θ_{ab} is defined by Eq. 4.8 and $I^{\text{wall}}_{ab}(z_{ab})$, derived in Appendix A, is given by Eq. A.28.

It remains to be seen how accurate the new model of wall repulsion is. As a simple test, we want to calculate the wall repulsion on an agent a for the cases of two different, straight boundaries. The first boundary is sufficiently large so that the end points are located outside the range of the agent-boundary interaction. The second boundary, on the other hand, has a total length which is identical to the interaction radius. This means that the boundary end points will be inside the interaction range if the agent is sufficiently close to the boundary. We assume a uniform crowd density. Agent a is placed on the boundary symmetry line, but the distance from the boundary vary. First, we calculate the boundary force by explicitly generating mirror agents on the outside of the boundary and directly calculating the total inter-agent crowd repulsion force on agent a from all the mirror agents. This is the reference result. Then, we calculated the wall repulsion force using Eq. 5.11. In Fig. 5.2 we compare the calculated force for the two boundaries in question as a function of normalized agent-boundary separation. The solid lines refer to the direct interaction with mirror agents, while the dashed lines are made from using the approximation given by Eq. 5.11. The colours indicate the crowd density, in the range $1 - 6$ m^{-2}. The dotted curve in both panels shows the wall repulsion if the boundary segment is a point and the wall repulsion therefore is modelled as a single interaction between the agent in question and its corresponding mirror agent.

Both panels of Fig. 5.2 reveal a good match between the wall force calculated by direct summation and using the integral approximation. As expected, the dashed curves representing the integral approximation show none of the smaller scale variations found in the solid curves representing summation over discrete mirror agents. We also note that the integral approximation slightly overestimates the force at larger distances, in particular when the density is moderate. This is reasonable since the mirror agent spacing is quite large relative to the interaction scale length, ranging from about $5b_C$ at $\rho = 1$ to about $4b_C$ at $\rho = 6$.

To illustrate the effect of introducing both the density correction described in section 5.2 and the wall repulsion force described here, we have constructed two examples which involve a static crowd in a complex, closed boundary. The agents are spread out evenly and the average density of the crowd is 2 agents per square meter. The only forces included are the crowd

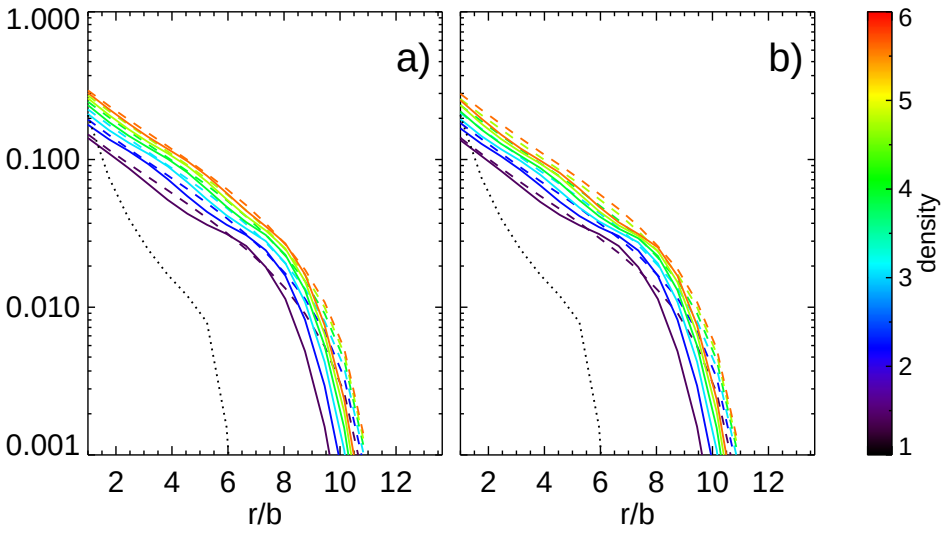

Figure 5.2 Normalized wall repulsion force as a function of normalized distance from a boundary calculated using mirror agents (solid lines) and the new wall repulsion approximation (dashed lines). The colour indicates the crowd density. Panel **a** *corresponds to a straight boundary where the size is larger than the interaction diameter, whereas panel* **b** *shows the case where the length of the boundary is equal to the interaction radius. The dotted line indicates the force in the case of a boundary point.*

repulsion and wall repulsion forces. In the first example, the boundary is built using only line segments. In Fig. 5.3, the boundary is indicated by the solid, black lines. It can be seen that the boundary exhibits both convex and concave angles, in addition to line segments that are only connected to other segments at one of the two end points. Each agent in the crowd is represented by a filled circle with an outer ring. The colour of the circle indicates the norm of the total force, while the colour of the ring corresponds to the estimated crowd density, ρ. For agents with a sufficiently large force strength, a red arrow starting at the agent's position indicates the direction of the total force.

Sufficiently far from the boundary, we see that the description is satisfactory. However, the uncorrected crowd density is seen to drop for agents located nearer to the boundary. As expected, the estimated density is at its lowest where the interior angle is at its smallest. For instance, the density drops to about 1.2 near corners where 3 lines intersect. Coinciding with the drop in estimated density, is the force imbalance. The force is always pointing towards the boundary and the force strength can reach 10-20% of the gravitational force. This is comparable to what is a reasonable upper limit to forces acting on agents during movement. Therefore, it represents an unacceptably high level of noise in a static or semi-static crowd. Fig. 5.4 shows the corresponding results when the density correction and wall repulsion are used. First, we see that the density near the boundary never drops below 1.7-1.8. Secondly, the force strength is less than 1% of the gravitational force and therefore negligible for most agents. A few agents, such as

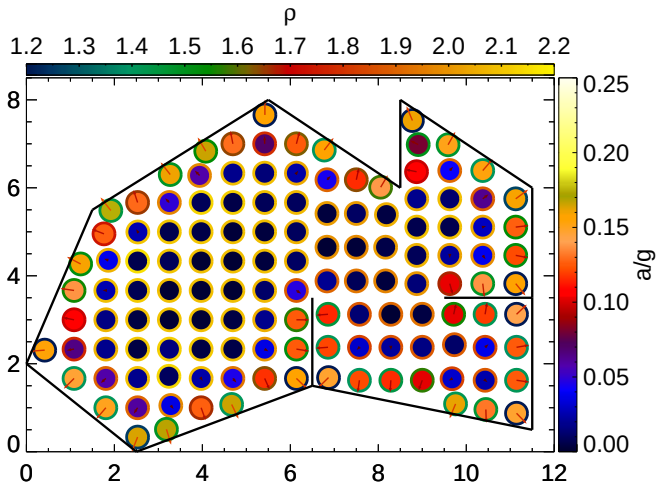

Figure 5.3 *Snapshot of a static crowd inside a closed boundary of line segments when no specific boundary handling is applied. The colour of the filled circles and outer rings indicate the acceleration norm and the calculated desnity, respectively. Red arrows show the direction of the acceleration vector.*

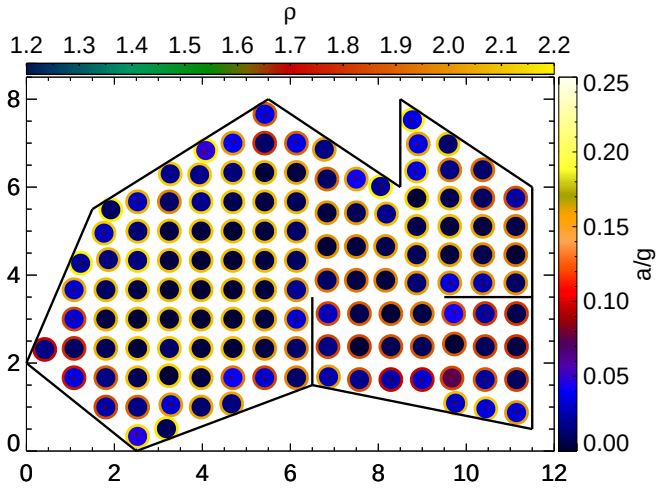

Figure 5.4 *Snapshot of a static crowd inside a closed boundary of line segments when density correction and wall repulsion are applied. The colour of the filled circles and outer rings indicate the acceleration norm and the calculated desnity, respectively. Red arrows show the direction of the acceleration vector.*

the agent located roughly at $x = 9.7$ and $y = 1.7$, still show a noticeable force imbalance but this is due to a slightly inhomogeneous crowd distribution rather than errors in the boundary treatment.

As an additional test, we modify the boundary used in the previous two tests. This time we introduce curved segments at two places in the upper part of the boundary. The right-most curve has positive curvature, while the left-most curve has negative curvature. Despite the change in the shape of the two boundary segments, Fig. 5.5 shows little change in the boundary related errors when no boundary corrections are applied. Fig. 5.6 shows the corresponding results when estimated density is corrected and wall repulsion is included. Again, we see that the boundary corrections remove much of the variation in density and the force imbalance. We also see that the level of errors near the curved boundary segments is roughly the same as the corresponding error level near any of the line boundary segments.

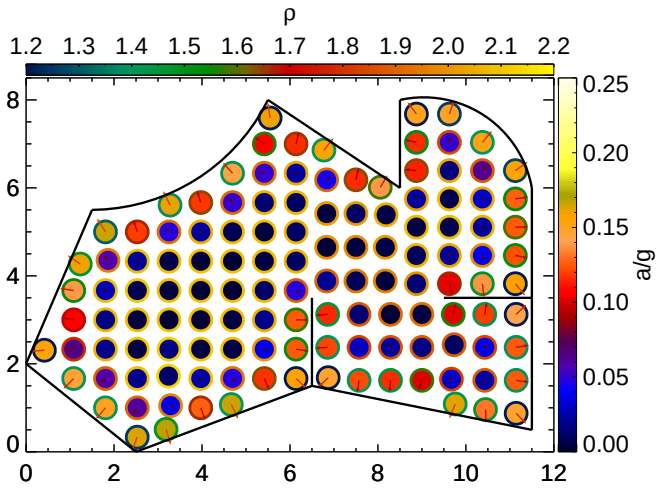

Figure 5.5 *Snapshot of a static crowd inside a closed boundary of both line and curve segments when no specific boundary handling is applied. The colour of the filled circles and outer rings indicate the acceleration norm and the calculated desnity, respectively. Red arrows show the direction of the acceleration vector.*

5.4 Contact boundary force

Contact boundary forces are treated completely analogous to the inter-agent contact forces. Again, the separation vector is defined as the vector from the agent in question and its mirror image with respect to the boundary segment. The mirror agent is assume to have the same physical properties as the parent agent, and the velocity vector of the mirror agent is a mirror image of the velocity of the parent agent with respect to the boundary. With these boundary properties, the contact boundary force between a boundary element b and an agent a will take the form given in Eq. 4.10.

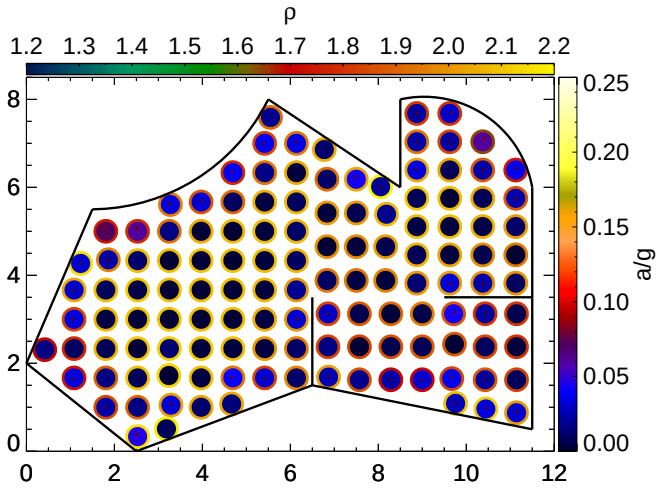

Figure 5.6 Snapshot of a static crowd inside a closed boundary of both line and curve segments when density correction and wall repulsion are applied. The colour of the filled circles and outer rings indicate the acceleration norm and the calculated desnity, respectively. Red arrows show the direction of the acceleration vector.

5.5 Automatic path finder

We want agent a to automatically consider solid boundaries when trying to reach the preferred location $\boldsymbol{z}_a$. If a boundary obstructs the direct path to $\boldsymbol{z}_a$, then the agent should choose a preferred velocity which would correspond to moving around the boundary. Since a boundary typically has a substantial size relative to the size of a single agent, a simple deflection force (see section 4.1.1) will not be sufficient. Instead, we introduce an algorithm which allows the preferred velocity to be modified by nearby boundaries. The automatic path finder considers both boundary segments and individual vertices. The algorithm used is described in detail in Appendix B.

6 Model calibration

In formulating the basic crowd model, we have introduced a number of free parameters that influence the behaviour of the model. Some of these parameters were determined already in section 2 based on fundamental observations and assumptions regarding the human body and human motion. Still, there are other parameters, such as the force amplitudes A^v_{will}, A_{crowd}, A^r_{avoid}, and A^d_{avoid}, that need to be determined before applying the model to more complex test problems. This model calibration is achieved by using the model to solve simplified problems and comparing the results to observational data. Starting with the most fundamental parameters and gradually extending the model to more complec problems, we can determine the remaining parameters, one at the time. In this section, we describe the calibration of the current crowd model

6.1 Uni-directional, homogeneous flow ($A_{\text{crowd}}/A^v_{\text{will}}$ and θ_0)

The fundamental diagram for pedestrian motion is a cornerstone in pedestrian traffic planning. It describes the empirical relation between crowd density ρ and the flow speed v (or eqivalently the specific flow rate J). Despite the fact that there is a fairly large spread in the empirical data (Fruin, 1971; Helbing, Johansson & Al-Abideen, 2007; Older, 1968; Predtechenskii & Milinskii, 1978; Still, 2000; Weidmann, 1992), the fundamental diagram is widely used as a quantitative benchmark for crowd models (Daamen et al., 2002; Parisi et al., 2009; Seyfried et al., 2006). In the current work, we start by looking at steady-state, uni-directional flow in a homogeneous and infinitely large crowd where the agents are placed in a rectangular grid formation. We neglect contact force which should reduce the flow speed further when the agent spacing becomes smaller than the agent diameter at $\rho \sim 5$. Initially, we also assume the flow will force to be linear, that is $\Gamma(x)$ in Eq. 3.8 is identical to x for all x. Later, we will look at the effect of having a non-linear will force.

As a result of these assumptions, the crowd model can be reduced to a semi-analytic calculation where the only free parameters are the force amplitude ratio, $A_{\text{crowd}}/A^v_{\text{will}}$, and the level of isotropy, θ_0. The former parameter scales the strength of each individual crowd repulsion interaction relative to the flow will force. The latter parameter determines the level of the net crowd force in a uniform crowd. The two parameters are linked and must therefore be considered together. The original social force model of Helbing is typical used with parameters that correspond to $A_{\text{crowd}}/A^v_{\text{will}} \sim 10$ and $\theta_0 \sim 0.3 - 0.8$ (Vetter et al., 2011). In the current model, the range of the social force is larger. It is therefore reasonable that a slightly smaller value of $A_{\text{crowd}}/A^v_{\text{will}}$ is appropriate in this case.

6.1.1 Results with a linear will force

Fig. 6.1 shows the results of the analysis for $A_{\text{crowd}}/A^v_{\text{will}} = 6$ and a preferred velocity of 1.4 m/s. The left- and right-hand panel show the flow speed (v) and flow rate (J), respectively, as a function of crowd density (ρ). The red, green, olive, bright blue, and dark blue curves correspond to $\theta_0 = 0.1, 0.2, 0.3, 0.4,$ and 0.5, respectively. For comparison, we have included data from two empirical studies. The dashed curves represent the Weidmann model constructed on the basis of numerous data sets, many of which are multi-directional rather than uni-directional (Weidmann, 1992). According to this model, the flow speed is given as

$$v = u\left(1 - \exp\left[-\gamma_W\left(\frac{1}{\rho} - \frac{1}{\rho_{\text{max}}}\right)\right]\right), \tag{6.1}$$

where $u = 1.34$ m/s, $\rho_{\text{max}} = 5.4$ agents/m^2, and $\gamma_W = 1.913$ agents/m^2. The open circles in Fig. 6.1 are taken from an empirical study of pedestrian flow across the Jamarat Bridge in Makkah (Helbing, Johansson & Al-Abideen, 2007). Although the empirical data agree qualitatively, there is substantial difference quantitatively. This could partly be because the Weidmann model also relies on data from multi-directional flow. Also, social and physical characteristics of the crowds are factors that are likely to play a role.

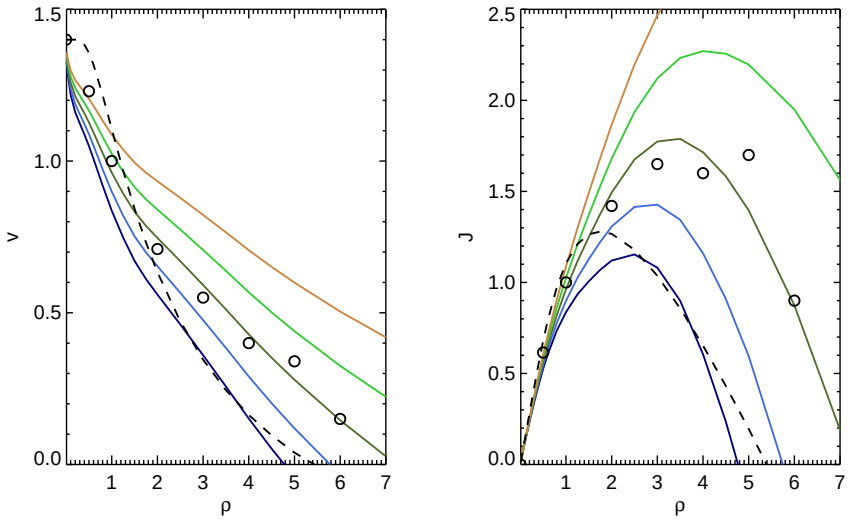

Figure 6.1 Fundamental diagrams for uni-directional pedestrian flow. The left- and right-hand panels show the flow speed (v) and flow rate (J), respectively, as a function of crowd density (ρ). The semi-analytical results with linear will force for $A_{crowd}/A^v_{will} = 6$ and θ_0 ranging from 0.1 (red) to 0.5 (dark blue) are compared to the Weidmann model (Weidmann, 1992) (dashed line) and empirical data from Helbing, Johansson & Al-Abideen (2007) (open circles).

First, we notice that the flow speed drops too quickly for small, but non-zero density levels. This regime will be addressed by the non-linear will force amplifier. For larger densities, the solid lines show that the new crowd model with $A_{\text{crowd}}/A^v_{\text{will}} = 6$ fits reasonably well to the empirical data. The model fits nicely with the Jamarat Bridge data if $\theta_0 = 0.3$ is chosen. If on the other hand $\theta_0 = 0.4 - 0.5$ is chosen, the resulting fundamental diagram fits well with the Weidmann model. If the ratio $A_{\text{crowd}}/A^v_{\text{will}}$ is increased, the isotropy parameter θ_0 must be decreased in order to maintain roughly the same curves in the fundamental diagram, and vice versa. In fact, the fundamental curves appear in this case to be defined by a single variable roughly equal to $A_{\text{crowd}}/A^v_{\text{will}} + 10\theta_0 = 9$. We choose $A_{\text{crowd}}/A^v_{\text{will}} = 6$ and $\theta_0 = 0.3$ as default values for the new crowd model.

6.1.2 Results with a non-linear will force

To achieve a better fit with the empirical data for $\rho < 1$, we want to use the non-linear will force as determined by the will force amplifier (see Eq. 3.8). The amplifier is characterized by the parameters x_0, x_1, x_2, and Γ_2. We need strong relative amplification for $\rho \ll 1$ so $x_0 \ll 1$, for instance $x_0 = 0.05$. The last two parameters, x_2 and Γ_2, is related to when and how strong the amplification is when the flow speed is relatively small, corresponding to relatively high density. These parameters cannot be properly determined without including contact forces. For now, we assume $x_2 = 0.9$ and $\Gamma_2 = 2$. We are left with determining x_1, for which we have $x_0 < x_1 < x_2$. In the following test, we consider x_1 in the range $0.2 - 0.5$. The results are

shown in Fig. 6.2 and once again compared to the Weidmann model (Weidmann, 1992) and the Jamarat Bridge data (Helbing, Johansson & Al-Abideen, 2007). It is clear that the non-linear

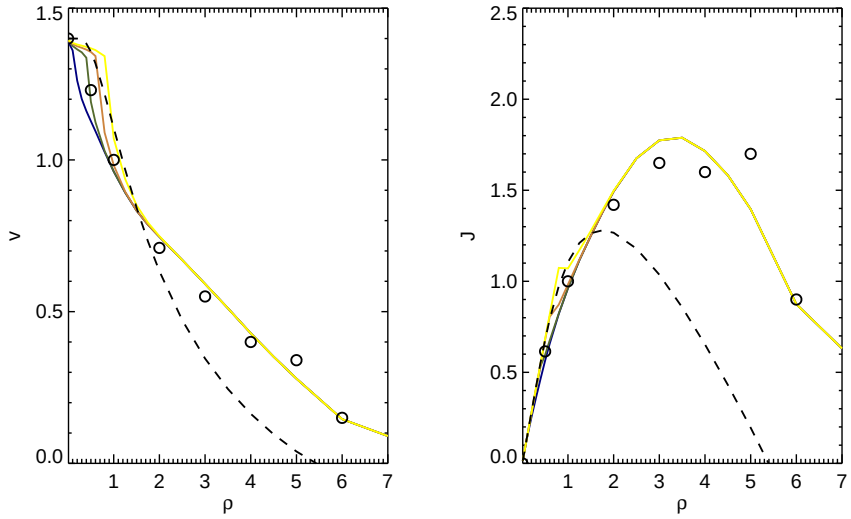

Figure 6.2 *Fundamental diagrams for uni-directional pedestrian flow. The left- and right-hand panels show the flow speed (v) and flow rate (J), respectively, as a function of crowd density (ρ). The semi-analytical results with a non-linear will force for $A_{crowd}/A^{v}_{will} = 6$, $\theta_0 = 0.3$, and x_1 ranging from 0.2 (blue) to 0.5 (yellow) are compared to the Weidmann model (Weidmann, 1992) (dashed line) and empirical data from Helbing, Johansson & Al-Abideen (2007) (open circles).*

amplfier gives a better fit to the empirical data in the low density regime. At larger densities, the effect is negligible. Compared to the Weidmann model, $x_1 = 0.4 - 0.5$, should be a suitable choice. Subsequent tests of multi-direction flow indicate that $x_1 = 0.5$ is close to the optimal value. Therefore, we choose $x_1 = 0.5$ as the default value.

6.2 Multi-directional, homogeneous flow ($A^{r}_{\text{avoid}}/A_{\text{crowd}}$)

It is still open for debate how the fundamental diagram for a multi-directional case should differ from the corresponding uni-directional case. However, Schadschneider et al. (2009) points to flow direction as possibly the most important factor in explaining differences in the fundamental diagram obtained with different experimental data. In support of this view, experimental data exist where a reduction in flow speed with increased direction imbalance has been observed (Navin & Wheeler, 1969). We will look at a multi-directional problem very similar to the uni-directional problem described in section 6.1. Agents are initially placed as in the uni-directional case, in a homogeneous, infinite crowd on a rectangular grid formation. A single lane of agents move at a constant speed, while all other agents are assumed to be static. Since the agents in the lane move relative to the agents in the surrounding crowd, the crowd is not strictly homogeneous with a time-independent state unless we average over a suitable time period. This is solved by averaging over a sufficiently large number of different configuration where the

position of agents in the lane is shifted relative to the position of the other agents. Note that this averaging will in itself cause a slight decrease in flow speed relative to that found in the uni-directional case.

Since this problem involves velocity differences between interacting agents, the obstacle avoidance force will be non-zero. However, symmetry causes the deflection force to be zero. The only parameter is therefore A^r_{avoid}, the radial component of the avoidance force. It is this parameter that determines the difference between the uni-directional case and the multi-directional case. Using the same semi-analytical approach used in section 6.1, we want to investigate exactly how large the reduction in flow speed is for a given value of A^r_{avoid}. In Fig. 6.3, we see the fundamental diagram in the multi-directional case for 5 different values of the ratio $A^r_{\text{avoid}}/A_{\text{crowd}}$, ranging from 0.0 (dark blue) to 0.4 (red).

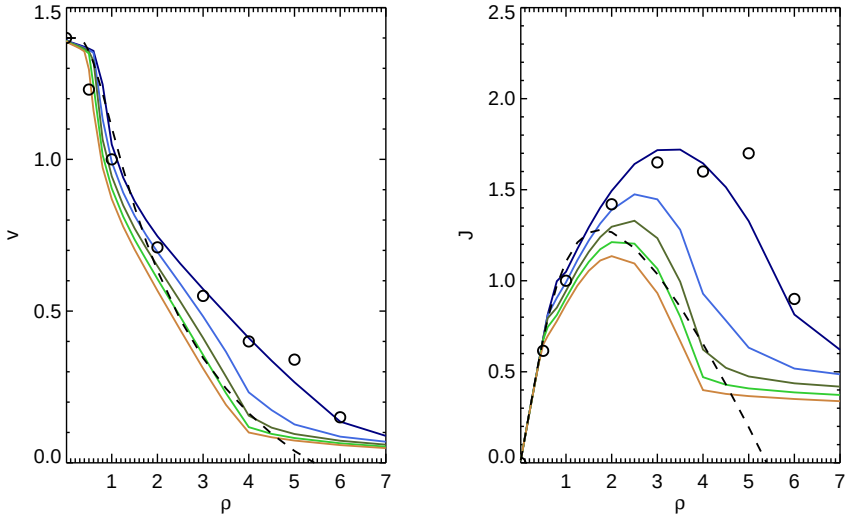

Figure 6.3 *Fundamental diagrams for pedestrian flow in a static background crowd. The left- and right-hand panels show the flow speed (v) and flow rate (J), respectively, as a function of crowd density (ρ). The semi-analytical results with a non-linear will force for $A_{crowd}/A^v_{will} = 6$, $\theta_0 = 0.3$, and A^r_{avoid}/A_{crowd} ranging from 0.0 (dark blue) to 0.4 (red) are compared to the Weidmann model (Weidmann, 1992) (dashed line) and empirical data from Helbing, Johansson & Al-Abideen (2007) (open circles).*

Let us assume that the Jamarat Bridge data (Helbing, Johansson & Al-Abideen, 2007) represents a more or less uni-directional case, and the Weidmann model represents a multi-directional case. If so, the ratio $A^r_{\text{avoid}}/A_{\text{crowd}}$ should be chosen so that the resulting fundamental diagram fits roughly with the Weidmann model. As before, the flattening of the fundamental curves in Fig. 6.3 for densities larger than roughly 4 agents$/\text{m}^2$ is caused by the non-linear will force and the fact that contact forces are not included in the semi-analytic model. Apart from this apparent flaw in the new model, we see that $A^r_{\text{avoid}}/A_{\text{crowd}} \approx 0.2$ gives a quite good fit with the Weidmann model. However, there are at least two factors to consider before concluding. First,

the semi-analytic analysis was based on a lane of agents moving in a static crowd. If we instead had considered a truly two-way flow, the relative velocity difference between agents of adjacent lanes would be twice the flow speed. According to Eq. 4.2, the radial avoidance force would then be upto a factor two larger (for relative velocities much smaller than the reference velocity). This would result in a smaller equilibrium flow speed relative to that shown in Fig. 6.3, in particular where the flow speed is much smaller than the reference velocity. The second factor to bear in mind, is that the Weidman model is constructed on the basis of data that also include uni-directional streams. This could imply that truly multi-directional streams should result in flow speeds that lie slightly below that of the Weidmann model. All in all, it would be reasonable to conclude that $A^r_{\text{avoid}}/A_{\text{crowd}}$ should be in the range 0.1 to 0.3. We will for now keep $A^r_{\text{avoid}}/A_{\text{crowd}} = 0.15$ as a default value.

6.3 Agent meeting ($A^d_{\text{avoid}}/A_{\text{crowd}}$)

In order to determine the appropriate level of the obstacle avoidance deflection force, we look at a simple system describing the close-up meeting of two agents. Since only two agents are involved, we assume that D_{avoid} (defined in Eq. 4.6) is roughly 1. First, we concentrate on the case where only one of the agents is moving. Afterwards, we look at the more realistic case where both agents are moving. In both cases, preferred locations are defined so that a nearly head-on collision between the two agents would occur if motion was governed by the flow will force alone. In the absence of a deflection force, the interaction between the two agents would be strictly radial. Although effective at slowing down moving agents, a radial force would in this case contribute very little to deflecting agents from a straight line. As a consequence, the two agents will either collide or, at best, make a sharp turn once the separation between the two agents have become sufficiently small. To achieve a much more realistic movement past the static agent, we need to include a non-zero deflection force.

6.3.1 Asymmetric meeting

In this test problem only one of the agents is moving. The static agent is located at origin. The moving agent starts at the position $\boldsymbol{r}_0 = (-30\text{ m}, -0.05\text{ m})$ with a preferred location at $\boldsymbol{r}_1 = (30\text{ m}, -0.05\text{ m})$. The distance between the static agent and the straight line between $\boldsymbol{r}_0$ and $\boldsymbol{r}_1$ is therefore only 5 cm, which corresponds to roughly 25% of the agent radius. However, with the inclusion of a non-zero deflection force, the moving agent will deviate from the straight line in such a way that the minimum separation between the two agents becomes larger than 5 cm. Fig. 6.4 shows how the minimum separation between the agents (δr_{min}) and the maximum acceleration (a_{max}) on the moving agent varies with varying preferred speed and deflection force amplitude. The blue, green, red, and yellow curves correspond to a preferred speed of 1 m/s, 3 m/s, 5 m/s, and 7 m/s. First, we notice the steady increase in the minimum separation with increasing deflection force. When $A^d_{\text{avoid}}/A_{\text{crowd}} = 0.1$, the minimum separation is around 1 m for all preferred speeds. For $A^d_{\text{avoid}}/A_{\text{crowd}} = 0.5$, the minimum separation has increased to 2-3 m. The other important result to note, is the sharp increase in maximum acceleration with

increasing preferred speed when $A^d_{\text{avoid}}/A_{\text{crowd}}$ is around 0.1 or less. Note also that there is a minimum in the recorded maximum acceleration for $A^d_{\text{avoid}}/A_{\text{crowd}} \approx 0.15$

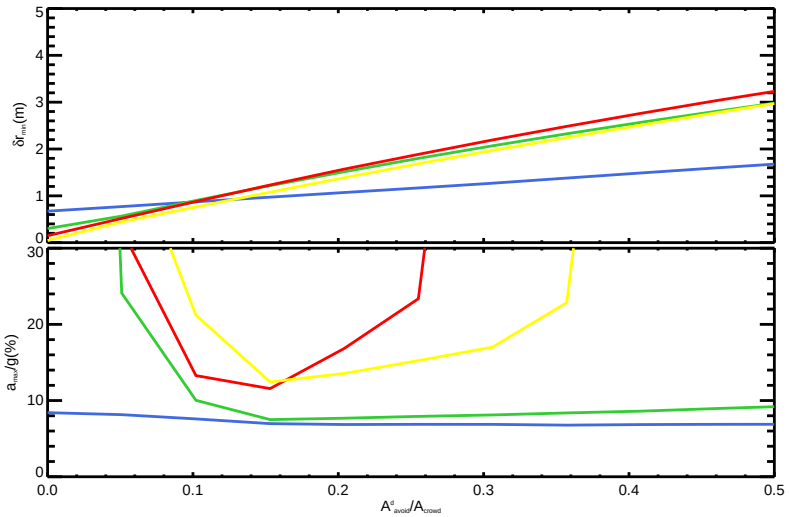

Figure 6.4 Simulation of a moving agent originally on an almost head-on collision course with a static agent. Top and bottom panels show the minimum separation (in metres) and maximum acceleration (in percentage of g), respectively, as functions of the ratio A^d_{avoid}/A_{crowd}. The preferred speed of the moving agent is 1 m/s (blue), 3 m/s (green), 5 m/s (red), and 7 m/s (yellow).

Observational data should determine what is a realistically minimum separation between a moving and a static agent. For now, we assume that 1.5-2.5 m is reasonable. If we in addition aim at minimizing the recorded acceleration, we can conclude that the results in Fig. 6.4 point towards an optimal value of $A^d_{\text{avoid}}/A_{\text{crowd}}$ of around 0.15. This also implies that A^d_{avoid} and A^r_{avoid} are comparable in size. In Fig. 6.5, we have plotted the path of the moving agents for the 4 different choices of preferred speed with $A^d_{\text{avoid}}/A_{\text{crowd}} = 0.15$. The colour of the different curves indicates the agent speed, while the colour of the filled circles shows the acceleration magnitude. We see that there are relatively small variations in the flow path for different preferred speeds. Also, there are no sharp changes of direction, which is consistent with a moderate acceleration.

6.3.2 Symmetric meeting

Now, we look at the case where both agents are moving. One agent is original placed at $\boldsymbol{r}_{a,0} = (-15\text{ m}, -0.025\text{ m})$ with a preferred location at $\boldsymbol{r}_{a,1} = (30\text{ m}, -0.025\text{ m})$. The other agent is original placed at $\boldsymbol{r}_{b,0} = (15\text{ m}, 0.025\text{ m})$ with a preferred location at $\boldsymbol{r}_{b,1} = (-30\text{ m}, 0.025\text{ m})$. Just as in the previous test case, the minimum separation between the two agents would only be about 25% of the agent radius if the agents had moved in straight lines between their respective original and preferred locations.

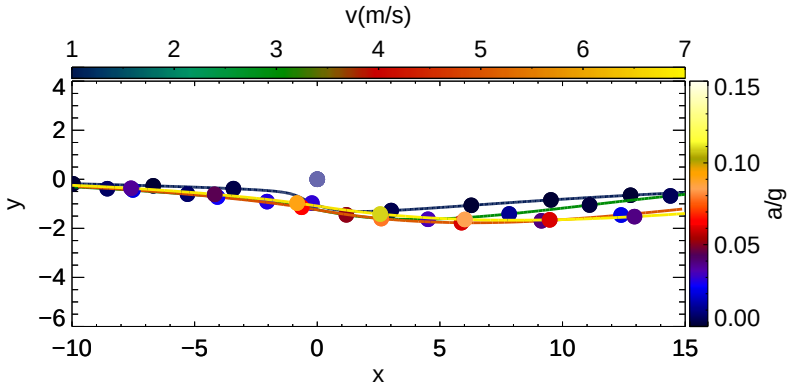

Figure 6.5 Flow pattern of a single agent originally on an almost head-on collision course with a static agent. The deflection ratio, A^d_{avoid}/A_{crowd}, is equal to 0.15. The colour of the different curves indicates the agent speed, while the colour of the filled circles shows the acceleration magnitude.

Figs. 6.6 and 6.7 show the simulation results corresponding to Fig. 6.4 and 6.5, respectively. The level of the maximum acceleration has increased for high preferred speeds relative to the asymmetric case. This is reasonable since the relative velocity between the two agents is doubled from the asymmetric to the symmetric case. Other than that, Fig. 6.6 confirms the result found in the simulation of the asymmetric meeting that the maximum acceleration experienced by the agents is at its lowest for $A^d_{\text{avoid}}/A_{\text{crowd}}$ around 0.15. The flow pattern in Fig. 6.7 is just as smooth as the one seen in Fig. 6.5. Both figures also reveal a generic weakness in crowd force models: It takes a certain time, due to inertia, from a moderately strong force starts to act until the accumulated effect on the velocity is noticeable. As a consequence, the greatest effect on the trajectories of the agents seen in Figs. 6.5 and 6.7 are after the agents have passed each other. In reality, a human would act earlier to produce a trajectory which is roughly symmetric about the point of meeting (Moussaïd, Helbing & Theraulaz, 2011).

6.4 Crowd naviagtion (e_{avoid} and ρ_{avoid})

In section 6.3, we determined an appropriate deflection force level in low density situations where the velocities can be relatively large. We know from experience that the deflection force should increase with increasing density until it reaches some, not too large, upper limit. For this reason, we introduced the deflection factor $D_{\text{avoid}}(\rho) \geq 1$ (defined in Eq. 4.6) in the expression for the deflection force (see Eq. 4.7). Now, we need to find appropriate values for the two parameters e_{avoid} and ρ_{avoid} which, together with the local density, gives us $D_{\text{avoid}}(\rho)$.

To calibrate the parameters, we study a problem where a single agent a is to navigate through

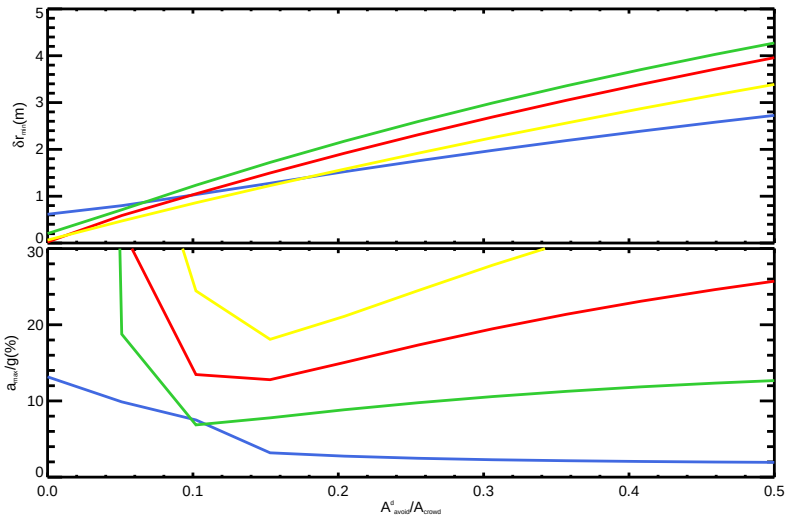

Figure 6.6 Simulation of two agents originally on an almost head-on collision course. Top and bottom panels show the minimum separation (in metres) and maximum acceleration (in percentage of g), respectively, as functions of the ratio A^d_{avoid}/A_{crowd}. The preferred speed of the agents is 1 m/s (blue), 3 m/s (green), 5 m/s (red), and 7 m/s (yellow).

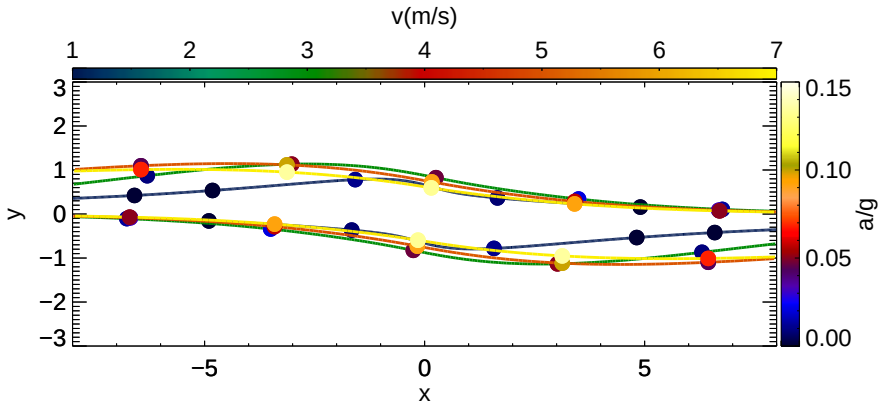

Figure 6.7 Flow pattern of two agents originally on an almost head-on collision course. The deflection ratio, A^d_{avoid}/A_{crowd}, is equal to 0.15. The colour of the different curves indicates the agents speed, while the colour of the filled circles shows the acceleration magnitude.

static crowds of different densities. The position of the agents in the crowd follow roughly a grid configurations, although with substantial random noise superimposed. Agent a is to navigate the crowd at an optimal angle of 34 degrees relative to the axis, at a desired speed of 1.4 m/s. Each simulation is run for 30 s, or until agent a has moved 15 m in the preferred direction. We perform simulations with crowd density varying between 0.36 m^{-2} and 2.4 m^{-2} and D_{avoid} ranging from 1 to 10 with 25 unique simulation setups in all. To minimize the effects of stochastic noise, all 25 setups are simulated 5 times with different starting seed for the random number generator. This means a total of 125 individual simulations. Fig. 6.8 illustrates the obtained trajectories of agent a for one particular starting seed. The colour of each of the trajectories indicate the chosen value of D_{avoid}, ranging from 1 (black) to 10 (yellow). The arrows show the instantaneous velocity of a where the colour of the arrows becomes darker as the velocity decreases.

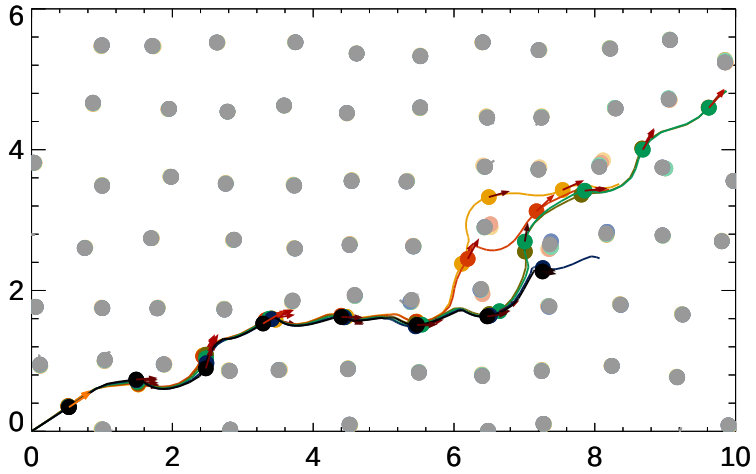

Figure 6.8 Trajectories of agent a navigating through a crowd where the density is approximately 1.2 m^{-2}. The deflection factor (D_{avoid}) is set to 1 (black), 2 (blue), 4 (green), 6 (olive), 8 (red), and 10 (yellow), and the arrows indicate the instantaneous velocity (darker arrows correspond to lower velocities).

We immediately see that the black trajectory, corresponding no increase in the deflection force amplitude relative to the low density limit, exhibits several sharp bends and ends well before the agent has moved 15 m. The corresponding velocities are small. The blue trajectory corresponds to $D_{\text{avoid}} = 2$. Again, the trajectory has sharp bends with corresponding low velocities. For larger values of D_{avoid}, the trajectories become much more smooth with corresponding larger velocities. We note that the difference between $D_{\text{avoid}} = 4$ (green curve) and $D_{\text{avoid}} = 6$ (olive curve) is negligible. In both cases, the agent has moved the specified distance of 15 m in less than 30 s. The trajectories of $D_{\text{avoid}} = 8$ (red curve) and $D_{\text{avoid}} = 10$ (yellow curve) do not extend as far as 15 m from the starting point. This indicates that D_{avoid} has become too large and that the optimal value of D_{avoid} lies in the range 4-6.

To further investigate how the motion of agent a depends on D_{avoid} for different crowd densities, we construct the time integrated quantity L_a defined as

$$L_a = \sum_i \delta t_i \frac{|dv_{a,i}/dt|}{\hat{v}_{a,i}}, \tag{6.2}$$

where δt_i is the time between snapshots i and $i-1$, $|dv_{a,i}/dt|$ is the norm of the acceleration of a at snapshot i, and $\hat{v}_{a,i}$ indicates how large the velocity component parallel to the normalized preferred velocity ($\hat{\boldsymbol{u}}_a$) is:

$$\hat{v}_{a,i} = \begin{cases} \boldsymbol{v}_a \cdot \hat{\boldsymbol{u}}_a + 10^{-4}\text{m/s} & \text{if } \boldsymbol{v}_a \cdot \hat{\boldsymbol{u}}_a > 0; \\ 10^{-4}\text{m/s} & \text{otherwise.} \end{cases} \tag{6.3}$$

In general, we are interested in identifying a model where the acceleration is relatively small, while the velocity is relatively large. In other words, smaller values of L_a indicate better models.

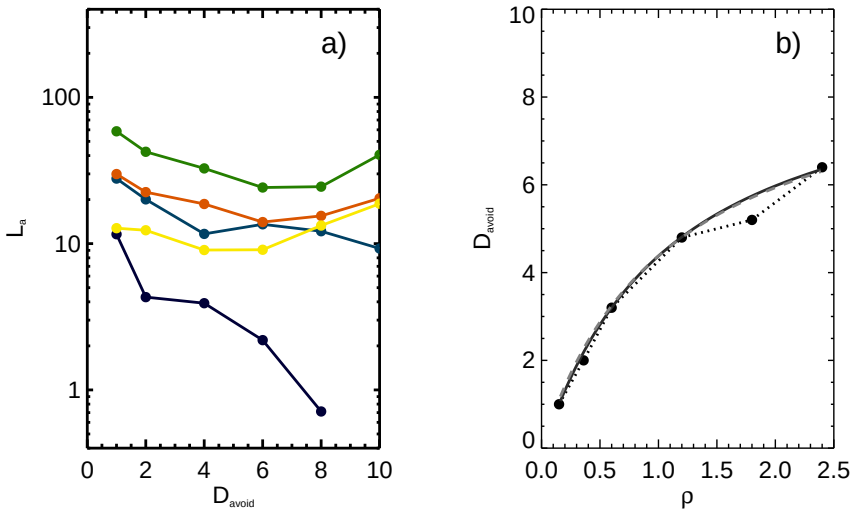

Figure 6.9 *Time-integrated quantity L_a for agent a plotted as function of the deflection factor D_{avoid} (left-hand panel) and optimal deflection factor as a function of density (right-hand panel). The curves in the left-hand panels correspond to average crowd density equal to 0.36 m^{-2} (black), 0.6 m^{-2} (blue), 1.2 m^{-2} (green), 1.8 m^{-2} (red), and 1.8 m^{-2} (yellow). The dotted and solid curves in the right-hand panel show the numerical results and the analytical results given by Eq. 4.6 with $e_{avoid} = 9.2$ and $\rho_{avoid} = 1.1$ m^{-2}.*

We calculate L_a for all simulations, and we average over the 5 simulations with identical model parameters. The results are plotted in the left-hand panel of Fig. 6.9 where the time-integrated L_a is plotted as function of the deflection factor, D_{avoid}. The curves correspond to average crowd density equal to 0.25 m^{-2} (black), 0.36 m^{-2} (blue), 0.60 m^{-2} (green), 1.2 m^{-2} (red), and 2.4 m^{-2} (yellow), and the filled circles correspond to the simulated values of D_{avoid}. For all but

the smallest simulated density level, we see that L_a is much larger than unity when $D_{\text{avoid}} = 1$. When D_{avoid} is increased, we see that L_a at first decreases for all simulated density levels. When D_{avoid} is increased above a certain value, L_a starts to increase. Depending on density, we can therefore identify an optimal value of D_{avoid}. The dotted line in the right-hand panel of Fig. 6.9 shows the optimal value of D_{avoid} found in the crowd navigation tests as a function of density.

Now we can fit the deflection parameters e_{avoid} and ρ_{avoid} to best fit the simulated data just described. The simplified model for the deflection factor (D_{avoid}) can fit the numerical data with sufficiently high accuracy. if we choose $e_{\text{avoid}} = 9.2$ and $\rho_{\text{avoid}} = 1.1$ m^{-2}. The solid line in the right-hand panel of Fig. 6.9 shows how D_{avoid} will vary when D_{avoid} no longer is a free parameter but rather a function of e_{avoid} and ρ_{avoid} as given by Eq. 4.6.

6.5 Agent pair equilibrium ($A^r_{\text{will}}/A^v_{\text{will}}$ and σ_{min})

The next model constants to be determined are A^r_{will} and σ_{min}, parameters associated with the displacement will force defined in section 3.1. To determine the effects of these parameters, we set up a test involving two identical agents who share the same preferred location. We assume a quasi-static situation where agent velocities are negligible compared to the preferred speed. The displacement and flow will forces will draw the agents towards the preferred location, while the mutual crowd repulsion will prevent the two agents from colliding. For a given choice of A^r_{will} and σ_{min}, force equilibrium is achieved at a given distance δz from the preferred location. As before, we assume $A_{\text{crowd}}/A^v_{\text{will}} = 6$. Fig. 6.10 shows at what distance the two agents experience force equilibrium as a function of the ratio between the displacement will force amplitude and the flow will force amplitude. The effect of varying σ, the scale length of the displacement, in increments of 1.0 m is illustrated by the different curves in the plot. The grey curve corresponds to $\sigma = 1.0$ m, while in the other end of the scale, the results for $\sigma = 8.0$ m are represented by the yellow curve. It is a reasonable requirement that the permanent separation between the two agents should not be less than around 1.0 m. This corresponds to $\delta z \geq 0.5$ m. From inspecting Fig. 6.10, we see that $A^r_{\text{will}} = A^v_{\text{will}}$ and $\sigma = 4.0$ m will result in $\delta z \approx 0.6$, which corresponds to a inter-agent separation of 1.2 m. As default values, we choose $A^r_{\text{will}} = A^v_{\text{will}}$ and $\sigma_{\text{min}} = 4.0$ m.

6.6 Single agent boundary avoidance ($C_{\mathcal{B}}$ and $q_{\mathcal{B}}$)

The boundary avoidance model described in section 5.3.1 relies on 3 not yet determined parameters, $C_{\mathcal{B}}$, $q_{\mathcal{B}}$, and $p_{\mathcal{B}}$. The parameters are coupled in a non-linear way which makes it difficult to determine one parameter at the time. First, we focus on two single agent scenarios where the crowd density is negligible. In this case, $p_{\mathcal{B}}$ is not an important parameter. In the first scenario, the agent moves from a start location roughly 20 m from a straight wall, towards a target location 1 m in front of the wall. In the second scenario, we make a 1 m wide opening in the wall and specify that the agent should move through the passage towards a target location on the far side of the wall. A large set of simulations is performed, varying $C_{\mathcal{B}}$ between 1.6

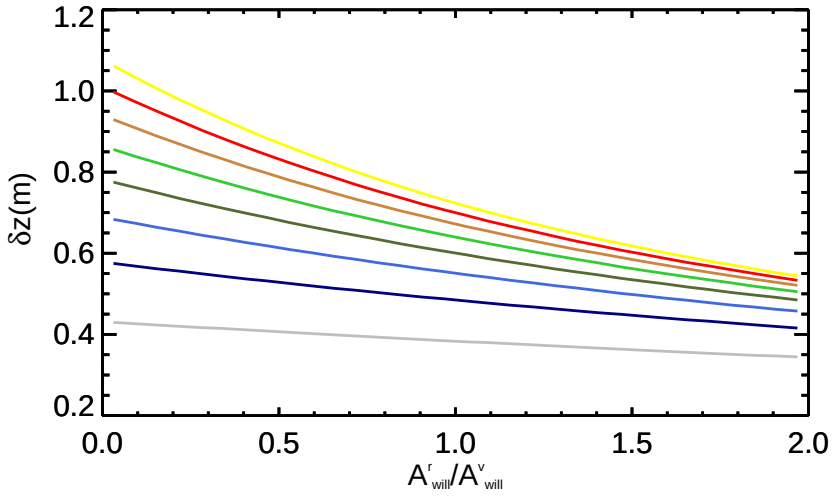

Figure 6.10 *Equilibrium distance, δz from preferred location as a function of the ratio between the displacement and flow will force amplitudes, A^r_{will}/A^v_{will}, when two isolated agents share the same preferred location. The scale length of the displacement force, σ, range from 1 m (grey) to 8 m (yellow).*

and 2.8, $q_{\mathcal{B}}$ between 3.0 and 6.0, with the optimal speed of the agent, u_a chosen between 1.0 m/s and 8.0 m/s.

The aim is to arrive at a model where the agent stops close to the target location without hitting the wall and with a mean speed which is reasonably close to the optimal speed. To assess the outcome of the simulations, we define 3 observable quantities $a_{\max}$, δv, and δr. The first observable represents the maximum acceleration experienced by the agent. The second observable is found as the difference between the optimal speed and the time-averaged speed of the agent, normalized by the optimal speed. The last observable is defined as the distance from the agent to the target location at the point of closest encounter with the wall. Better models result in overall smaller values of the three observables. Therefore, we define an upper acceptance limit associated with each of the 3 observables. The criteria for accepting the model is that each of the 3 observables are smaller than the corresponding limits $a_{\lim}$, $\delta v_{\lim}$, and $\delta r_{\lim}$. Dividing the observables by the corresponding limits, give us the ratios:

$$R_a = \frac{a_{\max}}{a_{\lim}}, \tag{6.4}$$

$$R_v = \frac{\delta v}{\delta v_{\lim}} \tag{6.5}$$

and

$$R_r = \frac{\delta r}{\delta r_{\lim}}, \tag{6.6}$$

which can be combined into a single scalar quantity

$$R_{\text{wall}} = R_a R_v R_r. \tag{6.7}$$

For the first scenario, we have chosen $a_{\text{lim}} = g$, $\delta v_{\text{lim}} = 0.3$, and $\delta r_{\text{lim}} = 0.5$ m. For each combin-

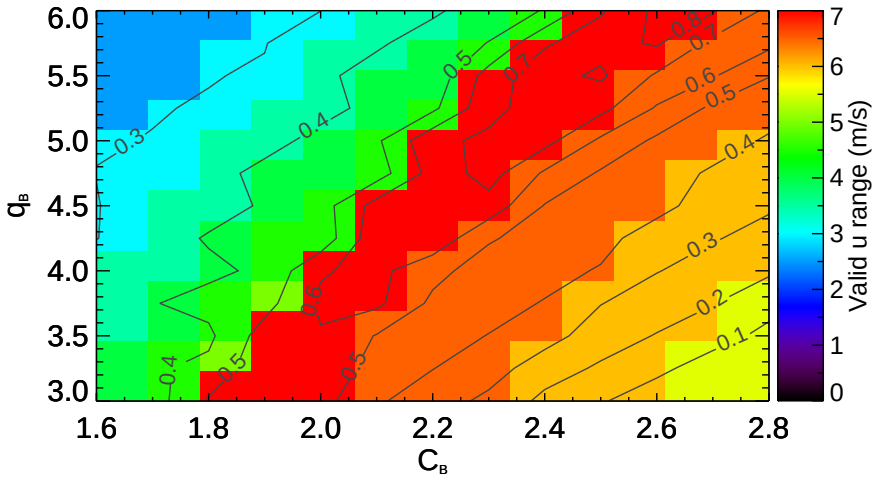

Figure 6.11 *Parametric study of a single agent moving towards a straight wall. The colour indicates the range of optimal speed which resulted in observables below the acceptance limits. The contour lines indicate the value of* $R_{\text{wall}}(C_{\mathcal{B}}, q_{\mathcal{B}})$.

ation of selected values of $C_{\mathcal{B}}$, $q_{\mathcal{B}}$ and u_a, a simulation is run and R_{wall} is calculated. If $R_a < 1$, $R_v < 1$, and $R_r < 1$, the particular pair of model parameters $(C_{\mathcal{B}}, q_{\mathcal{B}})$ is accepted as *valid* for a given optimal speed u_a. Alternatively, the model is said to *fail* for the current optimal speed. Let $R_{\text{wall}}(C_{\mathcal{B}}, q_{\mathcal{B}}, u_a)$ denote the calculated value of R_{wall} for the selected parameter values $C_{\mathcal{B}}$, $q_{\mathcal{B}}$ and u_a, and let $\bar{R}_{\text{wall}}(C_{\mathcal{B}}, q_{\mathcal{B}})$ denote the average of R_{wall} over all u_a where the given model is valid.

Fig. 6.11 summarizes the results of more than 2500 simulations of the first scenario in a $(C_{\mathcal{B}}, q_{\mathcal{B}})$-diagram. The colours show the range of the optimal speed in which a specific model is valid. The red areas indicate the models which are valid for all tested optimal speed values, corresponding to a range of 7 m/s. The turquoise areas on the other hand, indicate models which are valid only in about half the tested u_a range. The contour lines show $\bar{R}_{\text{wall}}(C_{\mathcal{B}}, q_{\mathcal{B}})$. A smaller contour line value indicates a better description of the problem within the valid optimal speed range. When looking for the optimal choice for $C_{\mathcal{B}}$ and $q_{\mathcal{B}}$, we need to identify a model which provide both a large range of valid u_a and a small average value of $\bar{R}_{\text{wall}}(C_{\mathcal{B}}, q_{\mathcal{B}})$ among the valid simulations. We see from Fig. 6.11 that the two model parameters are coupled so that there are several unique pairs of parameters that give roughly the same result. The models which are valid in the full optimal speed range is found loosely by the line $4.3C_{\mathcal{B}} + 5 = q_{\mathcal{B}}$.

The contour lines of Fig. 6.11 seem to indicate that choosing smaller values of $C_{\mathcal{B}}$ and $q_{\mathcal{B}}$ are better. Remember that $q_{\mathcal{B}}$ determines how sensitive the boundary avoidance force is to the angle between the direction of movement and the relative position of the boundary. In the first scenario, the wall was directly in front of the agent and the angle in question was

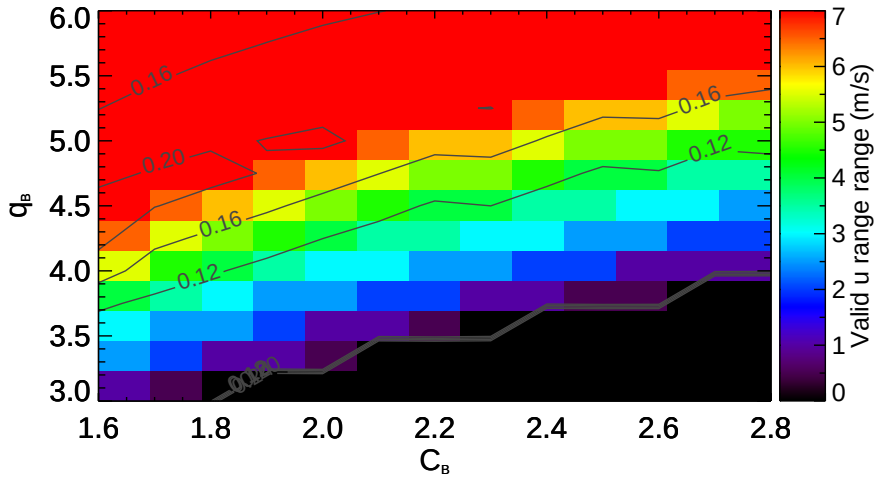

Figure 6.12 *Parametric study of a single agent moving through a 1-m wide passage in a straight wall. The colour represents the range of optimal speed which resulted in agent dynamics within the defined limits. The contour lines indicates the value of* $\bar{R}_{wall}(C_{\mathcal{B}}, q_{\mathcal{B}})$.

therefore zero throughout the simulation. As a consequence, the simulation results were not very sensitive to the choice of $q_{\mathcal{B}}$. In the second scenario, on the other hand, the agent is going to pass through a 1-m wide passage. In the beginning, the situation is very similar to the first simulation because the walls are almost directly in front of the agent. But when the agent is close to the passage, the angle between the direction of movement and the relative position of the boundaries increases. A higher value of $q_{\mathcal{B}}$, results in a stronger decrease in the boundary avoidance force as the angle increases, which in turn means the agent can pass through the passage more easily. Fig. 6.12 shows a plot similar to that of Fig. 6.11, but this time for the scenario with a passage. In this case, the agent goes through the passage and does not stop in front of the wall. The observable R_r is therefore not relevant in this case and is therefore assumed to be 1. For the two remaining observables, R_a and R_v, the limits are this time $a_{\text{lim}} = g$ and $\delta v_{\text{lim}} = 0.8$, respectively. From Fig. 6.12, we see that the performance of the models is now highly dependent on $q_{\mathcal{B}}$ and only weakly dependent on $C_{\mathcal{B}}$. To ensure that we have a model which is valid for both scenarios for the full range of u_a, we should choose $q_{\mathcal{B}} > 5$ and $C_{\mathcal{B}} \approx 2.5$. Based on this analysis, we choose $q_{\mathcal{B}} = 6$ and $C_{\mathcal{B}} = 2.5$ as default values.

6.7 Homogeneous crowd stopping near boundary ($p_{\mathcal{B}}$)

Having determined $C_{\mathcal{B}}$ and $q_{\mathcal{B}}$, we are left with only one undetermined boundary avoidance parameter, namely $p_{\mathcal{B}}$. Since this parameter controls how much the boundary avoidance force increases with increasing crowd density, we formulate a scenario involving a uniform crowd. The agents in the crowd are identical and placed in a lattice configuration. Just as in the first of the two single agent scenarios in section 6.6, the agents move towards a straight wall. The

target location of each agent is chosen so that the entire crowd should move in an almost fixed formation towards the wall, stopping 1 m in front of the wall. This test is far more challenging than the corresponding single agent test, especially for higher optimal velocities. This is because the boundary avoidance force acts primarily on the agents closest to the boundary and not so much on the agents further away from the boundary. As the agents closest to the boundary have started to slow down due to the repulsive force of the boundary, the agents further away from the boundary are still moving forward at more or less full speed. As a consequence, the first line of agents will be pushed up against the boundary. We analyse the dynamics of the agents closest to the boundary just as we did with the single agent in the first scenario in section 6.6, this time with $a_{\text{lim}} = g$, $\delta v_{\text{lim}} = 0.8$, and $\delta r_{\text{lim}} = 0.8$ m. If we change the parameter $p_{\mathcal{B}}$, the optimal speed in the crowd (u), or the crowd density (ρ), the observed R_{wall}, given by Eqs. 6.7, will change. Indirectly, we can therefore regard R_{wall} to be a function of $p_{\mathcal{B}}$, u, and ρ. To assess the results, we define a new quantity $P_{\text{sum}}(p_{\mathcal{B}})$ which is derived from R_{wall} as

$$P_{\text{sum}}(p_{\mathcal{B}}) = \left[\frac{1}{N_u N_\rho} \sum_{k}^{N_u} \sum_{l}^{N_\rho} R_{\text{wall}}(p_{\mathcal{B}}, u_k, \rho_l) \right]^{1/3}, \tag{6.8}$$

where $N_u = 5$ and $N_\rho = 4$ is the number of simulated values of u and ρ, respectively. The simulated values of u is in the range 1.0-5.0 m/s, while ρ is chosen to be in the range 0.1-1.0 m^{-2}. Note also that P_{sum} is a sum over all simulations of the crowd scenarios and not only those where the observables are below the defined limits. Fig. 6.13 shows P_{sum} as a function of $p_{\mathcal{B}}$. Just as in the case with the single agent scenarios, the colours indicate the size of the range of u where the results are valid. (The colour coding is similar to that used in Figs. 6.11 and 6.12.) We see that the lowest value of P_{sum} is found for $p_{\mathcal{B}} = 4$. But we also see that the largest valid optimal speed range is obtained with $p_{\mathcal{B}} = 2$. When we also take into account cpu efficiency, we conclude that 2 is a suitable default value for the parameter $p_{\mathcal{B}}$.

7 Crowd tests

In the previous section, we calibrated the new crowd dynamics model, one or two parameters at the time using simplified analysis, both semi-analytical and numerical. In this section, we apply the new simulation model to full-scale applications. Where possible, we compare the obtained results with corresponding results from the literature. The first 3 tests deal with basic pedestrian traffic, while the last test cover a scenario more relevant to evacuation and riot management.

7.1 Full-scale simulation of uni-directional flow

The first test simply re-visits the problem of uni-directional flow, described in section 6.1. This time, the problem is formulated as a full-scale simulation in a channel which is 20 m long and 10 m wide. Solid walls limits the channel width and a periodic boundary condition causes agents leaving the right-hand boundary to re-enter at the left-hand boundary. Properties of the agents are randomly chosen according to typical distributions described in Weidmann (1992).

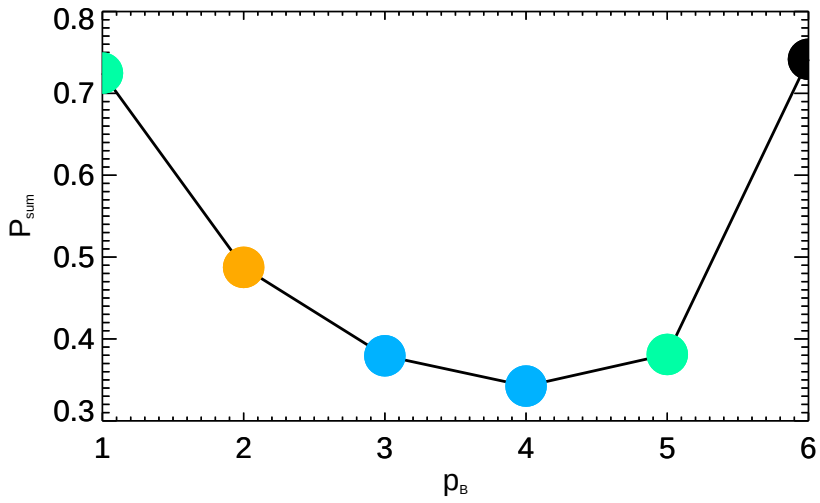

Figure 6.13 *Summary of parametric study of a crowd moving towards a straight wall. The colour indicates the range of optimal speed (u) which resulted in agent dynamics within the defined limits. The ratio of valid u range to tested u range, was (for increasing values of p_B) 0.75, 0.94, 0.69, 0.69, 0.75, and 0.19.*

Average mass, body-mass index (BMI), radius, and preferred speed is 70 kg, 24, 0.25 m, and 1.34 m/s, respectively. The standard deviation of mass, BMI, and preferred speed is 15 kg, 5, and 0.26 m/s, respectively. Maximum allowed deviation is set to 2 times the standard deviation for all 3 quantities.

In all, 7 simulations were performed with crowd density ranging from 0.5 m^{-2} to 6 m^{-2}. The simulations were terminated once a static solution had been obtained. Based on the observed average flow speeds of agents, the fundamental diagrams can be constructed similar to that shown in Figs. 6.1 and 6.2. Flow speed (v) and flow rate (J), respectively, as a functions of crowd density (ρ) are shown in the left- and right-hand panels of Fig. 7.1. The simulated results, represented by filled squares, are compared with the parametric model of Weidmann (Weidmann, 1992) (dashed line) and empirical data from Helbing, Johansson & Al-Abideen (2007) (open circles). Just as the semi-analytical model described in section 6.1, the simulated results fit well with the empirical data. The Weidmann model is partly based on data from multi-directional flow and exhibits a stronger drop in flow speed with increasing density. In conclusion, the full-scale simulation behaves as expected with the currently chosen model parameters.

7.2 Bi-directional flow in a torus-shaped channel

The second test is taken from Moussaïd et al. (2012) where it was studied both experimentally as well as numerically. The test describes a torus-shaped channel with an inner radius of 2 m and an outer radius of 4.5 m. The agents are initially placed randomly, at rest, inside the torus.

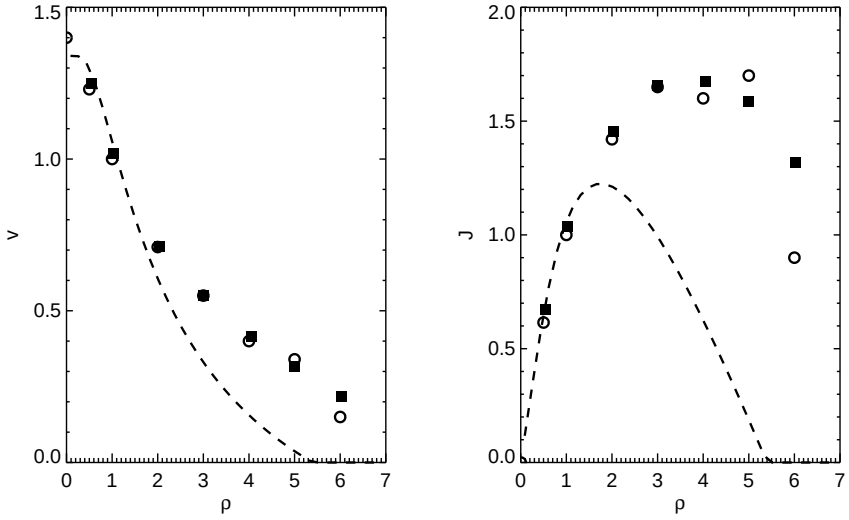

Figure 7.1 Fundamental diagrams for uni-directional pedestrian flow. The left- and right-hand panels show the flow speed (v) and flow rate (J), respectively, as a function of crowd density (ρ). The simulated results (black squares) are compared to the Weidmann model (Weidmann, 1992) (dashed line) and empirical data from Helbing, Johansson & Al-Abideen (2007) (open circles).

At the start of the test, the agents start to walk in a pre-selected, randomly chosen walking direction so that half of the agents walk clockwise, while the other half of the agents walk anti-clockwise, relative to the torus centre. All tests lasted for 60 s. In addition to numerical results, experimental trials with 30, 50, and 60 agents, corresponding to an average crowd density of 0.59 m^{-2}, 0.98 m^{-2}, and 1.18 m^{-2}, respectively, are described in Moussaïd et al. (2012). The distribution of preferred velocities inside the torus, determined by single-agent experiments, is characterized by an average preferred speed of 1.2 m/s and standard deviation of 0.16 m/s. Moussaïd et al. (2012) reported both the formation of lanes as well as instabilities due to inter-individual variability.

In this section, we report on simulations corresponding to the experimental setup described by Moussaïd et al. (2012). Fig. 7.2 shows two snapshots for each of the 3 simulations, taken after 30 s (top row) and 60 s (bottom row). Panels marked **a** and **b**, **c** and **d**, and **e** and **f** are taken from the simulations with 30, 50, and 60 agents, respectively. Each agent is represented by a filled circle and the colour of the circle indicates whether a particular agent moves clockwise (blue) or anti-clockwise (red). The coloured arrows visualize the velocity of the agents. With 30 agents, we see very clearly from panels **a** and **b** that a sorting has taken place: the agents moving clockwise are typically found at lower radial distances than the agents moving anti-clockwise. This is an example of lane formation and the lanes seem to be highly stable. Note that in Moussaïd et al. (2012), the lanes were found to be weakly unstable even in the case of just 30 agents. With 50 agents, we still typically get a two-lane structure, but this time the lanes are less stable, as can be seen in panels **c** and **d**. When 60 agents are used in the test, we see

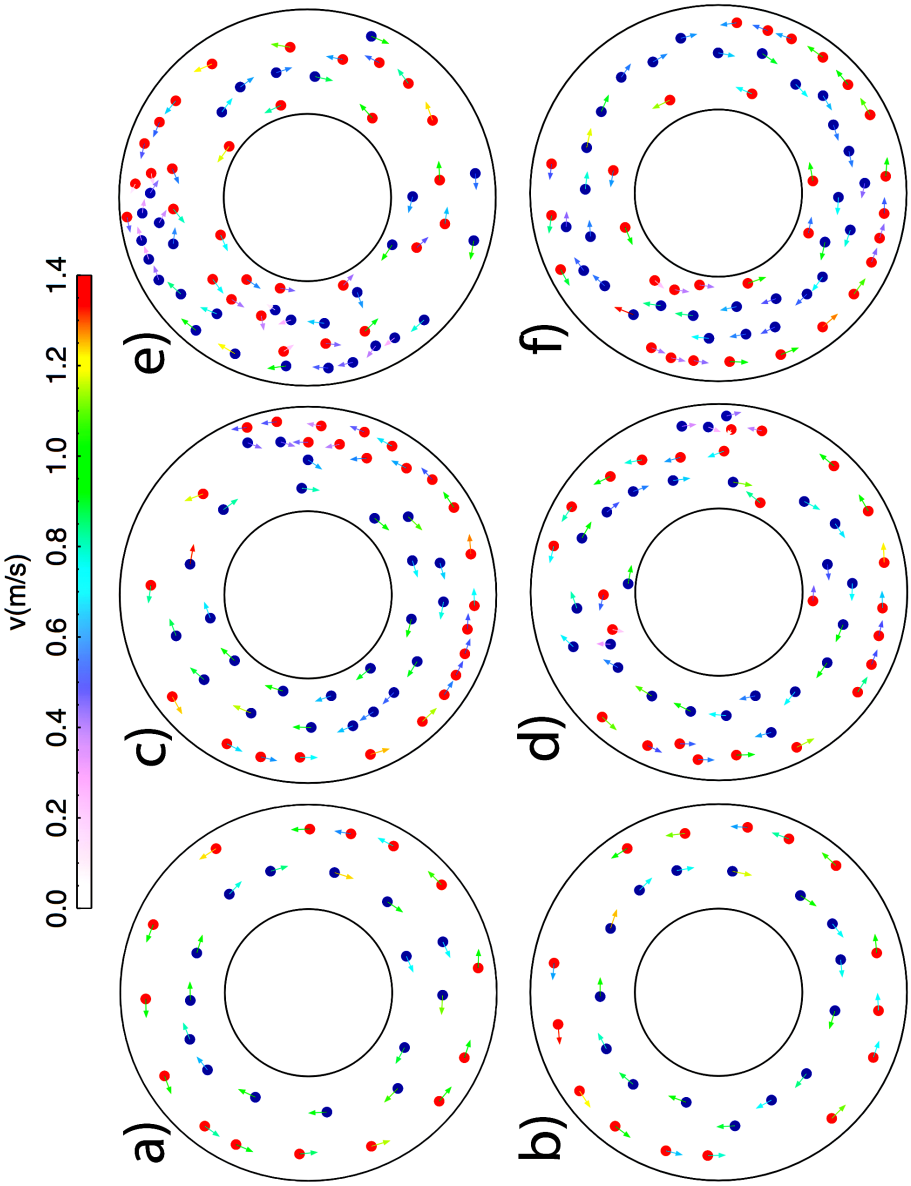

Figure 7.2 Simulation snapshots of bi-directional flow in a torus-shaped channel. The blue and red dots indicate the instantaneous location of agents moving clockwise and anti-clockwise, respectively. Corresponding velocities are shown by the coloured arrows. Panel pairs **a** *and* **b**, **c** *and* **d**, *and* **e** *and* **f** *show the agent distribution for the case with 30, 50, and 60 agents, respectively, after 30 s (top row) and 60 s (bottom row).*

from panels **e** and **f** that we at 30 s have a slightly disordered two-lane structure. At 60 s, this has evolved into a more well-defined three-lane structure: two lanes moving anti-clockwise and one lane moving clockwise.

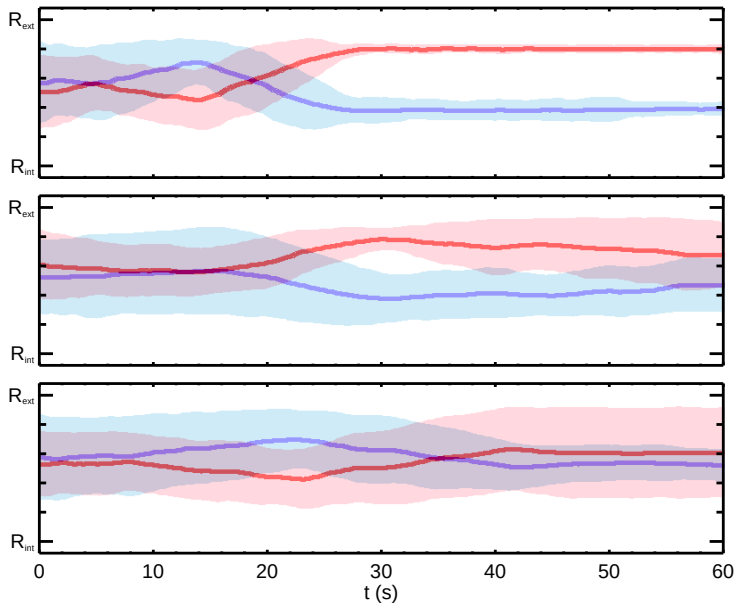

Figure 7.3 Average radial position and corresponding standard deviation for agents moving clockwise (blue) and anti-clockwise (red) as a function of time. The top, middle, and bottom panels show the results for the case of 30, 50, and 60 agents, respectively.

Two different ways of summarizing the data is shown in Figs. 7.3 and 7.4. In the first case, the blue and red lines indicate the average radial position for agents moving clockwise and anti-clockwise, respectively. The semi-transparent, blue or red zone around each line is the corresponding standard deviation. The top panel shows the results from the simulation with 30 agents. We see that it takes nearly 30 s before the clearly defined, two-lane structure has been established. This impression is confirmed by looking at the actual crowd distribution at different points in time during the first 30 s of the simulation. After 30 s, two lanes at radial positions 3 m and 4 m have formed with negligible deviation. The middle panel of Fig. 7.3, which corresponds to 50 agents, indicates a true lane formation only for a brief period around 30 s. This is only partially true, as can be seen by investigating the detailed agent distribution. It takes some time before a clear structure has been developed, but after around 12-13 s, we can identify 3-4 lanes. However, this is not a very stable configuration. Instabilities, as reported

in Moussaïd et al. (2012), causes the first structure to be broken. Around 30 s, a new two-lane structure has emerged. In turn, this structure gradually deteriorates towards the end of the simulation. In the case with 60 agents, there are several interesting observations that can be made on the basis of Fig. 7.3 (bottom panel). First, the separation into a two-lane structure is clearly visible only for a short period of time around 24 s. Furthermore, the clockwise distribution appears to become gradually more centred around the average value, which at the end of the simulation is around 3.3 m. The anti-clockwise distribution also ends up with a very similar average radial position, roughly 3.5 m, but in contrast to the clockwise distribution, the standard deviation of the anti-clockwise distribution increases with time. The reason for this, as we saw in panel **f** of Fig. 7.2, is that the anti-clockwise distribution has split up into two lanes, an inner lane at a radial position of roughly 2.2 m and an outer lane at a radial position of about 4 m.

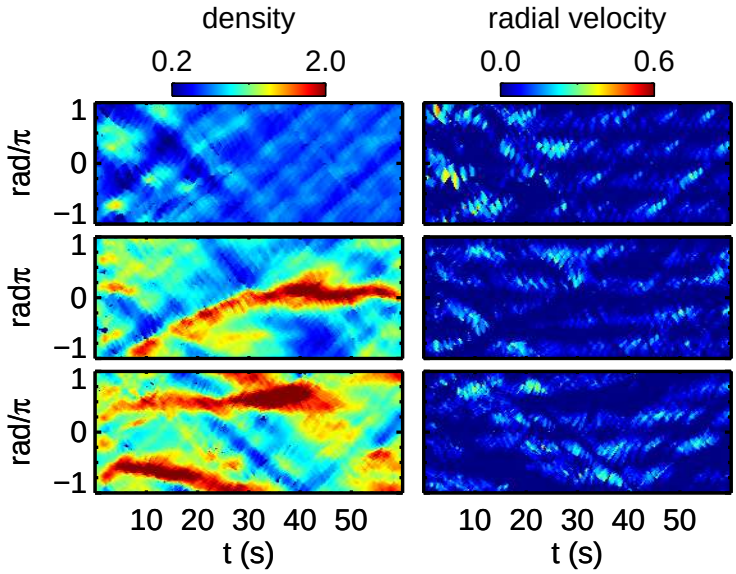

Figure 7.4 Crowd density (left panel) and radial velocity (right panel) as functions of time and angular position. The density is given in agents/m^2, while velocity is given in m/s.

Finally, we look at how density fluctuations and radial movement are distributed in time and angular position for the three simulations. This is shown in Fig. 7.4 where the panels in the left and right columns show the density and radial velocity distributions, respectively. Again, the top, middle, and bottom rows correspond to the simulations with 30, 50, and 60 agents, respectively. For both quantities, we can see traces of compression waves, although not as clearly defined as that found in Moussaïd et al. (2012). In the 30 agent case, the waves travel more or less unhindered. With 50 or 60 agents, stronger clustering of agents occur which can lead to temporary congestion. This is indicated by dark red regions which lie almost horizontally. This is not found to the same extent in Moussaïd et al. (2012). A feature which the current results have in common with the results in Moussaïd et al. (2012), is the observed correlation between local radial speed and density gaps.

7.3 Pedestrian flow through bottlenecks

Another fundamental crowd dynamics test is the problem of pedestrian flow through bottlenecks, and numerous experiments focusing on this topic has been performed (Kretz, Grünebohm & Schreckenberg, 2006; Muir, 1996; Müller, 1981; Seyfried et al., 2009). The setups might be slightly different from experiment to experiment, but the essential component is crowd flow through a corridor where the width suddenly is reduced. This creates a bottleneck, a point where a certain level of congestian is created. The aim of studies of this type is to determine how the specific flow through the bottlenecks changes with changing bottleneck width. In this work, we follow the setup proposed in Seyfried et al. (2009) and which is shown in Fig. 7.5: The upstream width of the corridor is 4 m. The agents are initially placed randomly in a start region which covers the full width of the corridor and which starts 3 m away from the bottleneck. The length of the region is adjusted so that the mean initial crowd density is 3.3 agents/m^2. The agents are initially at rest. We have performed simulations with 20, 40, and 60 agents. The properties of the agents are the same as that used in section 7.2, with the exception that the mean optimal speed is set to the more standard value of 1.4 m/s. The bottleneck width is varied from 0.6 m to 1.4 m and the total length of the bottleneck is 2.8 m. The initial position of the agents within the start region are drawn using a random number generator. However, the same seed has been used in all simulations. This means the initial positions are identical for all simulations with the same number of agents.

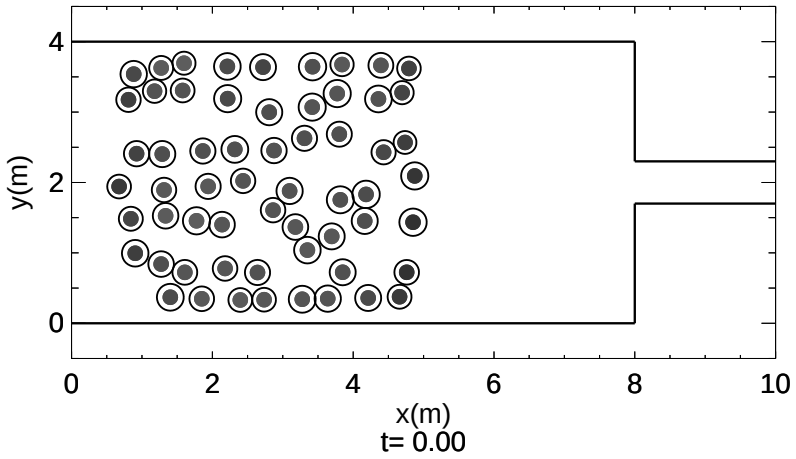

Figure 7.5 Layout of the bottleneck test together with the initial agent distribution for the case with 60 agents. The agents start to move to the right, through the bottleneck.

In Fig. 7.6 we have plotted the mean specific flow for the case with 20 (blue line), 40 (green line), and 60 (red line) agents as a function of bottleneck width (b). The simulated results are compared with experimental results taken from Kretz, Grünebohm & Schreckenberg (2006) (triangles), Müller (1981) (diamonds), Muir (1996) (squares), and Seyfried et al. (2009) (circles).

When simulating this problem, we noticed that agents at the back of the crowd typically lag slightly behind compared to the rest of the agents. This is because the repulsive force due to nearby agents in front of them is not balanced by an oppositely directed repulsive force from agents behind them. As a result, the net crowd repulsion will be larger on agents at the back of the crowd and the last group of agents to pass through the bottleneck will lag slightly behind compared to the rest of the agents. If we calculate the mean specific flow based on all agents in the crowd, we will therefore get somewhat lower values than if we calculate the mean specific flow based on half the crowd, those agents starting off closest to the bottleneck. By choosing the latter approach, as we have done, we avoid including what is really a free surface effect. The free surface effect is discussed in more detail in section 8.

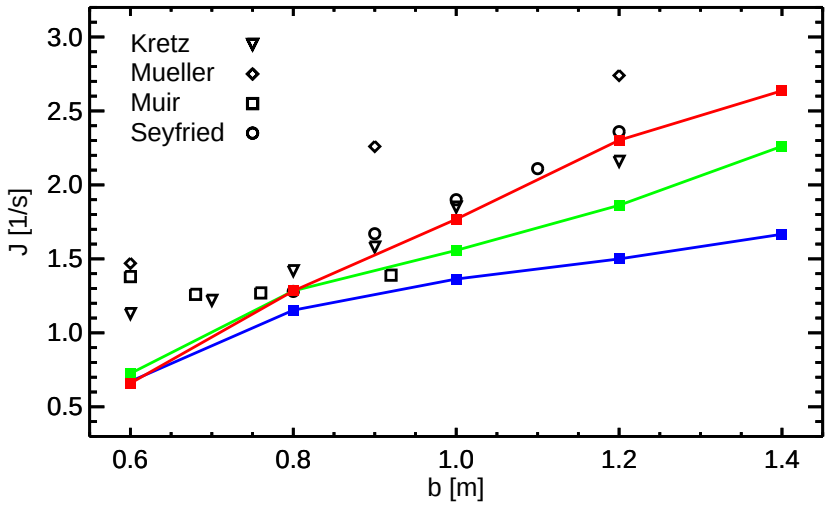

Figure 7.6 *Mean specific flow as a function of bottleneck width (b) for the case with 20 (blue line), 40 (green line), and 60 (red line) agents. The simulated results are compared with experimental results taken from Kretz, Grünebohm & Schreckenberg (2006) (triangles), Müller (1981) (diamonds), Muir (1996) (squares), and Seyfried et al. (2009) (circles).*

The simulated results in Fig. 7.6 fit reasonably well with the experimental data. This is particularly true for the simulations with 60 agents. When the number of agents in the crowd is reduced, the free surface effect becomes stronger and agents are to a larger degree slowed down before reaching the bottleneck. The difference between the experimental and simulated results therefore increase with increasing bottleneck width, especially for the case with only 20 agents. Another point worth mentioning, is the low specific flow for $b = 0.6$ m compared to the experiments. Studying this in more detail, we identify an issue related to flow through very narrow bottlenecks. If the flow upstream from the bottleneck is highly symmetric and the bottleneck is sufficiently narrow so that only one agent at the time can enter the bottleneck, then a gridlock can occur. This means, that forces are so well balanced that all movement in front of the bottleneck becomes negligible. This state of gridlock can last for up to 10 s in some cases, before

small asymmetries eventually have grown sufficiently to enable one agent to get to the bottleneck opening at the expense of the other agents. In experiments, gridlocks of this type is only likely to occur if the crowd density is very high, and even then, the time span of the gridlock is presumably much less than 10 s. Artificial gridlocking is discussed in more detail in section 8. In conclusion, the simulated results fit well with the experimental data, when the free surface effect and artificial gridlocking is negligible.

7.4 Evacuation from a building

The study of evacuation dynamics, for instance in connection with fire alarms, is an important application of crowd modelling. The final test case presented in this report describes a scenario where agents need to evacuate a 1-storey building. We have performed 7 separate tests where the level of urgency or panic in the crowd is increasing. This has been done by increasing the average optimal speed u of the agents, from 1.5 m/s to 7.5 m/s. Apart from this, the agents have the same statistical properties used in the previous two test cases. The building being evacuated has 4 rooms, varying in size from 28 m^2 (bottom left room) to 42.5 m^2(top right room). The corridors and doorways are 1.5 m and 0.8 m wide, respectively. There are two exits, one in each end of the vertical corridor. The number of agents in each room is 56 (bottom left), 68 (bottom right), 21 (top right), and 28 (top left), which results in an average initial crowd density in each room of 2.0 m^{-2}, 2.0 m^{-2}, 0.5 m^{-2}, and 0.8 m^{-2}, respectively. The layout of the building and distribution of agents at times t=0 s, 10 s, 30 s, and 50 s, can be seen in panel **a**, **b**, **c**, and **d**, respectively, of Fig. 7.7. The optimal speed is set to 3.5 m/s in this particular case. The colours of the filled circles indicate the crowd density experienced by each agent at that particular point in time. Similarly, the direction and colour of the arrows visualize the instantaneous agent velocity vectors.

This test is a good example of how the automatic path finder algorithm described in Appendix B works. The agents are initially instructed to move to the intersection between the horizontal and vertical corridors. Once they reach this area, the agents are instructed to leave the building by the nearest exit. The path finder algorithm enables the agents to identify boundaries that are obstructing the way to the destination, find the doorways, and modify the desired direction of movement accordingly. Panels **b** and **c** of Fig. 7.7 show clearly how the agents in the more densely populated rooms spread out in a characteristic arc structure near the doorways inside the rooms. When an agent has exited the room, the movement is directed towards the central corridor intersection. Having entered the corridor, an agent can typically increase the speed somewhat, although clogging near the exits eventually becomes a problem. Notice how the typical speeds are well below the average optimal speed of 3.5 m/s.

The average optimal speed (u) is regarded as an indication of the level of urgency or panic in the crowd. To see how this affects the efficiency of the evacuation, we have analysed the simulation results in more detail. The results of this analysis is summarized in Fig. 7.8. Panel **a** shows how the time required for the entire crowd to evacuate (T_{evac}) varies with increasing

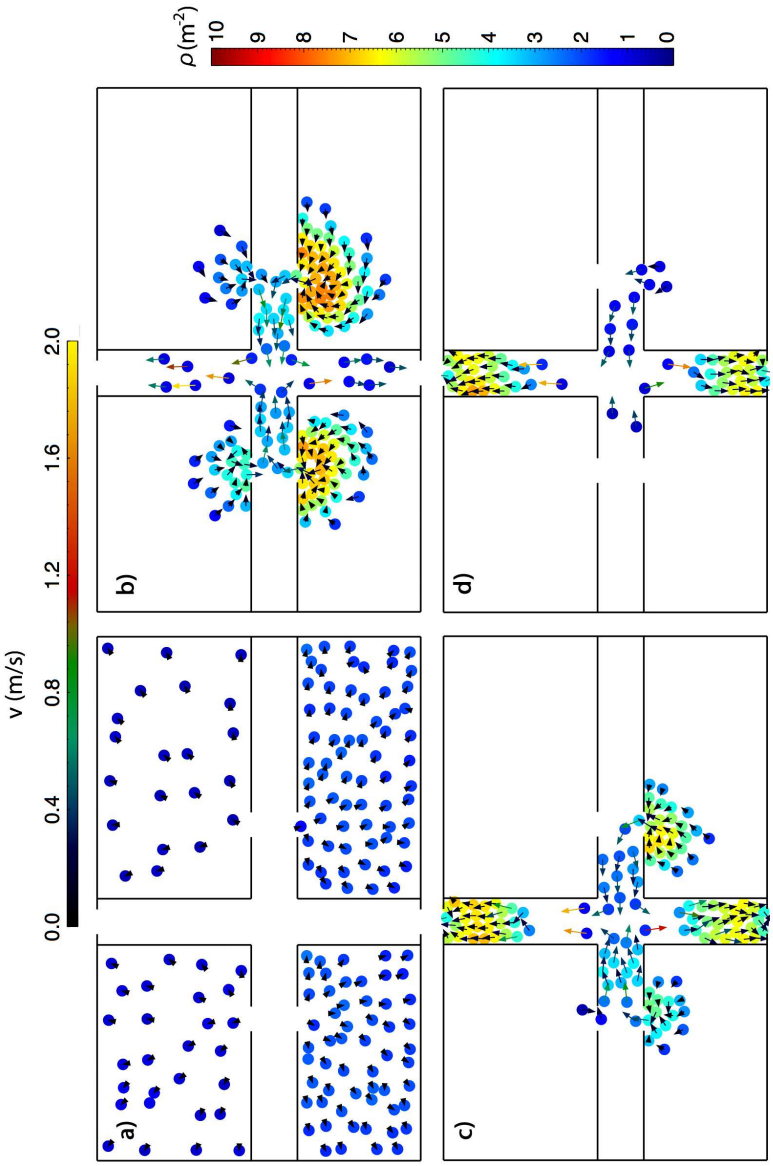

Figure 7.7 *Snapshots of the agent distribution in the evacuation simulation for the case of optimal speed (u) equal to 3.5 m/s at t=0 s (**a**), 10 s (**b**), 30 s (**c**), and 50 s (**d**). The colours of the filled circles indicate crowd density, while the direction and colours of the arrows visualize the agent velocity vectors.*

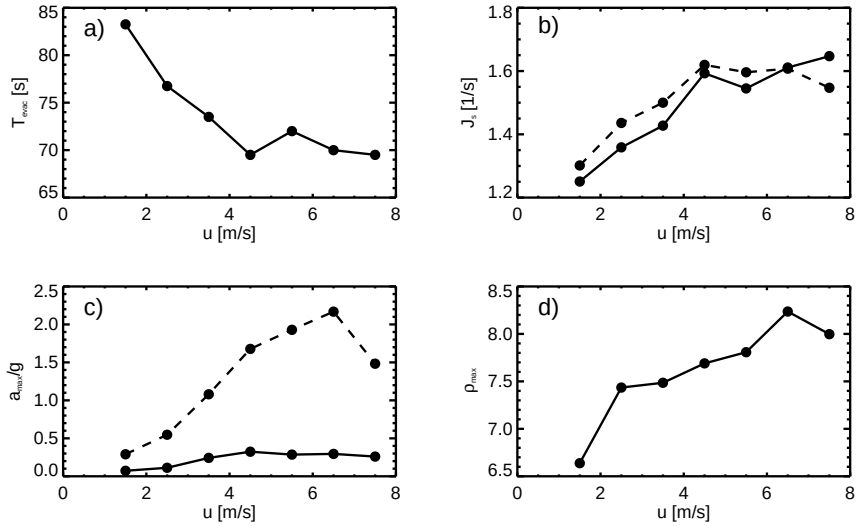

*Figure 7.8 Evacuation characteristics as functions of the average optimal speed (u). The 4 panels show the total evacuation time (**a**), the average, specific flow through the bottom (solid line) and top (dashed line) exits (**b**), the maximum 10-second (solid line) and 1-second (dashed line) averaged acceleration (**c**), and the maximum 10-second averaged crowd density.*

average optimal speed. With $u = 1.5$ m/s, T_{evac} becomes 83 s which corresponds to an effective distance of movement of about 125 m. Increasing u to 2.5 m/s should result in T_{evac} becoming roughly equal to 50 s, if the agents were free to move with their optimal speed. In reality, we see that $T_{\text{evac}} \approx 77$ s when $u = 2.5$ m/s. This indicates that the agents are slowed down substantially by the presence of the other agents. There is a small but still noticeable decrease in T_{evac} as u is increased to $u = 4.5$ m/s. Increasing u further, can cause the evacuation time to increase rather than decrease. In other words, there is a limit to how fast the particular crowd distribution used in these tests can be evacuated from the building. This limit seems to be about 69 s. Panel **b**, which shows the specific flow through each of the two exits, confirms the picture. The solid and dashed lines correspond to the bottom and top exit, respectively. Both curves show a distinct flattening for $u > 4.5$ m/s. The difference between the two curves are also interesting. More than 70% of the agents are originally located in the bottom two rooms, yet the specific flow is larger through the top exit than through the bottom exit. The only exception seems to be for the largest simulated optimal speeds. This indicates the presence of turbulent behaviour which causes flow efficiency to be reduced with increasing local density.

Another interesting point in connection with dense crowds that may or may not be in a state panic, is to what extent large forces are present in the crowd which might cause injuries and, in worst case, deaths. Table 2.1 lists estimated force thresholds for asphyxia which are in the order of 1000 N (1-minute averaged force) and 6000 N (10-second averaged force). For a typical agent of around 75 kg, this corresponds accelerations of around 1.4g and 8.2g, respectively. However, these limits are mostly relevant in scenarios involving nearly static crowds with very

high densities. In an evacuation scenario, the danger is not so much asphyxiation, but rather that people can be knocked over and trampled on. From literature (Hunter, Marshall & McNair, 2005; Kugler & Janshen, 2010) we know that horizontal manoeuvre forces rarely exceed the gravitational force of the body. Agent accelerations larger than g is therefore likely to result in agents being knocked over, possibly becoming injured, and at least creating extra obstacles which hinders the local crowd flow. We are interested in analysing the evacuation data in search of indications of agent injuries. This is particularly relevant since we are simulating crowds with high average optimal speeds (up to 7.5 m/s). Only the contact forces are relevant when considering injuries, but unfortunately the current version of the simulation software does not store information about the contact forces directly. Instead, we have to look at the acceleration. In situations with substantial physical contact, the contact forces will typically dominate over the other forces. And if the crowd is not highly uniform, the net acceleration should give a good indication of the level of contact forces.

To analyse the agent acceleration levels in the evacuation simulations, we calculate the 10-second and 1-second time averaged accelerations for each agent. Based on the averaged values, we find the maximum experienced acceleration by any agent in each of the simulations. Panel **c** shows the results as a function of u. The solid line shows the maximum 10-second averaged acceleration, while the dashed line shows the corresponding 1-second averaged acceleration. We see that the 10-second average acceleration only shows a weak increase with increasing u and never becomes large enough for there to be asphyxia-related health problems. The 1-second averaged acceleration on the other hand, has a strong increase with increasing u, with a maximum of 2.2g for $u = 6.5$ m/s. This indicates that problems of people being knocked over and possibly becoming injured could be expected for optimal speeds larger than 3-4 m/s. However, the current crowd model does not take into account that agents might lose their balance and perhaps become injured. Such a model should take into account that agents cannot move much if they do not stand on their feet and that nearby agents will also be slowed down by the immobile agents. If such a model had been included in the evacuation simulations, it is likely that the evacuation time would increase for average optimal speeds larger than 3-4 m/s.

The final panel in Fig. 7.8, panel **d**, shows the maximum 10-second averaged crowd density in the simulations. The maximum density increases with increasing u, despite the fact that the number of agents in all simulations is the same. This can only mean that there is a larger degree of clustering when the average optimal speed is larger. In turn, this means that more of the available space is empty. Crowd flow thus becomes less efficient, and the agents must compensate by using a larger net will force.

8 Conclusion

This report describes a new, robust crowd dynamics simulation model capable of simulating a wide range of human crowd behaviour with a reasonable degree of accuracy. This includes not only normal pedestrian traffic, but also scenarios such as evacuation or riots which might

involve running agents. The model relies on a number of model parameters. Default values of these parameters have been determined on the basis of fundamental properties of the human body, semi-analytical models of fundamental crowd behaviour, or simplified crowd test simulations. A summary of the most important model parameters and their default values are given in Table 8.1. A list of the forces acting on individual agents in the crowd is reproduced in Table 8.2.

Parameter	Physical interpretation	Default value	Section
$b_{A,0}$	Zero-density obstacle avoidance scale length	2.0 m	2.5.1
$b_{C,0}$	Zero-density crowd repulsion scale length	1.0 m	2.5.2
A^v_{will}	Flow will acceleration amplitude	0.25g	2.1.1
A^r_{will}	Displacement will acceleration amplitude	0.25g	6.5
σ_{min}	Displacement will force scale length	4.0 m	6.5
A^s_{will}	Velocity strain acceleration amplitude	1.5g	2.1.1
$v_{\text{lim},0}$	Activation threshold for velocity strain	6.0 m/s	2.1.1
δv_{lim}	Velocity strain width	3.0 m/s	2.1.1
$f_{\text{lim},0}$	Activation threshold for acceleration strain	0.5g	2.1.1
δf_{lim}	Acceleration strain width	0.5g	2.1.1
κ_r	Radial contact force amplitude	$5.0 \cdot 10^2 \text{s}^{-2}$	4.2
κ_t	Tangential contact force amplitude	$2.5 \cdot 10^3 (\text{ms})^{-1}$	4.2
A_{crowd}	Crowd repulsion acceleration amplitude	1.5g	6.1
θ_0	Crowd repulsion anisotropy level	0.3	6.1
A^r_{avoid}	Radial obstacle avoidance acceleration amplitude	0.225g	6.2
A^d_{avoid}	Deflection obstacle avoidance acceleration amplitude	0.225g	6.3
e_{avoid}	Maximum density-dependent deflection increase	9.2	6.4
ρ_{avoid}	Reference density in density-dependent deflection increase	1.1	6.4
$C_{\mathcal{B}}$	Boundary avoidance enhancement factor	2.5	6.6
$q_{\mathcal{B}}$	Boundary avoidance velocity exponent factor	6.0	6.6
$p_{\mathcal{B}}$	Boundary avoidance density exponent factor	2.0	6.7

Table 8.1 Summary of important numerical parameters in the new, calibrated crowd dynamics model.

The new model not only captures crowd movement well, it also provides reliable information regarding force levels which in turn can be used to assess the risk of injuries and deaths. Possible improvements to the present model include agent parameters to monitor the possible development of injuries and the effect this has on the crowd dynamics, as well as include motivation as an important factor in determining the behaviour of individual agents. Motivation is a psychological and not a physical property. Nevertheless, the idea is to link motivation to the concept of internal energy. Reduced motivation means less internal energy which results in weakened will force. Experimental data exist which show the energy consumption of a human

Force group	Force name	Equation	Relevant parameters
Internal	Displacement	3.1	A^r_{will} , σ_{min}
Internal	Flow will	3.8	A^v_{will}
Internal	Velocity strain	3.19	A^s_{will}, $v_{\text{lim},0} v_{\text{lim},0}$, δv_{lim}
Internal	Acceleration strain	3.22	$f_{\text{lim},0}$, δf_{lim}
Inter-agent	Obstacle avoidance	4.7	$b_{A,0}$, A^r_{avoid}, A^d_{avoid}, e_{avoid}, ρ_{avoid}
Inter-agent	Crowd repulsion	4.9	$b_{C,0}$, A_{crowd}, θ_0
Inter-agent	Contact	4.10	κ_r, κ_t
Boundary	Boundary avoidance	5.10	$b_{A,0}$, A^d_{avoid}, $C_{\mathcal{B}}$, $q_{\mathcal{B}}$, $p_{\mathcal{B}}$
Boundary	Wall repulsion	5.11	$b_{C,0}$, A_{crowd}, θ_0

Table 8.2 Summary of forces included in the model, the corresponding equations in this report, and which parameters from Table 8.1 are associated with each force.

body when performing various activities such as walking and running. Using this information, one could construct a basic model for temporal changes in the internal energy. Such a model should include energy consumption related to work done by the will force of an agent on its surroundings.

Also, one could try to address the two issues mentioned in section 7.3. First, it was noted that agents moving at the back of a group will experience a larger net crowd repulsion than the agents moving at the front of the group. The most straightforward method to reduce this problem is to update the position of agents using the so-called XSPH-formulation. It was first proposed to reduce problems with particle penetration in smoothed particle hydrodynamics simulations of shock waves (Monaghan, 1989). It has later been applied in a modified form to crowd modelling (Vetter et al., 2011). The idea of the method is make sure that particles (or in this case, agents) move at a velocity closer to the local average velocity. This would reduce the difference in velocity between agents located at the back of a group compared to the agents located in the front of the group. In addition, it will help avoid direct collisions between agents and could possibly also help in lane formation. The XSPH formulation is implemented by replacing the standard equation of movement (see Eq. 2.2) with

$$\frac{d\boldsymbol{r}_a}{dt} = \tilde{\boldsymbol{v}}_a, \tag{8.1}$$

where $\tilde{\boldsymbol{v}}_a$ is given as

$$\tilde{\boldsymbol{v}}_a = \boldsymbol{v}_a + \epsilon_{\text{XSPH}} \sum_b m_m \frac{\boldsymbol{v}_b - \boldsymbol{v}_a}{\rho_{ab}} \mathcal{W}_{ab}. \tag{8.2}$$

In its original form ϵ_{XSPH} is constant, with a typical value of around 0.5, but in the crowd model of Vetter et al. (2011), ϵ_{XSPH} is function of velocity and crowd densty. A problem with the XSPH-formulation is that it becomes more difficult for single agents to move in a static background population, such as shown in the crowd navigation calibration test in section 6.4. More work is therefore needed before we can formulate a satisfactory XSPH-formulation for use in crowd simulations.

The second issue identified in section 7.3 was artificial gridlocking in front of narrow bottlenecks. This occurs if the agent distribution in front of the passage is highly symmetric. Then, for a substantial period of time (for instance up to 10 s), none of the agents are able to enter the passage due to a balance between will forces, social forces and boundary forces. If a similar situation were to occur in real life, individuals in the crowd would normal take an initiative to solve the problem, either by taking the lead or by making way for others. How people react in these situations probably dependence on small details in the situation at hand but also on the psychological properties of each individual involved. The question is how this can be solved in a computer simulation. One solution could possibly be to introduce a random generated parameter, let us for now call it leadership, which indicates how likely a person is to take the lead in a gridlocked situation. The parameter could be used in a new inter-agent force which only becomes important when the velocity is much smaller than normal walking speed. Agents with a small leadership value will give way to agents with a higher leadership value. The same parameter could be used when modelling herding, the observed phenomena that some agents are more likely to follow other agents rather than choosing an individual path. This effect is particularly strong in situation where agents feel unsecure or lack detailed information about their route.

References

Daamen, W., Bovy, P.H.L., & Hoogendoorn, S.P., **Modelling pedestrians in transfer stations**, in **Pedestrian and evacuation dynamics** (eds: M. Schreckenberg & S. Sharma), 59-73, 2002.

Fruin, J.J., **Pedestrian planning and design**, Metropolitan Assoc. Urban Designers and Environ. Planners, 1971.

Fruin, J.J., **The causes and prevention of crowd disasters**, Intl. Conf. Engin. Crowd Safety, **1**, 1-10, 1993.

Helbing, D., Farkas, I., & Vicsek, T., **Simulating dynamical features of escape panic**, Nature, **407**, 487-490, 2000.

Helbing, D., Johansson, A., & Al-Abideen, H.Z., **The dynamics of crowd disasters: An empirical study**, Phys. Rev. E, **75**, 046109/1-7, 2007.

Helbing, D. & Molnár, P., **Social force model for pedestrian dynamics**, Phys. Rev. E, **51**, 4282-4287, 1995.

Hunter, J.P., Marshall, R.N., & McNair, P.J., **Relationships between ground reaction force impulse and kinematics of sprint-running acceleration**, J. Appl. Biomech., **21**, 31-43, 2005.

Kavanagh, J.J. & Menz, H.B., **Accelerometry: A technique for quantifying movement patterns during walking**, Gait & Posture, **28**, 1-15, 2008.

Kretz, T., Grünebohm, A., & Schreckenberg, M., **Experimental study of pedestrian flow through a bottleneck**, J. Stat. Mech. Theory Exper., **10**, 10014/1-20, 2006.

Kugler, F. & Janshen, L., **Body position determines propulsive forces in accelerated running**, J. Appl. Biomech., **43**, 343-348, 2010.

Lakoba, T.I., Kaup, D.J., & Finkelstein, N.M., **Modifications to the Helbing-Molnár-Farkas-Vicsek social force model for pedestrian evolution**, Simulation, **81**, 339-352, 2005.

Monaghan, J.J., **Smoothed particle hydrodynamics**, Rep. Prog. Phys., **68**, 1703-1759, 2005.

Monaghan, J.J., **On the problem of penetration in particle methods**, J. Comput. Phys., **82**, 1-15, 1989.

Moussaïd, M., et al., **Traffic instabilities in self-organized pedestrian crowds**, PLoS Comput. Biol., **8**, e1002442/1-10, 2012.

Moussaïd, M., Helbing, D., & Theraulaz, G., **How simple rules determine pedestrian behavior and crowd disasters**, Proc. Natl. Acad. Sci. USA, **108**, 6884-6888, 2011.

Muir, H.C., Bottomley, D.M., and Marrison, C., **Effects of motivation and cabin configuration on emergency aircraft evacuation behavior and rates of egress**, Int. J. Aviation Psychol., **6**, 57-77, 1996.

Müller, K., **Die Gestaltung und Bemessung von Fluchtwegen für die Evakuierung von Personen aus Gebäuden**, dissertation, Technische Hochschule Magdeburg, 1981.

Navin, P.D. & Wheeler, R.J., **Pedestrian flow characteristics**, Traffic Engin., **19**, 30-33, 1969.

Novacheck, T.F., **The biomechanics of running**, Gait & Posture, **7**, 77-95, 1998.

Older, S.J., **Movement of pedestrians on footways in shopping streets**, Traffic Eng. Control, **10**, 160-163, 1968.

Parisi, D.R., Gilman, M. & Moldovan, H., **A modification of the social force model can reproduce experimental data of pedestrian flows in normal conditions**, Physica A, **388**, 3600-3608, 2009.

Predtechenskii, V.M. & Milinskii, J.M., **Planning of foot traffic flow in buildings**, Amerind Publ., New Dehli, 1978.

Schadschneider, A. et al., **Evacuation dynamics: Empirical results, modeling and applications**, in Encyclopedia of Complexity and Systems Sci. (ed. R.A. Meyers), New York: Springer, 3142-3176, 2009.

Seyfried, A., Steffen, B., & Lippert, T., **Basics of modelling the pedestrian flow**, Physica A, **368**, 232-238, 2006.

Seyfried, A. et al., **New insights into pedestrian flow through bottlenecks**, Transportation Sci., **43**, 395-406, 2009.

Still, K.G., **Crowd dynamics**, PhD Thesis, Univ. of Warwick, 2000.

Vetter, C. et al., **SPH modelling of pedestrian crowds**, Proc. 6th Int. SPHERIC Workshop, 261-268, 2011.

Viano, D.C. & King, A.I., **Biomechanics of the chest and abdomen impact**, The Biomechanical Eng. Handbook (2nd Ed.), Ed. J.D. Bronzino, CRC Press LLC, Boca Raton, 2000.

Weidmann, U., **Transporttechnik der Fußgänger**, Schriftenreihe des IVT, **90**, ETH-Zürich, 1992.

Wendland, H., **Piecewise polynomial, positive definite and compactly supported radial functions of minimal degree**, Adv. Comp. Math., **4**, 289-396, 1995.

Yu, W.J. et al., **Centrifugal force model for pedestrian dynamics**, Phys. Rev. E,**72**, 026112/1-6, 2005.

Zhou, S. et al., **Crowd modeling and simulation technologies**, ACM Trans. Model. Comput. Simul., **20**, 1-35, 2010.

Appendix A Calculating the wall repulsion integral, I_{ab}^{wall}

In this appendix we want to derive an approximation to the integral I_{ab}^{wall} used in Eq. 5.11 to describe the strength of the wall repulsion experienced by an agent a from a nearby boundary segment b. The wall repulsion exerted on a from b is defined as the total crowd repulsion force on the agent a from the imaginary mirror agents that would fit in the exterior interaction region associated with boundary segment b. First, we derive the wall repulsion for a finite-sized but isolated, straight boundary segment where we assume the sector lines to be normal to the segment tangent. Then, the result is extended to take into account the fact that boundary segments can be connected to other segments by having common end points and that the corresponding sector lines will typically not be normal to the boundary segment tangent. Finally, we discuss how the results are generalized to curved boundaries.

A.1 Approximation to I_{ab}^{wall} with normal sector lines

Let the boundary segment b be defined by the two boundary points p_1 and p_2. We want to estimate the wall repulsion force on a given agent a, located at $\boldsymbol{r}_a$. To arrive at this first approximation to the wall repulsion, we assume that the sector lines are normal to the tangent of b (as illustrated in Fig. 5.1). The projection of a onto b, the boundary interaction point, denoted p_a, is assumed to lie somewhere between the two end points so that p_a splits b into a left- and a right-hand boundary section (indicated by the red and blue colours, respectively, in Fig. 5.1). The integration over the exterior interaction region is similarly split up into two. In the following discussion we focus on the right-hand integral, covering the boundary from the boundary interaction point to p_2. Normalized by the interaction scale length, simply denoted b_C in this case, the distance between a and p_a is z_d, the distance between p_a and p_2 is $z_{l,2}$, and the interaction range is z_{max}. We define

$$z_h = \sqrt{z_{\text{max}}^2 - z_d^2} \tag{A.1}$$

as the maximum distance from p_a along l where the interaction with a is non-zero. The smaller distance of $z_{l,2}$ and z_h is denoted z_l. The boundary normal at p_2 in the exterior interaction region (indicated by the right-hand, dotted line in Fig. 5.1) intersects the interaction circle (the dashed circle in Fig. 5.1) at the point c. The angle between the boundary normal and the vector between a and c is denoted θ and given as

$$\theta = \sin^{-1}\frac{z_l}{z_{\text{max}}}. \tag{A.2}$$

It is also useful to define the distances

$$z_c = \sqrt{z_d^2 + z_l^2} \tag{A.3}$$

and

$$z_s = z_d \tan\theta. \tag{A.4}$$

Starting with the inter-agent crowd repulsion force, given in Eq. 4.9, with the simplifying assumption that the angular dependent factor defined by Eq. 4.8 is set to unity, the wall repulsion

force on agent a from the right-hand section of boundary segment b can be estimated by

$$\boldsymbol{S}^{\mathcal{B}}_{2,ab} = -m_a A_{\text{crowd}} \rho_a b_C^2 \hat{\boldsymbol{r}}_{ab} \int_{z_d}^{z_{\max}} \int_{\alpha}^{\alpha_m(z)} \Phi(z,1) z \cos\alpha dz d\alpha. \tag{A.5}$$

We have assumed the force is strictly normal to the boundary. The radial distance from agent a is given by $b_C z$, while the angular position relative to the boundary normal through $\boldsymbol{r}_a$ is denoted α. The upper limit of the angular integration, α_m, depends on z in that

$$\alpha_m(z) = \begin{cases} \alpha_{m,1}(z) = \sin^{-1}\left(\sqrt{1 - z_d^2/z^2}\right) & \text{if } z_d < z \leq z_c; \\ \alpha_{m,2}(z) = \sin^{-1}\left(\frac{z_l}{z}\right) & \text{if } z_c < z \leq z_{\max} \end{cases} \tag{A.6}$$

Performing the angular integration of Eq. A.5, we then get

$$\boldsymbol{S}^{\mathcal{B}}_{2,ab} = -m_a A_{\text{crowd}} \rho b_C^2 \hat{\boldsymbol{r}}_{ab} \left\{ \int_{z_d}^{z_c} \Phi(z,1) z \sin\alpha_{m,1}(z) dz + \int_{z_c}^{z_{\max}} \Phi(z,1) z \sin\alpha_{m,2}(z) dz \right\}. \tag{A.7}$$

Using Eq. A.6, we rewrite Eq. A.7 as

$$\boldsymbol{S}^{\mathcal{B}}_{2,ab} = -m_a A_{\text{crowd}} \rho b_C^2 \hat{\boldsymbol{r}}_{ab} \left\{ \int_{z_d}^{z_c} \Phi(z,1) z \sqrt{1 - z_d^2/z^2} dz + \int_{z_c}^{z_{\max}} \Phi(z,1) z_l dz \right\}. \tag{A.8}$$

Before we can perform the radial integration, we need to remind ourselves of what the spatial interaction function, $\Phi(z,1)$, looks like. From Eq. 2.8 we know that

$$\Phi(z,1) = \Phi_0(z,1) \Psi\left(\frac{z - z_0}{z_w}\right), \tag{A.9}$$

where $\Phi(z,1) = 1/(z^2+1)$ and Ψ is a taper function which secures compact support. In order to simplify the evaluation of Eq. A.8, we will replace $\Psi(\xi)$ (given in Eq. 2.7) by a step function, $\tilde{\Psi}(\xi)$, which is equal to 1 for $\xi \leq \xi_h$ and otherwise equal to 0. The parameter ξ_h is found as

$$\xi_h = \int_0^2 \Psi(\xi) d\xi, \tag{A.10}$$

which is easily found to be 2/3. The effect of repacing Ψ with $\tilde{\Psi}$ as the taper function is simply to replace $z_{\max}$ by $\tilde{z}_{\max} = z_0 + \xi_h z_{\text{wid}}$ in Eq. A.8.

The first integral on the right-hand side of Eq. A.8 can now be written as

$$I_1^r(z_d, z_c) = \int_{z_d}^{z_c} \frac{\sqrt{z^2 - z_d^2}}{z^2 + 1} dz. \tag{A.11}$$

This integral can be solved analytically, but in practise, it will be more efficient to solve the integral numerically. Since $0 \leq z_d \leq z_c \leq \tilde{z}_{\max}$, the integral can be solved once with satisfactory

resolution for different values of z_d and $\tilde{z}_{\text{max}}$, stored in a look-up table and reused whenever needed. The second integral in Eq. A.8 is easier to handle since it can be written as

$$I_2^r(z_d, z_c) = z_l \int_{z_c}^{\tilde{z}_{\text{max}}} \frac{1}{z^2+1} dz = z_l \left(\tan^{-1} \tilde{z}_{\text{max}} - \tan^{-1} z_c \right). \tag{A.12}$$

Although this is easily treated analytically, the most efficient and consistent approach would be to include this term in the look-up table already required by the first term. Combining integrals I_1^r and I_2^r gives us the complete contribution to the wall repulsion force strength from the right-hand side of the interaction sector under the assumption of normal sector lines (blue region in Fig. 5.1):

$$I_\perp^r(z_d, z_c) = I_1^r(z_d, z_c) + I_2^r(z_d, z_c). \tag{A.13}$$

Following the same approach, we can determine the integrals I_1^l and I_2^l which combined gives us $I_\perp^l$, the contribution from the left-hand side of the interaciont sector (red region in Fig. 5.1).

A.2 Modifications to I_{ab}^{wall} due to boundary segment intersections

So far, we have looked at isolated boundary segments b with normal sector lines. In addition, we have assumed that a boundary interaction point for the interaction between agent a and segment b can be found. (In section 5, the boundary interaction point was defined as the intersection between the boundary segment b and the separation vector between agent a and its mirror image across b). In this section, we generalize the results in section A.1 in order to take into account the effect of connected boundary segments. We also want to be able to handle situations where no interaction point can be found. The required modifications represent rough estimates of the real solutions, and the primary aim is to achieve robust and smoothly behaving numerical solutions with a reasonable degree of accuracy.

A.2.1 End point related coordinates

First, we need to define coordinate systems associated with boundary segment end points. These coordinates are used to specify positions relative to the end points and angles relative to the segment normal vectors. Then, we define an angular weight factor which will be used in the final wall repulsion expression.

Fig. A.1 shows a boundary line A which is defined by the two end points V_0 and V_1. The segment tangent, $\hat{\boldsymbol{t}}_A$, is directed from V_0 to V_1. The segment normal, $\hat{\boldsymbol{n}}_A$, is directed so that $\hat{\boldsymbol{t}}_A \times \hat{\boldsymbol{n}}_A$ points into the simulation plain, as shown in Fig. A.1. For each of the two end points k, we introduce two coordinates, a_{tk} and β_k. The former variable is defined as

$$a_{tk} = (\boldsymbol{r} - \boldsymbol{r}_k) \cdot \hat{\boldsymbol{t}}_{A,k}, \tag{A.14}$$

where $\boldsymbol{r}_k$ is the position of end point k and $\hat{\boldsymbol{t}}_{A,0} = \hat{\boldsymbol{t}}_A$ and $\hat{\boldsymbol{t}}_{A,1} = -\hat{\boldsymbol{t}}_A$. As illustrated in Fig. A.1, a_{t0} is negative to the left of V_0 and positive elsewhere, while a_{t1} is negative to the right of V_1 and positive elsewhere. The second variable, β_k, represents the smallest angle that a

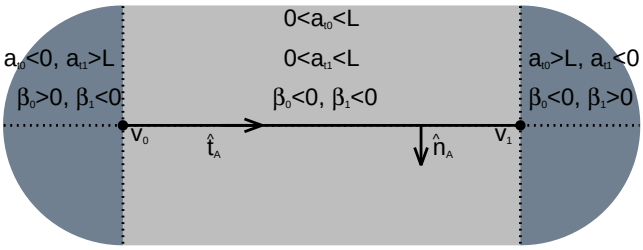

Figure A.1 Line segment A defined by end points V_0 and V_1. The tangent and normal unity vector associated with the segment is denoted $\hat{\boldsymbol{t}}_A$ and $\hat{\boldsymbol{n}}_A$, respectively. The sign of the end point specific coordinates, a_{tk} and β_k, are indicated by the annotation.

positional vector forms with an infinite line normal to the boundary segment through end point k. If we define the distance to the boundary segment, a_n, as distance to the line in the light grey region of Fig. A.1 and as the distance to the nearest end point in the dark grey regions of Fig. A.1, then β_k can be expressed as

$$\beta_k = \begin{cases} \tan^{-1}\left(\frac{\|a_n\|}{a_{tk}}\right) - \frac{\pi}{2} & \text{if } a_{tk} > 0; \\ \tan^{-1}\left(\frac{\|a_n\|}{a_{tk}}\right) + \frac{\pi}{2} & \text{if } a_{tk} < 0; \\ 0 & \text{otherwise}. \end{cases} \tag{A.15}$$

Fig. A.1 illustrates the fact that β_0 and β_1 are negative between the two end points and that they change sign at V_0 and V_1, respectively. It should also be noted that $-\pi/2 \leq \beta \leq \pi/2$. For the remaining part of this appendix, we define exterior and interior regions so that the segment normal vector points towards the exterior region. Since β_k is symmetric about the segment tangent, we always need to specify whether an angle is exterior or interior. In this context, agents might be located both in the interior and the exterior regions. The regions which contains a specific agent will be referred to as the **agent side** of a boundary segment. The region on the other side of the boundary segment will be referred to as the **mirror agent side**.

For later use, we define the angular weight factor $g(\beta)$ as

$$g(\beta) = \begin{cases} 1 & \text{if } -\pi/2 \leq \beta \leq 0; \\ 1 - \frac{2\beta}{\pi} & \text{if } 0 < \beta \leq \pi/2. \end{cases} \tag{A.16}$$

If we assume $\beta = \beta_0$, then Eq. A.16 shows that $g = 0$ along the line which is parallel to the boundary segment and which extends to the left of V_0. To the right of V_1, $g = 1$. If we instead

assume $\beta = \beta_1$, then g is mirrored about the segment midpoint.

A.2.2 Boundary segment intersections

So far, we have only looked at isolated boundary segments. But before formulating the modified wall repulsion integral, we should take a closer look at segment intersections. We assume that two or more boundary segments can only intersect by sharing a common end point. In this section, we characterize a boundary segment intersection by identifying angles in the end point coordinate systems which are used in formulating the generalized wall repulsion integral.

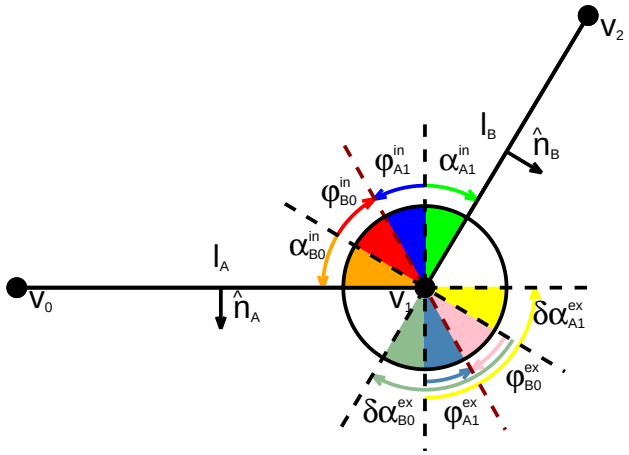

Figure A.2 *Intersection between lines A and B at end point V_1 with sector line angles $\phi^{in}_{A1} = \phi^{in}_{B0} = -\phi^{ex}_{A1} = -\phi^{ex}_{B0} < 0$. Maximum angles of visibility are correspondingly $\alpha^{in}_{A1} = \alpha^{in}_{B0} < \pi/2$, $\alpha^{ex}_{A1} = \phi^{ex}_{A1} + \phi^{ex}_{B0} + \delta\alpha^{ex}_{A1} \equiv \pi/2$, and $\alpha^{ex}_{B0} = \phi^{ex}_{B0} + \phi^{ex}_{A1} + \delta\alpha^{ex}_{B0} = \alpha^{ex}_{B0} \equiv \pi/2$.*

Fig. A.2 is a sketch of the intersection between to line segments, A and B. The two segments share a common end point, V_1, but we still use two different coordinate systems, one used by line A and one used by line B. Although not parallel, the line normal vectors are consistently defined. We therefore refer to the region above line A and to the left of line B as the interior region and the region below line A or to the right of line B as the exterior region. We note that the interior angle, $\Delta\phi^{in}_{AB}$, between the two lines is convex, while the corresponding exterior angle, $\Delta\phi^{ex}_{AB}$, is concave. The bisectors of the two angles are indicated by red, dashed lines in Fig. A.2. These are the sector lines which up until now have been assumed to be normal to the

associated boundary segments. The segment normal vectors are indicated by black, dashed lines on either side of the sector lines. The angle that the interior sector line forms with the normal of line A is marked ϕ^{in}_{A1} and indicated by the dark blue sector in Fig. A.2. The corresponding angle associated with line B is ϕ^{in}_{B0} and indicated by the red sector in Fig. A.2. We note that

$$\phi^{\text{in}}_{A1} = \phi^{\text{in}}_{B0} = (\Delta\phi^{\text{in}}_{AB} - \pi)/2 < 0. \tag{A.17}$$

If only two segments intersect at the end point in question, as is the case in Fig. A.2, then we know that $\phi^{\text{ex}}_{A1} = \phi^{\text{ex}}_{B0} = -\phi^{\text{in}}_{A1}$. Note also that if an end point k associated with boundary segment l is not shared with any other segment, then we assume $\phi^{\text{in}}_{lk} = \phi^{\text{ex}}_{lk} = \pi/2$.

In addition to modifying the sector line directions, an intersecting boundary segment can further limit the view of agents relative to that found for isolated segments. An example taken from Fig. A.2, agents located above line A and to the right of line B will only see B and not A. Agents below line A and sufficiently far to the left of line B will similarly not see B. Generally, corresponding to each sector line angle ϕ^o_{lk} of end point k associated with boundary segment l in region o (interior or exterior), there exists a maximum angle of visibility, α^o_{lk}, defined as

$$\alpha^o_{lk} = \begin{cases} \frac{\pi}{2} + 2\phi^o_{lk} & \text{if } -\frac{\pi}{2} \leq \phi^o_{lk} < 0; \\ \frac{\pi}{2} & \text{otherwise .} \end{cases} \tag{A.18}$$

From Fig. A.2, we see that α^{in}_{A1}, indicated by the bright green sector, is the angle from the interior normal of A to B. Correspondingly, α^{in}_{B0}, indicated by the orange sector, is the angle from the interior normal of B to A. In the exterior region, $\alpha^{\text{ex}}_{A1} = \phi^{\text{ex}}_{A1} + \phi^{\text{ex}}_{B0} + \delta\alpha^{\text{ex}}_{A1} \equiv \pi/2$. In the same way, $\alpha^{\text{ex}}_{B0} = \phi^{\text{ex}}_{B0} + \phi^{\text{ex}}_{A1} + \delta\alpha^{\text{ex}}_{B0} \equiv \pi/2$.

Fig. A.3 shows the slightly more complicated case of several boundary segments sharing a common end point. The 3 sector lines are indicated by dashed, coloured lines. Line A connects to line B in the interior (relative to its own normal vector) and line C in the exterior. Line B also connects to line C in the exterior. It should be pointed out that generally $\phi^{\text{ex}}_{lk} \neq \phi^{\text{in}}_{lk}$ for end point k associated with boundary segment l when more than 2 boundary segments intersect at the end point. Other than that, the generalization from two to several intersecting boundary segments is straightforward.

A.2.3 Modified wall repulsion integration

In section A.1, an expression for the wall repulsion strength, I^{wall}_{ab}, in the case of isolated boundary segments with normal sector lines was derived. Now, we are ready to formulate a modified expression which represents a better approximation in realistic scenarios with connected boundary segments.

We want to determine the strength of the wall repulsion experienced by agent a from boundary segment b. Just as in section A.1, we divided the expression into a left- and right-hand integral. So, let us focus on the right-hand integral corresponding to the right-hand end point of b. The position of agent a relative to the right-hand end point is given by the tangential coordinate

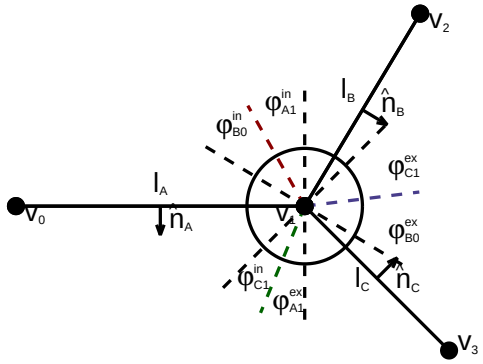

Figure A.3 Intersection between lines A, B, and C at end point V_1 with sector line angles at $\phi^{in}_{A1} = \phi^{in}_{B0}$ (red line), $\phi^{in}_{C1} = \phi^{ex}_{A1}$ (green line), and $\phi^{ex}_{C1} = \phi^{ex}_{B0}$ (blue line).

$a_{t,a}$, normal coordinate $a_{n,a}$, and angular coordinate β_a (according to definitions in section A.2.1). Normalized parameters are

$$z_d = \frac{a_{n,a}}{b_{C,a}}, \tag{A.19}$$

$$z_{l,\text{min}} = \begin{cases} 0 & \text{if } a_{t,a} \geq 0; \\ -a_{t,a}/b_{C,a} & \text{otherwise,} \end{cases} \tag{A.20}$$

and

$$z_{l,\text{max}} = \min\left(a_{t,a}/b_{C,a}, \tilde{z}_{\text{max}}\right). \tag{A.21}$$

Based on $z_{l,\text{min}}$ and $z_{l,\text{max}}$, we also define

$$z_{c,\text{lo}} = \sqrt{z_d^2 + z_{l,\text{min}}^2} \tag{A.22}$$

and

$$z_{c,\text{hi}} = \sqrt{z_d^2 + z_{l,\text{max}}^2} \tag{A.23}$$

The outer sector line angle (as viewed by the agent) is ϕ_r, while the inner maximum angle of visibility is α_r. If $\beta_a < \alpha_r$ and $z_d < \tilde{z}_{\text{max}}$, then agent a will get a contribution to the wall repulsion strength from the right-hand integral. First, we introduce the following integral notation:

$$I^r_{\text{lo}} = I^r_{\perp}(z_d, z_{c,\text{lo}}), \tag{A.24}$$

$$I^r_{\text{hi}} = I^r_{\perp}(z_d, z_{c,\text{hi}}), \tag{A.25}$$

and

$$I^r_{\text{inf}} = I^r_{\perp}(z_d, \tilde{z}_{\text{max}}). \tag{A.26}$$

Then, we can write the right-hand wall repulsion integral as

$$I^r = g(\beta_a) \begin{cases} \cos\phi_r (I^r_{\text{hi}} - I^r_{\text{lo}}) & \text{if } \phi_r \leq 0; \\ \cos\phi_r (I^r_{\text{hi}} - I^r_{\text{lo}}) + (1 - \cos\phi_r) I^r_{\text{inf}} & \text{otherwise.} \end{cases} \tag{A.27}$$

The corresponding integral for the left-hand end point is denoted I^l, so that the full strength of the wall repulsion on agent a from boundary segment b can be written as

$$I^{\text{wall}}_{ab} = I^r + I^l. \tag{A.28}$$

A.3 Wall repulsion from curved boundaries

So far, we have assumed the boundary segment to be a line. Now, we will extend the description of wall repulsion to curved boundary segments. We will do this by applying assumptions and approximations which allows us to reuse much of the results from sections A.1 and A.2.3 while still maintaining an acceptable level of accuracy. A consequence of these additional assumptions is that higher accuracy might be achieved if large boundary segments with strong curvature are split up into smaller segments with identical curvature. For example, to represent a boundary which is a full circle, it is advisable to split the boundary into at least 4 segments, each covering angles of at most $\pi/2$.

Fig. A.4 shows a sketch of a curved segment A defined by end points V_0 and V_1, origin O, and curvature R_A. The angle between to the vectors from the curve origin to each of the two end points, the curve angle, is denoted χ. We will also refer to the **equivalent line segment**, which is straight line between the two end points. Tangent and normal vectors can be related to the curved or equivalent straight boundary. When it comes to the former vector, we use the equivalent curve tangent, $\hat{\boldsymbol{t}}_A$, which is a constant vector defined using the equivalent line segment. When it comes to the normal vector, we will need to use the actual curve normal, $\hat{\boldsymbol{n}}_A$, which varies in direction along the curve. In Fig. A.4, $\hat{\boldsymbol{n}}_A$ is shown for the two end points and for the midpoint. Note that at the midpoint, the tangent and normal vectors of the curved and equivalent straight boundary are identical. If an agent a is located inside the sector defined by the curve angle χ (light grey region in Fig. A.4), then a boundary interaction point on the curve can be found and the separation vector is normal to the curve. Alternatively, if agent a is located within interaction range of one of end points (dark grey semi-circles) at a valid angle, the corresponding end point is used as the interaction point with a separation vector which reflects a mirroring about the end point.

The computation of the wall repulsion strength for curved boundary segments is almost identical to the algorithm described in section A.2.3. This means neglecting some of the differences between a curved and a straight boundary. However, the accuracy is shown in section 5.3.2 to be comparable for both types of boundary segments. The changes done in the wall repulsion algorithm to handle curved boundaries are as follows: The equivalent tangent vector, $\hat{\boldsymbol{t}}_A$, is used to determine the tangential position, $a_{t,k}$ of the agent relative to the two end

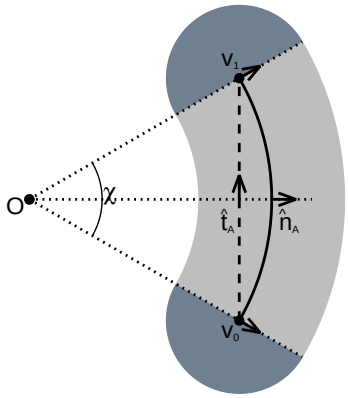

Figure A.4 *Curve segment A defined by end points V_0 and V_1, origin O, and curvature R_A is plotted with a solid line. The curve angle is denoted χ. The tangent vector, $\hat{\boldsymbol{t}}_A$, is associated with the equivalent line segment (dashed line). The normal vector, $\hat{\boldsymbol{n}}_A$, is plotted for 3 different points on the curve: the end points and the midpoint.*

points. The distance to the boundary segment, a_n, is defined as the distance to the curve in the light grey region of Fig. A.4 and as the distance to the nearest end point in the dark grey regions of Fig. A.4. The angular coordinate relative to each end point, β_k, can be found with Eq. A.15. The sector line angles, ϕ^o_{lk}, and maximum angles of visibility, α^o_{lk}, described in section A.2.2, can be found in much the same way as for lines. The only thing to remember is to use the local boundary normal at the respective end points. With these small changes, the wall repulsion algorithm described in section A.2.2, can now also be applied to curved boundary segments with an acceptable level of accuracy.

Appendix B Automatic path finder algorithm

The automatic path finder algorithm considers both boundary segments and individual vertices. Since boundaries are static (or move with an easily recognizable motion), we assume the agents can plan their route around these obstacles. Numerically, this means that the preferred direction of motion is modified in order to try avoid physical contact with solid boundaries. The implemented algorithm also take into account that the agents have a non-zero physical radius. This complicates the details somewhat but does not alter the basic principles of the algorithm. Here, we describe the overall structure of the path finder algorithm without going into any details. We look at agent a, currently at position $\boldsymbol{r}_a$ with preferred location $\boldsymbol{z}_a$ and physical diameter d_a. Primary target direction, $\boldsymbol{\delta z}^0_a$, is simply given as $\boldsymbol{\delta z}^0_a = \boldsymbol{z}_a - \boldsymbol{r}_a$. We also define alternative target direction $\boldsymbol{\delta z}^\phi_a$ by rotating $\boldsymbol{\delta z}^0_a$ by the angle ϕ (where positive rotation direction is anti-clockwise). If necessary, we will test 7 different target directions, all listed in the **target**

alternative list, $\boldsymbol{T}_z = \{\boldsymbol{\delta z}_a^0, \boldsymbol{\delta z}_a^{\pi/4}, \boldsymbol{\delta z}_a^{-\pi/4}, \boldsymbol{\delta z}_a^{\pi/2}, \boldsymbol{\delta z}_a^{-\pi/2}, \boldsymbol{\delta z}_a^{3\pi/4}, \boldsymbol{\delta z}_a^{-3\pi/4}\}$. We construct a set B of all relevant boundary segments, that is all boundary segments within interaction range of the agent, $R_{A,ab}$. Correspondingly, we construct a set V of all relevant vertices. A simplified path finder algorithm in pseudo code, can be formulated as follows:

Step 1: Define index $n = 0$.

Step 2: If ($n > 6$) then go to Step 10;
else define $\boldsymbol{\delta z}_a = \boldsymbol{T}_z[n]$ and $\boldsymbol{L}_{\text{pref}} = [\boldsymbol{r}_a, \boldsymbol{r}_a + \boldsymbol{\delta z}_a]$.

Step 3: Let B_n be a sub-set of all boundary segments in B which agent a will come in direct contact with assuming a is moving along $\boldsymbol{L}_{\text{pref}}$. If B_n is empty, go to Step 7.

Step 4: Find boundary segment $b \in B_n$ which represents the most critical obstacle, meaning the segment which requires the largest modification in preferred direction of movement to avoid collision.

Step 5: Evaluate the possibility of the agent moving around one of the two vertices associated with the obstructing boundary segment. If it is possible to move around both vertices, the most favourable vertex v is chosen (based on distance, direction, and possible connection to other boundary segments). If not, go to Step 8.

Step 6: Construct a modified preferred path of movement which, in the absence of other forces, will cause the agent to move around vertex v without coming in direction contact with the boundary. Store this in $\boldsymbol{\delta z}_a$. Let $\tilde{\boldsymbol{z}}_a^b = \boldsymbol{\delta z}_a + \boldsymbol{r}_a$ AND go to Step 9;

Step 7: If ($n > 0$) then $\tilde{\boldsymbol{z}}_a^b = \boldsymbol{\delta z}_a + \boldsymbol{r}_a$ AND go to Step 9;
else go to Step 10.

Step 8: n = n+1. Go to step 2.

Step 9: The current temporary target position candidate is accepted, $\tilde{\boldsymbol{z}}_a = (1 - \omega_a)\boldsymbol{z}_a + \omega_a \tilde{\boldsymbol{z}}_a^b$, where ω_a is a smoothing factor to ensure that the modification to the preferred path gradually increases from zero as the agent approach the segment from infinity. The direction of the preferred velocity, $\boldsymbol{u}_a$, is changed to make $\boldsymbol{u}_a$ parallel to $\tilde{\boldsymbol{z}}_a - \boldsymbol{r}_a$. Go to Step 10.

Step 10: Finish.